

12-14-2015

Development of Highly Active and Stable Hybrid Cathode Catalyst for PEMFCs

Won Suk Jung

University of South Carolina - Columbia

Follow this and additional works at: <http://scholarcommons.sc.edu/etd>



Part of the [Chemical Engineering Commons](#)

Recommended Citation

Jung, W. S.(2015). *Development of Highly Active and Stable Hybrid Cathode Catalyst for PEMFCs*. (Doctoral dissertation). Retrieved from <http://scholarcommons.sc.edu/etd/3261>

This Open Access Dissertation is brought to you for free and open access by Scholar Commons. It has been accepted for inclusion in Theses and Dissertations by an authorized administrator of Scholar Commons. For more information, please contact SCHOLARC@mailbox.sc.edu.

DEVELOPMENT OF HIGHLY ACTIVE AND STABLE HYBRID CATHODE CATALYST
FOR PEMFCs

by

Won Suk Jung

Bachelor of Science
Sungkyunkwan University, 2005

Master of Science
Korea University of Science and Technology, 2008

Submitted in Partial Fulfillment of the Requirements

For the Degree of Doctor of Philosophy in

Chemical Engineering

College of Engineering & Computing

University of South Carolina

2015

Accepted by:

Branko Popov, Major Professor

John W. Weidner, Committee Member

Francis Gadala-Maria, Committee Member

Andreas Heyden, Committee Member

Xinyu Huang, Committee Member

Lacy Ford, Senior Vice Provost and Dean of Graduate Studies

© Copyright by Won Suk Jung, 2015
All Rights Reserved.

DEDICATION

To my beloved family,

아내 연재와 딸 수아 그리고 양가 부모님께 바칩니다.

ACKNOWLEDGEMENTS

I appreciate my advisor, Dr. Popov, guiding me for the direction where I go. Especially, he gave me an opportunity to participate in the huge research program and an intrinsic experience. This is the precious feeling in my life ever and I cannot forget the lessons from that experience. As well, I thank my all the colleagues who helped to prepare this work.

I specially thank all committee members, Dr. Andreas Heyden, Dr. Francis Gadala-Maria, and Dr. Xinyu Huang. They spent their precious time to suggest and advise this work and made it more reasonable.

My parents have had a worry for my future and life all the time. But they have believed and supported me. It is more valuable than millions of dollars to me. Also my wife who flew ten thousands of miles from home to here has sacrificed her-self for me. Since I know this is not easy, she deserves to get my appreciation. My friends, Dr. Hyunseok Cho and Hyeran Cho, helped me a lot to prepare the presentation and dissertation in detail.

ABSTRACT

Polymer electrolyte membrane fuel cells (PEMFCs) are attractive power sources of the future for a variety of applications including portable electronics, stationary power, and automobile application. However, sluggish cathode kinetics, high Pt cost, and durability issues inhibit the commercialization of PEMFCs. To overcome these drawbacks, research has been focused on alloying Pt with transition metals since alloy catalysts show significantly improved catalytic properties like high activity, selectivity, and durability. However, Pt-alloy catalysts synthesized using the conventional impregnation method exhibit uneven particle size and poor particle distribution resulting in poor performance and/or durability in PEMFCs.

In this dissertation, a novel catalyst synthesis methodology is developed and compared with catalysts prepared using impregnation method and commercial catalysts. Two approaches are investigated for the catalyst development. The catalyst durability was studied under U. S. DRIVE Fuel Cell Tech Team suggested protocols. In the first approach, the carbon composite catalyst (CCC) having active sites for oxygen reduction reaction (ORR) is employed as a support for the synthesis of Pt/CCC catalyst. The structural and electrochemical properties of Pt/CCC catalyst are investigated using high-resolution transmission electron microscopy, X-ray diffraction, and X-ray photoelectron spectroscopy, while RDE and fuel cell testing are carried out to study the electrochemical properties. The synergistic effect of CCC and Pt is confirmed by the observed high activity towards ORR for the Pt/CCC catalyst. The second approach is the synthesis of

Co-doped hybrid cathode catalysts (Co-doped Pt/CCC) by diffusing the Co metal present within the CCC support into the Pt nanoparticles during heat-treatment. The optimized Co-doped Pt/CCC catalyst performed better than the commercial catalysts and the catalyst prepared using the impregnation method in PEMFCs and showed high stability under 30,000 potential cycles between 0.6 and 1.0 V. To further increase the stability of the catalyst at high potential cycles (1.0-1.5 V), high temperature treatment is used to obtain graphitized carbon having optimum BET surface area. The novel catalyst synthesis procedure developed in this study was successfully applied for the synthesis of Co-doped Pt catalysts supported on the graphitized carbon which showed high activity and enhanced stability at high potentials.

TABLE OF CONTENTS

DEDICATION	iii
ACKNOWLEDGEMENTS.....	iv
ABSTRACT	v
LIST OF TABLES	ix
LIST OF FIGURES	x
LIST OF SYMBOLS	xvi
LIST OF ABBREVIATIONS.....	xviii
CHAPTER 1: INTRODUCTION.....	1
1.1 BACKGROUND OF PEMFCs.....	1
1.2 LITERATURE REVIEW	3
1.3 OBJECTIVES AND OUTLINE.....	31
CHAPTER 2: SYNERGISTIC EFFECT OF CCC AND Pt CATALYST	34
2.1 INTRODUCTION	34
2.2 EXPERIMENTAL	35
2.3 RESULTS AND DISCUSSION.....	38
2.4 CONCLUSION	60
CHAPTER 3: DEVELOPMENT OF HIGHLY ACTIVE AND STABLE HYBRID CATHODE CATALYST UNDER POTENTIAL CYCLING CONDITIONS FOR PEMFCs	62
3.1 INTRODUCTION	62

3.2 EXPERIMENTAL	65
3.3 RESULTS AND DISCUSSION	70
3.4 CONCLUSION	106
CHAPTER 4: EVALUATION OF CARBON NANOSTRUCTURE OBTAINED AT HIGH TEMPERATURE AND ITS DURABILITY UNDER PEMFC START-UP/SHUTDOWN CYCLING CONDITIONS	108
4.1 INTRODUCTION	108
4.2 EXPERIMENTAL	111
4.3 RESULTS AND DISCUSSION	114
4.4 CONCLUSION	133
CHAPTER 5: ENHANCED DURABILITY OF CO-DOPED Pt/GCCC CATALYST UNDER POTENTIAL CYCLING FOR PEMFCs	134
5.1 INTRODUCTION	134
5.2 EXPERIMENTAL	137
5.3 RESULTS AND DISCUSSION	140
5.4 CONCLUSION	161
CHAPTER 6: SUMMARY	163
REFERENCES	165

LIST OF TABLES

Table 2.1 Characteristics of CCC obtained from XPS N1s peak	45
Table 2.2 Characteristics of the Pt/CB and Pt/CCC catalysts obtained from XPS Pt4f peaks	53
Table 2.3 Characteristics of Pt/CCC obtained from XPS N1s peak	54
Table 2.4 Electrochemical properties of the Pt/CB and Pt/CCC catalysts obtained from CV diagrams and LSV curves.....	58
Table 3.1 Characteristics of CCC obtained from XPS N1s peak	78
Table 3.2 Summary of synthesis conditions, structural characteristics, and composition of Co-doped Pt/CCC	84
Table 3.3 Pt:Co atomic compositions of Pt/CCC and Co-doped Pt/CCC measured by ICP-AES, XPS, and XRF.....	99
Table 3.4 Characteristics of XRD peak for Co-doped Pt/CCC and PtCo/C-Imp after 30,000 cycles.....	102
Table 3.5 Comparison of mass activities, OCPs in H ₂ /air, and maximum power density for Co-doped Pt/CCC, PtCo/C-Imp, PtCo/C, and Pt/C catalysts.....	104
Table 5.1 Characteristics of Co-doped Pt/CCC, Pt/GCCC and Co-doped Pt/GCCC.....	151
Table 5.2 Compositions of Pt/CCC, Co-doped Pt/CCC, Pt/GCCC and Co-doped Pt/GCCC measured by ICP-AES, XPS, and XRF	156
Table 5.3 Characteristics of XRD peak for Co-doped Pt/CCC and Co-doped Pt/GCCC after AST	159

LIST OF FIGURES

Figure 1.1 A schematic of typical PEMFC	4
Figure 1.2 Modeled cost of an 80-kW _{net} PEM fuel cell system based on projection to high-volume manufacturing (500,000 units per year) in 2013	5
Figure 1.3 Time dependence of the electrode weight measured in 1 M HClO ₄ and at 80 °C at different dissolution potentials: (a) 0.85, (b) 0.95, (c) 1.05, (d) 1.15, and (e) 1.4; (f) time dependence of the steady-state current at a potential of 1.4 V	8
Figure 1.4 (a) Equilibrium soluble platinum concentration as a function of temperature and voltage. Solid line, 196 °C, platinum foil from Bindra et al.; dashed line, 25 °C, platinum foil from Pourbaix; short-dashed line, 80 °C, platinum foil interpolated; solid circles, 80 °C, 2-3 nm platinum particles of a 46 wt% Pt/C electrocatalyst powder Tanaka sample measured in 0.5 M H ₂ SO ₄ . (b) Pt dissolution rate vs dissolution potential and temperature. The real surface area of the electrode is 24 cm ²	9
Figure 1.5 Alternation of the platinum surface state during: (a) anodic polarization, above ca. 1.1 V (vs. RHE) dissolution and passivation of the surface are in competition; and (b) cathodic polarization, during surface reduction below ca. 1.0 V (vs. RHE) (re-)deposition and dissolution are in competition	11
Figure 1.6 Performance loss of MEAs measured after being subjected to Pt dissolution ASTs at 40, 60 and 80 °C. Performance loss obtained from polarization curves at (a) 0.1 A cm ⁻² and (b) 1.7 A cm ⁻² . Variation of % ECSA loss with number of cycles during the AST is shown in (c)	12
Figure 1.7 Cobalt dissolution as a function of cycling number of PtCo/C electrode in a liquid cell of 0.1M HClO ₄ . The cycling test was conducted at 25 °C	13
Figure 1.8 The amount of ions dissolved from the Pt–M alloys in 0.5M H ₂ SO ₄ solution at 25 °C (a) dissolved M ions during 3 h-immersion test, (b) dissolved Pt ions after 3 h-immersion test. (c) dissolved M ions under the potentiostatic polarization at 1.0, 1.2 and 1.4 V. (d) dissolved M ions measured at the end of 100 cycles of CVs	16
Figure 1.9 Effect of upper potential limit of CV on amounts of (a) M (= Co, Ni, Fe) and (b) Pt dissolved from the Pt–M alloys by 100 potential cycles. The lower potential limit was fixed at 0 V. Effect of lower potential limit of CV on amounts of (a) M (= Co, Ni, Fe) and (b) Pt dissolved from the Pt–M alloys by 100 potential cycles. The upper potential limit was fixed at 1.4 V	17

Figure 1.10 Potential distributions along anode flow path during reverse current conditions	20
Figure 1.11 CVs of 10 wt% TFE-Vulcan composite after potential holds at 65 °C for 16 h at (a) 0.8, (b) 1.0, and (c) 1.2 V (sweep rate of 10 mV s ⁻¹). The initial (0 h) CVs of the prefilled samples overlapped	23
Figure 1.12 AFM images (1 μm × 1 μm) of a Pt-catalyzed HOPG surface (a) before and (b) after potential retention at 1.0 V for 70 h in a 1.0 M HClO ₄ solution.....	24
Figure 1.13 LSV curves of CCC treated by a pyrolysis alone and by a series of pyrolysis, leaching and 2nd pyrolysis. The measurements were performed in O ₂ -saturated 0.5 M H ₂ SO ₄ solution using a potential scan rate of 5 mV sec ⁻¹ and an electrode rotation rate of 900 rpm	28
Figure 1.14 Polarization curves of PEMFCs prepared with CCC as a cathode treated by a pyrolysis alone and by a series of pyrolysis, leaching and 2nd pyrolysis. The CCC loading is 6 mg cm ⁻² . The test was run with H ₂ /O ₂ back pressure of 30 psi/30 psi. The fuel cell operating temperature is 75 °C.....	29
Figure 1.15 Long-term fuel cell stability test measured on the carbon composite catalysts at 200 mA cm ⁻²	30
Figure 2.1 (a) N ₂ adsorption/desorption isotherms and (b) BJH pore-size distribution curves obtained from the adsorption branch of CB and CCC. The inset in (b) compares the PSD in the range 0-10 nm	39
Figure 2.2 Comparison of XRD patterns of CCC and CB.....	41
Figure 2.3 HR-TEM images of (a) CCC and (b) CB	42
Figure 2.4 (a) XPS survey scans of CCC and CB and (b) deconvoluted N1s XPS spectra of CCC	43
Figure 2.5 (a) CV diagrams of CCC and CB in N ₂ -saturated 0.1 M HClO ₄ at room temperature and scan rate of 50 mV s ⁻¹ . (b) LSV curves of Pt/C, CCC and CB in O ₂ -saturated 0.1 M HClO ₄ at room temperature and scan rate of 5 mV s ⁻¹ with 1600 rpm. (c) The Koutechy-Levich plots from LSV data of CCC at different potentials. (d) Tafel plot from LSV data of CCC at 1600 rpm.....	46
Figure 2.6 Comparison of XRD patterns of Pt/CCC and Pt/CB catalysts	49
Figure 2.7 HR-TEM images of (a) Pt/CCC and (b) Pt/CB catalysts	50
Figure 2.8 Deconvoluted XPS spectra of Pt4f in (a) Pt/CCC and (b) CB. (c) Deconvoluted XPS spectra of N1s Pt/CCC	51

Figure 2.9 (a) CV diagrams of Pt/CCC and Pt/CB in N ₂ -saturated 0.1 M HClO ₄ at room temperature and scan rate of 50 mV s ⁻¹ . (b) LSV curves of Pt/CCC and Pt/CB in O ₂ -saturated 0.1 M HClO ₄ at room temperature and scan rate of 5 mV s ⁻¹ at 1600 rpm. (c) Tafel plots from LSV data of Pt/CCC and Pt/CB at 1600 rpm.....	56
Figure 2.10 (a) PEMFC polarization curves of Pt/CCC and Pt/CB with various Pt loading at 80 °C and 100% RH and without backpressure. (b) PEMFC polarization curves of Pt/CCC and Pt/CB with various backpressures at 0.04 mg cm ⁻² Pt loading at 80 °C and 100% RH. (c) Mass activities of Pt/CCC and Pt/CB at 80 °C and 100% RH applying a backpressure of 7.3 psi.....	59
Figure 3.1 Schematic diagram for CCC support and Co-doped Pt/CCC catalyst synthesis	71
Figure 3.2 (a) N ₂ adsorption/desorption isotherms and (b) BJH pore-size distribution curves obtained from the adsorption branch of CCC and CB. The inset in (b) compares the PSD in the range 0-10 nm	72
Figure 3.3 Comparison of (a) XRD patterns and (b) Raman spectra of CCC and CB	74
Figure 3.4 HR-TEM images of (a) CCC and (b) CB	76
Figure 3.5 (a) XPS survey scans of CCC and CB and (b) deconvoluted N1s XPS spectra of CCC	77
Figure 3.6 (a) CV diagrams of CCC and CB in N ₂ -saturated 0.1 M HClO ₄ at room temperature and scan rate of 50 mV s ⁻¹ . (b) LSV curves of CCC and CB in O ₂ -saturated 0.1 M HClO ₄ at room temperature and scan rate of 5 mV s ⁻¹ at 1600 rpm	80
Figure 3.7 (a) XRD patterns of CCC, Pt/CCC, and Co-doped Pt/CCC prepared at 700, 750, 800, and 900 °C. Deconvoluted peaks of (b) Co-doped Pt/CCC-700, (c) Co-doped Pt/CCC-750, (d) Co-doped Pt/CCC-800 and (e) Co-doped Pt/CCC-900.....	82
Figure 3.8 (a) XRD patterns of Pt/C, PtCo/C-Imp-800, and PtCo/C-Imp-900 prepared at 800, and 900 °C. Deconvoluted XRD patterns of (b) PtCo/C-Imp-800, and (c) PtCo/C-Imp-900.....	85
Figure 3.9 HR-TEM images of (a) Pt/CCC , (b) Co-doped Pt/CCC-700, (c) Co-doped Pt/CCC-750, (d) Co-doped Pt/CCC-800 and (e)Co-doped Pt/CCC-900.....	86
Figure 3.10 H ₂ /air polarization curves of (a) Co-doped Pt/CCC-700, (b) Co-doped Pt/CCC-750, and (c) Co-doped Pt/CCC-800 (initial and after 10,000 and 30,000 cycles)	88
Figure 3.11 H ₂ /air polarization curves of Co-doped Pt/CCC, PtCo/C-Imp, PtCo/C, and Pt/C before and after 30,000 potential cycles between 0.6 and 1.0 V	90

Figure 3.12 Comparison of mass activities of (a) Co-doped Pt/CCC, (b) PtCo/C-Imp, (c) PtCo/C, and (d) Pt/C catalysts as a function of cycle number. The activities were measured under the following operating conditions: H ₂ /O ₂ (2/9.5 stoic.), 80 °C, 100% RH, and 150 kPa _{abs.} back pressure.....	91
Figure 3.13 Mass activity degradation of Co-doped Pt/CCC, PtCo/C-Imp, PtCo/C, and Pt/C catalysts as a function of cycle number	93
Figure 3.14 X-ray energy dispersive spectrometry (XEDS) particle line-scan of Co-doped Pt/CCC catalyst (after 30,000 cycles).....	94
Figure 3.15 Normalized ECSA of Co-doped Pt/CCC, PtCo/C –Imp, PtCo/C, and commercial Pt/C catalysts as a function of cycle number. ECSAs were calculated from cyclic voltammograms obtained between 0.05 and 0.6 V (vs. RHE) at 80 °C. Fully humidified H ₂ (200 sccm) and N ₂ (75 sccm) were supplied to the anode and the cathode, respectively	96
Figure 3.16 HR-TEM images and particle size distribution for (a) Co-doped Pt/CCC and (b) Pt/C catalysts before and after 30,000 cycles.....	97
Figure 3.17 Comparison of XRD patterns of (a) Co-doped Pt/CCC and (c) PtCo/C-Imp before and after 30,000 cycles. Deconvoluted peaks of (b) Co-doped Pt/CCC and (d) PtCo/C-Imp after 30,000 cycles.....	101
Figure 3.18 Cyclic voltammograms of Pt/CCC and Co-doped Pt/CCC. The measurements were carried out at room temperature by sweeping the potential from 0.05-1.0 V vs. RHE at 50 mV s ⁻¹ in nitrogen-purged 0.1 M HClO ₄	105
Figure 4.1 (a) N ₂ adsorption/desorption isotherms and (b) BJH pore-size distribution curves obtained from the adsorption branch of KB heat-treated at different temperatures. The inset in (b) compares the PSD in the range 0-10 nm	115
Figure 4.2 Comparison of XRD patterns of KB heat-treated at different temperature...	117
Figure 4.3 Raman spectra of (a) KB, (b) KB-9, (c) KB-13, and (d) KB-17	118
Figure 4.4 (a) Change of specific surface area and I _D /I _G as a function of temperature. (b) Change of interlayer spacing as a function of temperature. (c) Relationship between I _D /I _G and interlayer spacing	120
Figure 4.5 HR-TEM images of (a, b) KB and (c, d) KB-17	121
Figure 4.6 (a) N ₂ adsorption/desorption isotherms and (b) BJH pore-size distribution curves obtained from the adsorption branch of Pt/KB and Pt/KB-17. The inset in (b) compares the PSD in the range 0-10 nm.....	122
Figure 4.7 Comparison of XRD patterns of Pt/KB and Pt/KB-17 catalysts.....	124

Figure 4.8 HR-TEM images of (a) Pt/KB and (b) Pt/KB-17 catalysts	125
Figure 4.9 (a) LSV curves of Pt/KB and Pt/KB-17 catalysts in O ₂ -saturated 0.1 M HClO ₄ at room temperature and scan rate of 5 mV s ⁻¹ with 1600 rpm. The inset in (a) shows specific activities calculated from ECSA and platinum loading. (b) Tafel plots from LSV data of Pt/KB and Pt/KB-17 catalysts at 1600 rpm	127
Figure 4.10 (a) H ₂ /air polarization and (b) the power density curves of Pt/KB and Pt/KB-17 catalysts before and after 3,000 potential cycles between 1.0 and 1.5 V	129
Figure 4.11 Normalized ECSA of Pt/KB and Pt/KB-17 as a function of cycle number. ECSAs were calculated from cyclic voltammograms obtained between 0.05 and 0.6 V (vs. RHE) at 80 °C. Fully humidified H ₂ (200 sccm) and N ₂ (75 sccm) were supplied to the anode and the cathode, respectively.....	131
Figure 5.1 (a) N ₂ adsorption/desorption isotherms and (b) BJH pore-size distribution curves obtained from the adsorption branch of GCCC, CCC and CB. (c) BJH pore-size distribution in the range 0-10 nm.....	141
Figure 5.2 (a) XPS survey scans of GCCC, CCC and CB. Deconvoluted N1s XPS spectra of (b) CCC and (c) GCCC	143
Figure 5.3 (a) Comparison of (a) XRD patterns of GCCC, CCC and CB. Raman spectra of (b) CCC and (c) GCCC	145
Figure 5.4 HR-TEM images of (a) CB, (b) CCC and (c) GCCC.....	147
Figure 5.5 XRD patterns of GCCC, Pt/GCCC, and Co-doped Pt/GCCC.....	148
Figure 5.6 HR-TEM images of fresh (a) Pt/CCC, (b) Pt/GCCC, (c) Co-doped Pt/CCC, and (d) Co-doped Pt/GCCC catalysts	150
Figure 5.7 (a) H ₂ /air polarization and (b) power density curves of Co-doped Pt/CCC and Co-doped Pt/GCCC before and after potential cycling (1,000 cycles for Co-doped Pt/CCC; 3,000 cycles for Co-doped Pt/GCCC) between 1.0 and 1.5 V, respectively....	153
Figure 5.8 Normalized ECSA of Co-doped Pt/CCC and Co-doped Pt/GCCC catalysts as a function of cycle number. ECSAs were calculated from cyclic voltammograms obtained between 0.05 and 0.6 V (vs. RHE) at 80 °C. Fully humidified H ₂ (200 sccm) and N ₂ (75 sccm) were supplied to the anode and the cathode, respectively.....	155
Figure 5.9 (a) Comparison of XRD patterns of Co-doped Pt/CCC before and after 1,000 cycles. Deconvoluted patterns of Co-doped Pt/CCC (b) before and (c) after 1,000 cycles	157
Figure 5.10 (a) Comparison of XRD patterns of Co-doped Pt/GCCC before and after 3,000 cycles. Deconvoluted patterns of Co-doped Pt/GCCC (b) before and (c) after 3,000 cycles.....	158

LIST OF SYMBOLS

E	Electrode potential.
e	electrons.
E_{upper}	upper potential limit.
E_{lower}	lower potential limit.
E_{rest}	rest potential.
ad	adsorbed molecule.
CO_{surf}	CO molecule on surface of catalyst.
C=O	carbonyl group.
C-O-C	ethers.
O-C=O	carboxyl group.
D	crystallite size.
k	dimensionless shape coefficient.
θ	angle at the position of the maximum peak known as Bragg angle.
π	pi.
i	measured current density.
i_k	kinetic current density.
i_{dl}	diffusion-limited current density.
B	Levich slope.
n	the number of electrons exchanged in oxygen reduction reaction.
F	Faraday constant.

- C_{O_2} bulk concentration of oxygen.
- D_{O_2} diffusion coefficient of oxygen in the bulk solution.
- ω rotation rate in rpm.
- ν kinematic viscosity of the solution.
- Q_H coulombic charge for hydrogen desorption.
- L_{Pt} Pt loading.
- $V_{iR-free}$ iR-corrected potential.
- i^0 exchange current density.
- A_s specific activity.
- (s) surface site.

LIST OF ABBREVIATIONS

AFM	Atomic Force Microscopy
AST	Accelerated Stress Test
BCC	Body-Centered Cubic
BE	Binding Energy
BET	Brunauer-Emmett-Teller
BJH	Barrett-Joyner-Halenda
CB	Carbon Black
CCC	Carbon Composite Catalyst
CFDE	Channel Flow Double Electrode
CNC	Carbon Nanocage
CNF	Carbon Nanofiber
CNT	Carbon Nano-Tube
CV	Cyclic Voltammetry
DEMS	Differential Electrochemical Mass Spectroscopy
DMFC	Direct Methanol Fuel Cell
ECSA	Electrochemical Surface Area
EIS	Electrochemical Impedance Spectroscopy
EPMA	Electron Probe Microanalysis
EQCM	Electrochemical Quartz Crystal Microbalance
FCC	Face-Centered Cubic
FCT	Face-Centered Tetragonal

FE-SEM	Field Emission-Scanning Electron Microscopy
GCCC.....	Graphitized Carbon Composite Catalyst
GCNT.....	Graphitic Carbon Nanotube
GO.....	Graphene Oxide
HCC	Hybrid Cathode Catalyst
HOPG.....	Highly Oriented Pyrolytic Graphite
HR-TEM	High Resolution Transmission Electron Microscope
ICP-AES	Inductively Coupled Plasma Atomic Emission Spectroscopy
ICP-MS	Inductively Coupled Plasma-Mass Spectrometry
IPA	Isopropyl Alcohol
IUPAC.....	The International Union of Pure and Applied Chemistry
LSV	Linear Sweep Voltammetry
MCFC	Molten Carbonate Fuel Cell
MEA.....	Membrane-Electrode Assembly
MIMS	Membrane Inlet Mass Spectrometry
ML.....	Monolayer
MWNT	Multi-Walled Carbon Nanotube
OCP.....	Open Circuit Potentials
ORR	Oxygen Reduction Reaction
PAFC.....	Phosphoric Acid Fuel Cell
PCA.....	1-Pyrenecarboxylic Acid
PDDA.....	Poly(Diallyldimethylammonium Chloride)
PEMFC	Polymer Electrolyte Membrane Fuel Cell
PSD	Pore Size Distribution
RDE.....	Rotating Disk Electrode

RH.....	Relative Humidity
RHE.....	Reversible Hydrogen Electrode
SD	Standard Deviation
SOFC.....	Solid Oxide Fuel Cell
SXPES.....	Soft X-Ray Photoemission Spectroscopy
XAS.....	X-ray Absorption Spectroscopy
XEDS	X-ray Energy Dispersive Spectrometry
XPS	X-ray Photoelectron Spectroscopy
XRD	X-Ray Diffraction
XRF.....	X-Ray Fluorescence

CHAPTER 1

INTRODUCTION

1.1 BACKGROUND OF PEMFCS

Fuel cells are the electrochemical converters that transform the chemical energy into electrical energy. Briefly, fuel cells produce electricity by two simple reactions where hydrogen is oxidized at the anode and oxygen is reduced at the cathode and water is produced as a by-product. Unlike internal combustion engines, the fuels (hydrogen and oxygen) are not burned in fuel cells. Instead, the electrical energy is generated by electro-catalytical behavior. Due to the benefit, the energy efficiency is drastically high as compared to the internal combustion engines. Moreover, the heat produced by fuel cells operation can be harnessed for heating, hot water, and/or refrigeration cycles.

Fuel cells are similar with batteries since they use an electro-chemical reaction to provide electricity. However, a battery stores the chemical reactants such as metal compounds as a source of energy. Once it is used up, they must be discarded in case of primary batteries or externally recharged in case of rechargeable batteries. On the other hand, fuel cells can run indefinitely as long as the reactants, namely hydrogen and oxygen (or air), are supplied to the fuel cells.

There are several different types of fuel cells namely, proton exchange membrane fuel cells (PEMFCs), direct methanol fuel cells (DMFCs), phosphoric acid fuel cells (PAFCs), molten carbonate fuel cells (MCFCs) and solid oxide fuel cells (SOFCs). Fuel

cells classification is determined by different types of electrolyte employed in the respective system. PEMFCs in general have the following benefits over the traditional power sources (e.g. internal combustion engines and batteries).

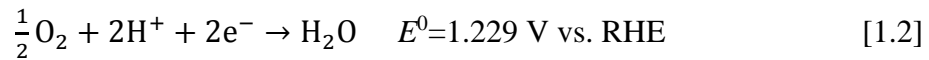
1. Higher efficiency than internal combustion engines.
2. Ability to run with low noise.
3. Produce only water as the by-product thus preventing pollution caused by fossil fuels in internal combustion engines.
4. Provide greater energy security for the country that does not have oil or natural gas.
5. Produce stable electricity independently when used as a stationary power.
6. High temperature fuel cells produce electricity and heat simultaneously. The heat is well suited for cogeneration application.
7. Operating times are even longer than batteries.
8. No “memory effect” unlike batteries.

A PEMFC unit consists of a stack. A stack is comprised of numerous individual membrane-electrode assemblies (MEAs). An MEA has a solid electrolyte and two electrodes. Of the two electrodes, one is positive (cathode) and the other is negative (anode). An electrolyte plays a key role; it must permit only the appropriate ions to transfer between the electrodes. The failure of an electrolyte leads to disturbance in the reactions on the electrodes. The hydrogen oxidation reaction takes place on the anode, while the oxygen reduction reaction (ORR) occurs on the cathode.

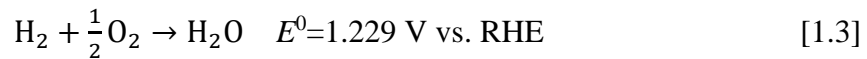
The reactions in fuel cells are explained as follows. Hydrogen is supplied to the anode which is electro-catalytically decomposed into protons and electrons according to the following reaction:



The protons produced at the anode permeate through the electrolyte membrane to the cathode. On the other hand, the electrons move along an external circuit to the cathode. The oxygen supplied to the cathode reacts with the protons and electrons from the anode to produce water according to the following reaction:



The overall reaction in a fuel cell is as follows.



1.2 LITERATURE REVIEW

Challenges the PEMFCs have faced are largely the cost, and durability. In the past several years, the effort for the fuel cell cost-down has been successful. For example, the cost for fuel cell has been reduced from \$275 kW⁻¹ in 2002 to \$51 kW⁻¹ in 2010 [1]. However, it is still more expensive than the internal combustion engine systems [2]. One primary portion of a fuel cell cost is due to the membrane electrode assembly (MEA) wherein the fuel cell reactions, fuel oxidation and oxygen reduction, take place. The most preferred catalysts used in the MEAs are based on Pt which is expensive and scarce. The Pt loading has been reduced by two orders of magnitude in the past decade and there is still room for further reduction by developing highly-active catalysts. The 2020 DOE targets for the fuel cell cost is \$40 kW⁻¹ for the transportation application. Specifically,

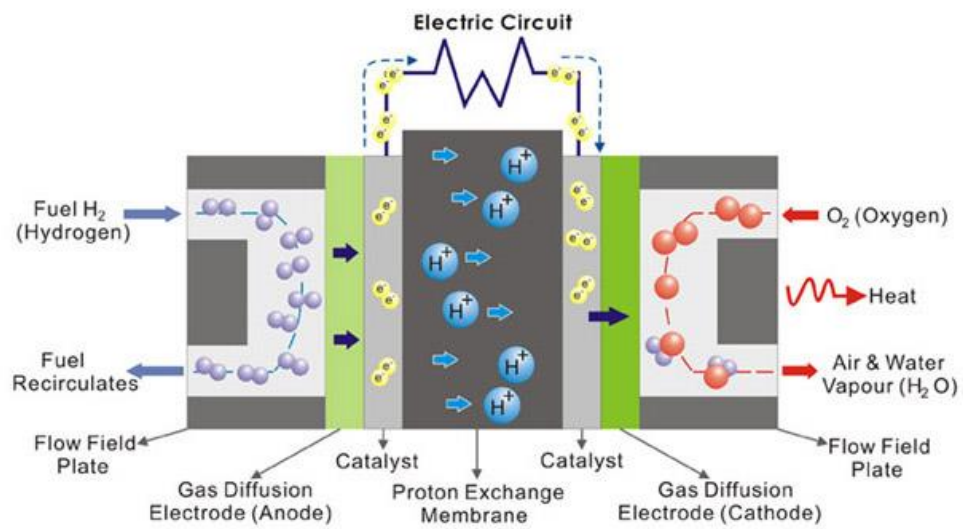


Figure 1.1 A schematic of typical PEMFC [3].



Figure 1.2 Modeled cost of an 80-kW_{net} PEM fuel cell system based on projection to high-volume manufacturing (500,000 units per year) in 2013 [4].

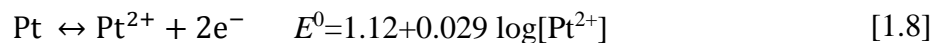
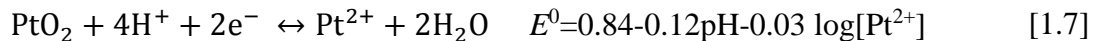
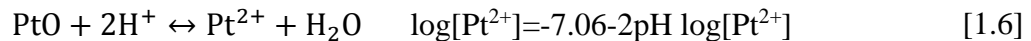
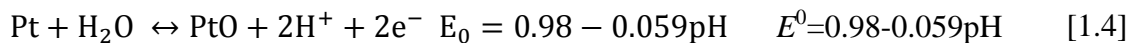
for the catalyst, a total loading (anode + cathode) of 0.125 mg_{Pt} cm⁻² is targeted by the US Department of Energy by FY 2017.

Fuel cell components like the MEA suffer degradation during long-term operations. The lifetime required by a commercial fuel cell is over 5,000 h durability for light-weight vehicles [2]. The degradation on long-term operation is caused by platinum sintering and dissolution, especially under load cycling and high electrode potentials. Carbon-support corrosion is another challenge at high electrode potentials and can worsen with load cycling.

Therefore, ways to cut costs by reducing cathode loadings to 0.1 mg_{Pt} cm⁻² by employing catalysts having high performance and durability is the core-issue of most of the electro-catalyst research.

1.2.1 PT-BASED CATALYST DEGRADATION

Platinum is well-known as a stable material in most of the acidic solutions such as sulfuric acid and hydrochloric acid. However, under certain conditions, it can undergo dissolution. Especially, Pt can be oxidized and reduced as follows [5].



Researchers found that the platinum is not stable under the PEMFC operation conditions such as high operating temperature, high humidity, and high potential. Dam

et.al [6] determined the in-situ dissolution of platinum using the conventional electrochemical cell equipped with a quartz crystal microbalance. According to the results, they observed that the gain in the electrode mass is due to the oxide formation and the loss of mass is attributed to the dissolution. The gain in the mass occurred for the first certain time while a constant potential is applied to the electrode. After that time, the mass decreased. For example, at a constant potential of 0.85 V, the mass increased for the first 100 min. After 100 min, the mass of the electrode decreased. They also noted that the dissolution rate was strongly dependent on the temperature. Platinum dissolution rate at 80 °C was even faster than that at 60 °C. At 0.95 V, it showed 100 ng h⁻¹cm⁻² at 80 °C, while it was 0.05 ng h⁻¹cm⁻² at 60 °C. Some research group verified the dissolution of different type of Pt such as carbon-supported Pt particle, Pt sheet, Pt wire, and Pt disk [7-10]. As shown in Figure 1.3, Wang et.al [10] measured the dissolution rate of Pt by high-resolution inductively coupled plasma-mass spectrometry (ICP-MS) under potentiostatic conditions. They reported that the concentration of dissolved Pt increases from 0.65 to 1.1 V and decreases at higher potentials than 1.1 V, which has been attributed to the formation of a protective oxide film. In particular, results showed that cycling potential ranges between the Pt-oxide formation and reduction enhanced the dissolution rates of Pt [7-9]. Sugawara et.al [11] investigated Pt dissolution under both potentiostatic and potential cycling conditions with a channel flow double electrode (CFDE) combined with Electron Probe Microanalyzer (EPMA) and ICP-MS. According to their results, under potentiostatic conditions, the Pt ions are detected at a potential higher than 0.8 V by ICP-MS, and the dissolution was maximized at 1.1 V. At the potential higher than 1.2 V, the dissolution of Pt is decreased by the Pt oxide formation of 1-2.5 monolayers (ML).

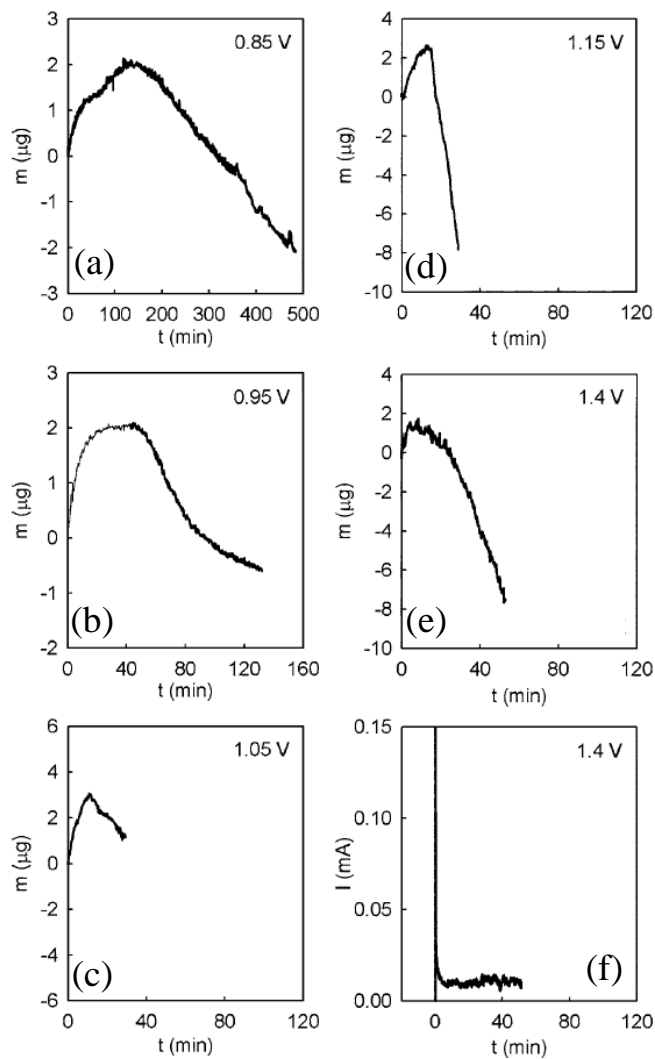


Figure 1.3 Time dependence of the electrode weight measured in 1 M HClO₄ and at 80 °C at different dissolution potentials: (a) 0.85, (b) 0.95, (c) 1.05, (d) 1.15, and (e) 1.4; (f) time dependence of the steady-state current at a potential of 1.4 V [10]

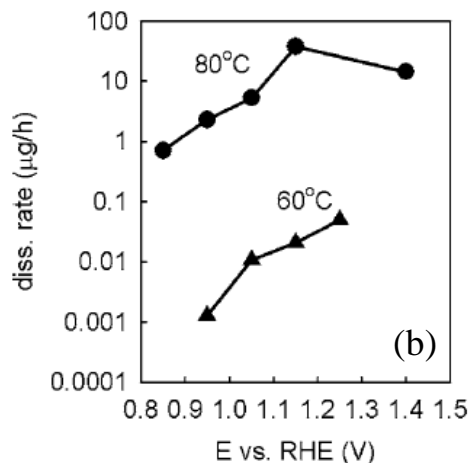
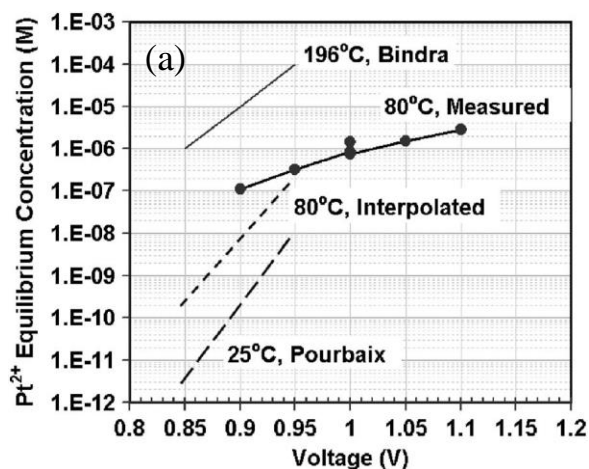


Figure 1.4 (a) Equilibrium soluble platinum concentration as a function of temperature and voltage. Solid line, 196 °C, platinum foil from Bindra et al.; dashed line, 25 °C, platinum foil from Pourbaix; short-dashed line, 80 °C, platinum foil interpolated; solid circles, 80 °C, 2-3 nm platinum particles of a 46 wt% Pt/C electrocatalyst powder Tanaka sample measured in 0.5 M H_2SO_4 [12]. (b) Pt dissolution rate vs dissolution potential and temperature. The real surface area of the electrode is 24 cm^2 [10].

However, under potential cycling conditions, Pt dissolution is enhanced when the upper potential limit is higher than 0.8 V and the lower potential limit is less than 0.6 V, where the Pt-O is completely reduced. Consequently, the Pt dissolution is more accelerated as the upper potential limit shifts more positively. A recent research using ICP-MS online analysis in Figure 1.5 represents a straightforward separation of the anodic and cathodic dissolution processes in correlation with the formation and reduction of the oxide layer [13]. The anodic dissolution is marginally dependent on the potential limits in cyclic voltammetry (CV), the scan rate, and the pH of the electrolyte, while clearly an enhanced cathodic dissolution was observed with higher anodic potential limits, lower scan rates, and increased acidity. As shown in Figure 1.6, Dhanushkodi et.al measured the MEA performance loss under the Pt dissolution conditions such as square-wave cycle (3 s at 0.6 V followed by 3 s at 1.0 V) at 40, 60, and 80 °C [14]. Polarization curves showed performance degradation particularly at low current density where kinetic effects are dominant. The polarization resistances measured in the low current density region by electrochemical impedance spectroscopy (EIS) increased at all temperatures. Electrochemical active surface area (ECSA) showed significant losses at all temperatures. Besides, the temperature leads to higher losses in both ECSA and MEA performance.

In the case of Pt-M alloy (M=Ni, Co, Fe, Cr etc.) catalysts, many literatures reported the dissolution of both Pt and M under operating conditions [15-18]. Yu et al. [18] prepared and evaluated a carbon supported Pt_{2.5}Co₁ catalyst in a dynamic fuel cell with continuous water fluxing on the cathode. Figure 1.7 presents the Co²⁺ concentration as a function of cycling number. It represents that 13.9 molar % cobalt dissolved in the first 400 cycles. The amount of cobalt dissolution was reduced subsequently and leveled

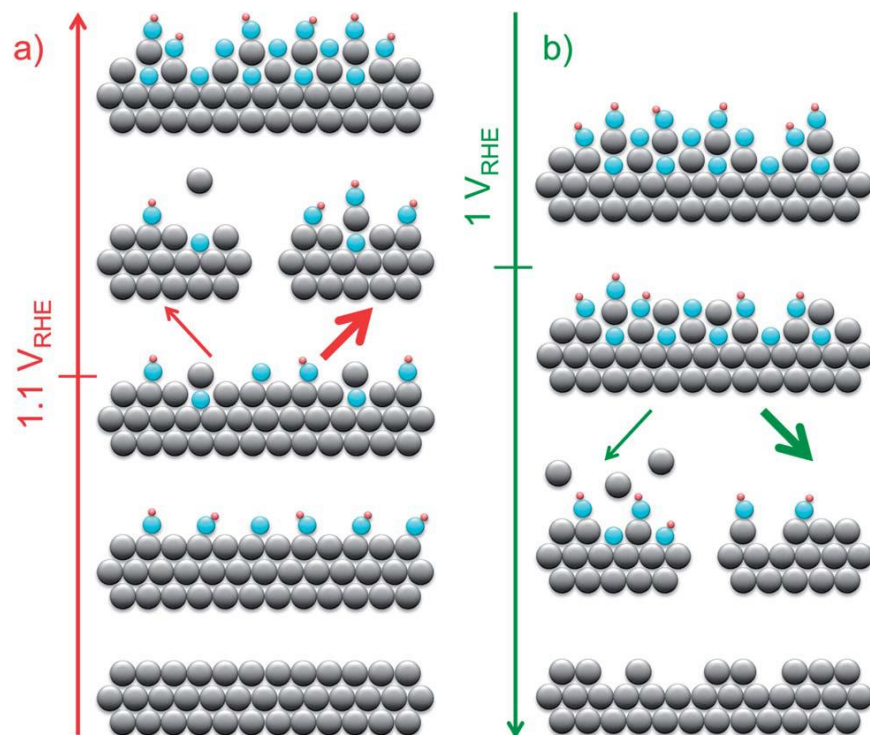


Figure 1.5 Alternation of the platinum surface state during: (a) anodic polarization, above ca. 1.1 V (vs. RHE) dissolution and passivation of the surface are in competition; and (b) cathodic polarization, during surface reduction below ca. 1.0 V (vs. RHE) (re-)deposition and dissolution are in competition [13].

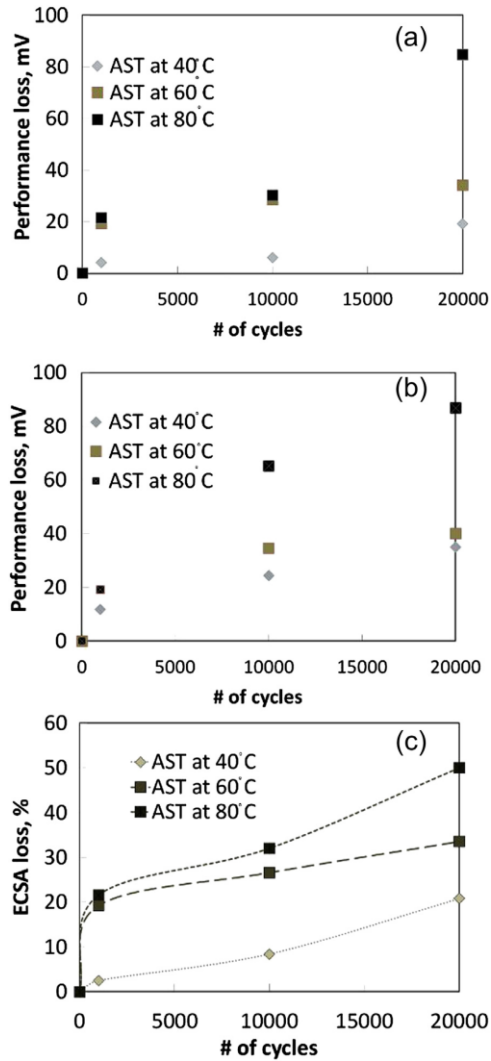


Figure 1.6 Performance loss of MEAs measured after being subjected to Pt dissolution testing protocol at 40, 60 and 80 °C. Performance loss obtained from polarization curves at (a) 0.1 A cm⁻² and (b) 1.7 A cm⁻². Variation of % ECSA loss with number of cycles during the degradation is shown in (c) [14].

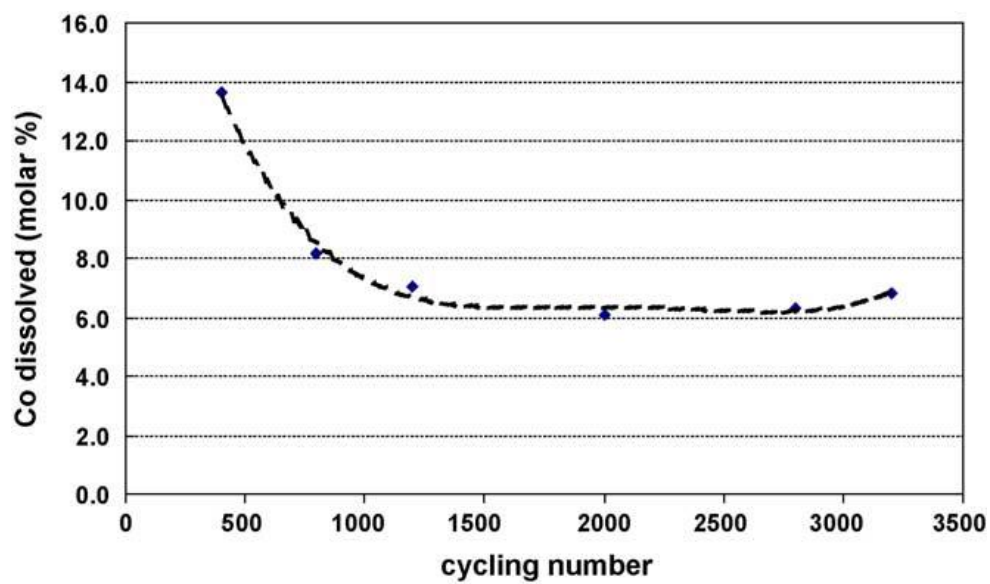


Figure 1.7 Cobalt dissolution as a function of cycling number of PtCo/C electrode in a liquid cell of 0.1M HClO₄. The cycling test was conducted at 25 °C [18].

off to approximately 6% after 800 cycles. This result agreed with a high performance loss in the first 400 cycles and a reduced loss in subsequent cycles. The results indicated that cobalt dissolution neither detrimentally reduced the cell voltage nor dramatically affected the membrane conductance. The overall performance loss over 2400 cycles for the PtCo/C MEAs was less than that of the Pt/C MEA. The performance losses of the Pt/C MEA over 1200 cycles mainly resulted from the cathode ECSA loss due to platinum recrystallization, while the performance losses of the PtCo/C MEA resulted from the activity loss due to cobalt dissolution as well as the ECSA loss.

Bonakdarpour et al. [19] studied the dissolution of Fe and Ni from $Pt_{1-x}M_x$ ($M = Fe, Ni; 0 < x < 1$) catalyst under simulated operating conditions of PEMFCs. Electron microprobe measurements showed that transition metals are removed from all compositions during acid treatment, but that the dissolved amount of metal increases with x , acid strength, and temperature. For $x < 0.6$, the dissolved transition metals originated from the surface, since no significant changes in the lattice size are observed upon dissolution of Fe or Ni. However, for $x > 0.6$, the transition metals dissolved also from the bulk because the lattice constant expands.

Protsailo and Haug [20] investigated the performance and durability improvement of PEMFCs, that can be achieved using PtCo/C and PtIrCo/C, synthesized by the carbothermal technique. The alloys showed not only better activity compared to pure Pt, but they also exhibited remarkable durability in the conditions at which Pt alone is prone to dissolution. The losses of the real surface area of Pt/C, PtCo/C and PtIrCo/C following 1800 cycles at 120 °C were about 45% for Pt/C, 18% for PtCo/C and 8% for PtIrCo/C, respectively.

Johnson Matthey [21, 22] reported a series of carbon supported binary alloys such as PtFe, PtMn, PtNi, PtCr, and PtTi alloys with a Pt to M atomic ratio of 50:50 and heat-treated to a variety of temperatures. Electron probe microanalysis (EPMA) was employed to evaluate the stability of the alloys during operation in the PEMFCs. The PtCr and PtTi alloys did not show any apparent leaching from the catalyst to the membrane or anode catalyst layer, while the PtFe, PtMn, and PtNi showed leaching of the base metal into the MEA, but no performance loss was observed over the 200 h testing.

Hoshi et.al [16] investigated the dissolution behavior of equimolar Pt–M (M: Cu, Co, Ni, Fe) alloys under conditions of immersion, potentiostatic polarization, and potential cycling in 0.5 M H₂SO₄ solution at 25 °C as shown in Figure 1.8. ICP-MS was employed to determine the quantity of dissolved ions. In 3-h immersion tests, selective dissolution of M atoms occurred immediately after immersion and is quickly suppressed. The Pt–Fe alloy exhibited a larger dissolution rate than other alloys. The dissolution rates of Cu, Co, and Ni were negligibly small just after immersion. The Pt-rich layer that formed on the Pt–Co and Pt–Ni surfaces after 1 h of immersion was stable under potentiostatic polarization at 1.0 and 1.2 V, but further dissolution of Co and Ni occurs at 1.4 V. The enhancement of dissolution was more significant under 0–1.4 V potential cycling. The other research in Figure 1.9 represented the dissolution of equimolar Pt–M (M: Co, Ni, Fe) alloys under potential cycling with various combinations of upper potential limit (E_{upper}) and lower potential limit (E_{lower}) in 0.5 M H₂SO₄ solution at 25 °C [17]. Selective dissolution of M was negligibly small when $E_{\text{upper}} \leq E_{\text{rest}}$, while it is increased with positively shifting the E_{upper} when $E_{\text{upper}} > E_{\text{rest}}$. The E_{upper} dependency of Pt dissolution is very similar to that of M dissolution, although the absolute values are

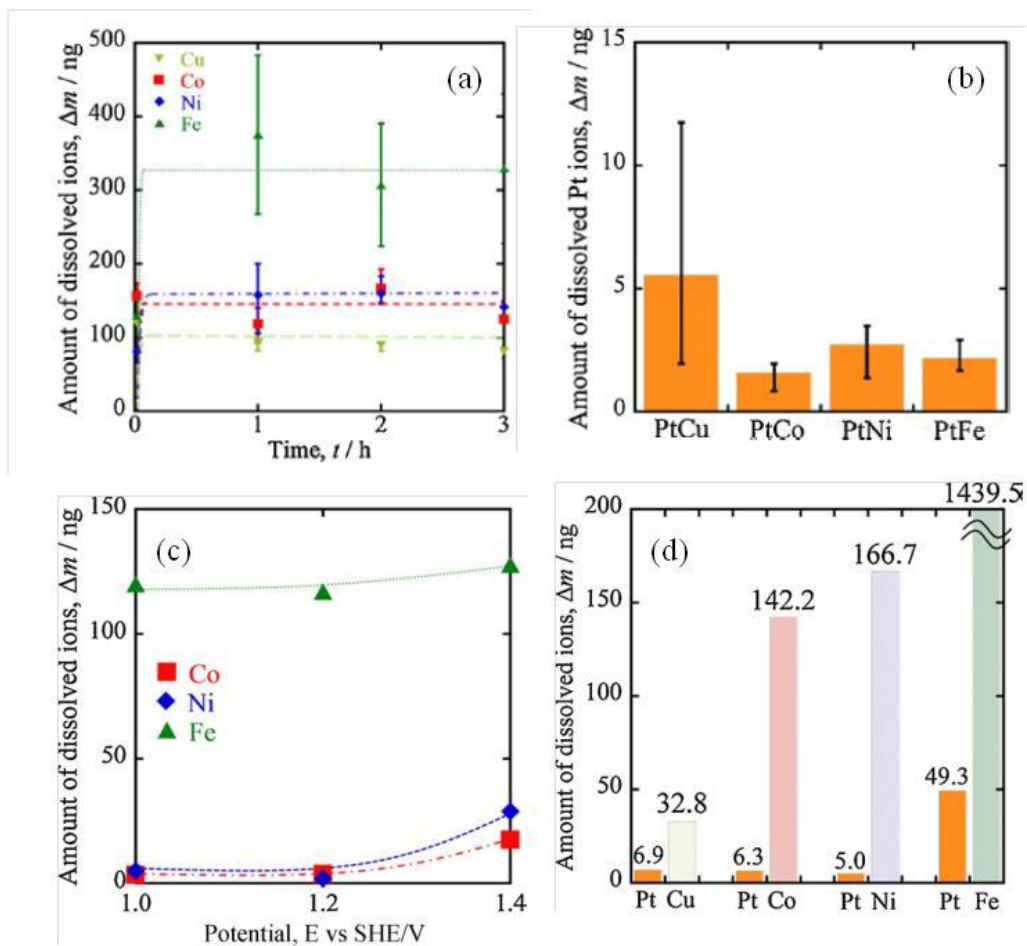


Figure 1.8 The amount of ions dissolved from the Pt–M alloys in 0.5M H₂SO₄ solution at 25 °C (a) dissolved M ions during 3 h-immersion test, (b) dissolved Pt ions after 3 h-immersion test. (c) dissolved M ions under the potentiostatic polarization at 1.0, 1.2 and 1.4 V. (d) dissolved M ions measured at the end of 100 cycles of CVs [16].

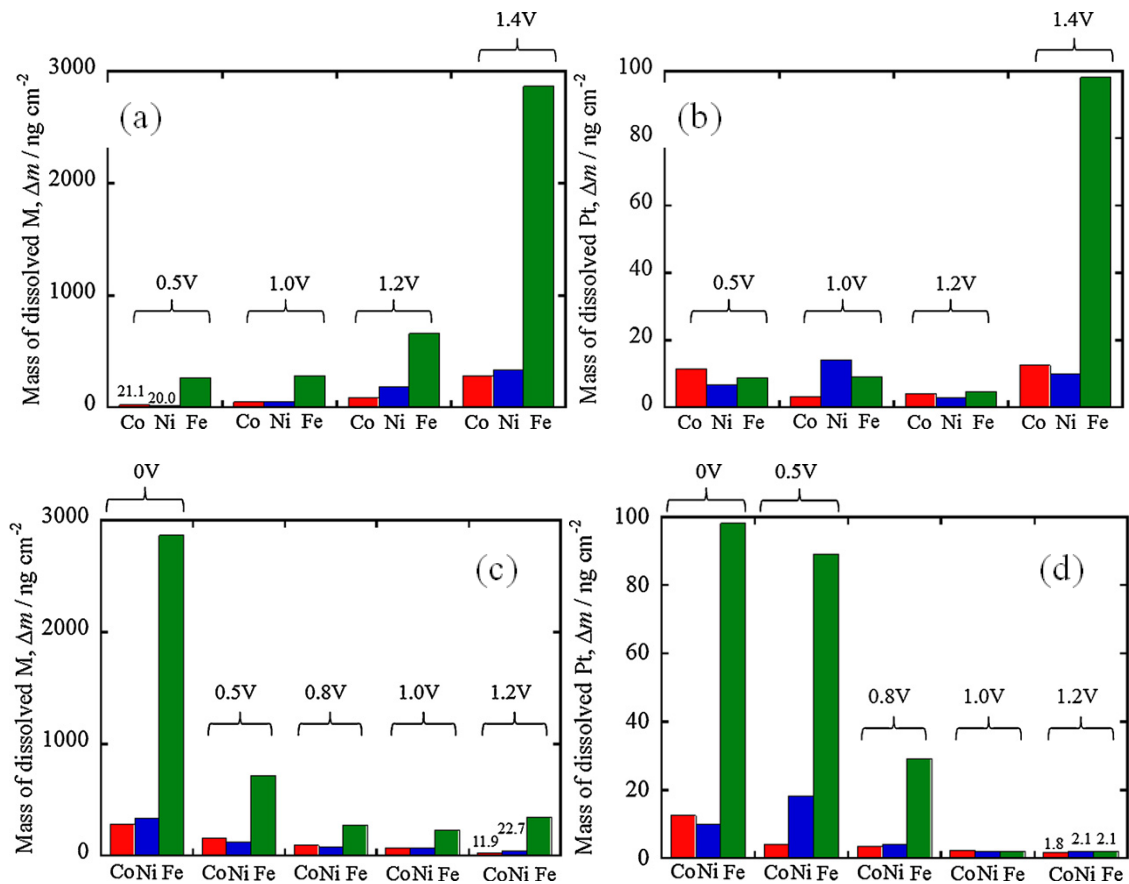


Figure 1.9 Effect of upper potential limit of CV on amounts of (a) M (= Co, Ni, Fe) and (b) Pt dissolved from the Pt–M alloys by 100 potential cycles. The lower potential limit was fixed at 0 V. Effect of lower potential limit of CV on amounts of (a) M (= Co, Ni, Fe) and (b) Pt dissolved from the Pt–M alloys by 100 potential cycles. The upper potential limit was fixed at 1.4 V [17].

much smaller. Regarding the effect of lower potential limit E_{lower} of the potential cycling with a common $E_{\text{upper}} = 1.4$ V, the amounts of the dissolved Co, Ni and Fe are very small amounts when the E_{lower} is 0.8, 1.0, and 1.2 V, while it is significantly increased when $E_{\text{lower}} = 0.5$ and 0 V, where Pt dissolution is also remarkably accelerated by potential cycling. Dissolution of M and Pt is accelerated by potential cycling in the potential range where formation of PtO_{ad} and the reduction occurs.

1.2.2 CARBON CORROSION

In addition to degradation of the catalysts, the carbon support that deposits the catalyst particles and provides electrical connection to the gas-diffusion media and bipolar plates also plays an important role in MEA degradation. Therefore, corrosion of carbon materials as catalyst supports for PEMFCs may give rise to electrical isolation of the catalyst particles as they are detached from the support, and result in aggregation of catalyst particles. Those results are attributed to a decrease in the electrochemical active surface area of the catalyst and an increase in the hydrophilicity of the carbon surface, which can, in turn, result in a decrease in gas permeability as the pores become more likely to be filled with liquid water films that can hinder gas transport [23]. As durability targets are established, graphitized carbons are being considered for use in PEMFCs due to the importance of carbon stability [24]. The carbon corrosion reaction in aqueous acid electrolytes including proton exchange membranes is shown as [25]



This reaction is thermodynamically feasible at the potential range where the fuel cell operates.

First, Stevens et.al investigated the thermal degradation of carbon and platinum supported on carbon in air at an elevated temperature [26]. Whereas the Black Pearls carbon is stable in air at temperatures as high as 195 °C, a high platinum loading can lead to a loss of more than 80% of all carbon, where the time needed to reach the maximum amount of combusted carbon is determined by the temperature and the platinum loading. At platinum loadings used in commercial PEMFC catalysts, i.e. 40 wt% and higher, the loss of carbon at the lowest experimental temperature, 125 °C, amounted to 15% after 1,000 h. From the relation between carbon loss and temperature, it was concluded that below 100 °C, thermal oxidation of platinum loaded carbon in air did not take place. Roen et al. [27] detected CO₂ in the cathode exhaust gas during CV with varying Pt mass fraction, catalyst type, and temperature. An Arrhenius plot indicated higher apparent activation energy for CO₂ production at the positive potential limit of the CV on 0% Pt (carbon-only) electrode than on 39% Pt/C electrode. It was concluded that platinum accelerated the corrosion rate of the carbon catalyst support. Additional studies showed that the humidification of air accelerated the thermal corrosion rate of carbon, by providing an additional pathway for chemical carbon oxidation through a direct reaction with water [28, 29]. Mathias et al. [30] reported the relation of carbon corrosion current on the potential, material, temperature, and time. The logarithm of the corrosion current related linearly with the logarithm of time.

Reiser et.al [31] proposed the reverse-current mechanism related to the local hydrogen starvation. During transient conditions of the cell operation such as start-up and shut-down, a high interfacial potential difference causes carbon corrosion as shown in Figure 1.10. When hydrogen is introduced into the anode during startup, a condition is

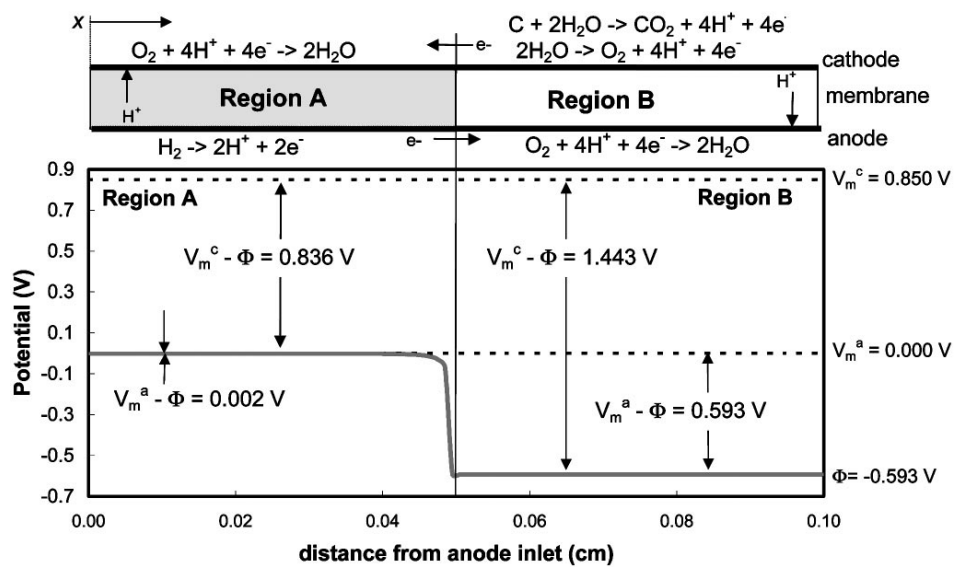


Figure 1.10 Potential distributions along anode flow path during reverse current conditions [31].

created where hydrogen occupies only part of the anode. At this moment, the carbon corrosion is occurred at the cathode. During the shutdown procedure, a similar phenomenon can be occurred, when the air from the outside or through the membrane, replaces the hydrogen causing carbon corrosion at the anode [31-35].

Fundamental studies on carbon corrosion have been carried out in aqueous electrolyte for a degradation mechanism [36-41]. Differential electrochemical mass spectroscopy (DEMS) shows that pure carbon is oxidized only at potentials higher than 0.9 V (RHE), and that Pt activation catalyzes the oxidation of a CO_{surf} surface layer to CO₂ at potentials between 0.6 and 0.8 mV (RHE) in sulfuric acid solution. This indicates that the carbon corrosion by Pt occurs in the neighborhood of the Pt-sites, thus damaging the Pt to carbon contact [36]. The membrane inlet mass spectrometry (MIMS) shows the formation of carbon oxidation products like CO₂, CO and HCOOH. The oxidation of carbon is accelerated in the presence of Pt [40]. In-situ electrochemical quartz crystal microbalance (EQCM) shows mass changes of a variety of carbon supports during the CV in deaerated 0.5M H₂SO₄ solution [42]. The mass change and corrosion onset potential during electrochemical carbon corrosion indicated oxide formation and accumulation on the carbon surface, leading to a mass increase. A decrease in the mass is associated with carbon loss from the gasification of carbon surface oxides into carbon dioxide. High surface area carbon blacks ECP 600 and ECP 300 have a carbon loss of 0.0245 ng cm⁻² s⁻¹ and 0.0144 ng cm⁻² s⁻¹ and as compared to 0.0115 ng cm⁻² s⁻¹ for low surface area support XC-72. Graphitized XC-72 and multi-walled carbon nanotubes (MWNTs), with higher graphitization have higher carbon corrosion onset potential at 1.65V and 1.62V and appear to be more intrinsically resistant to corrosion.

In Figure 1.11, electrochemical surface oxidation of carbon black (CB) was studied under the potentiostatic condition up to 120 h at various potentials from 0.6 to 1.2 V at room temperature and 65°C [37]. The presence of ether, carbonyl, and carboxyl surface oxide species that decreases the degree of hydrophobicity after electrochemical treatments was observed. In this study, the authors found that experiments at 65°C showed clear signs of surface oxidation after only 16 h at potentials > 0.8 V, while potential holds at 1.0 V at room temperature only resulted in slight oxidation of Vulcan XC-72. This verifies that surface oxides can be generated under simulated PEMFC operating conditions. Avasarala et.al have investigated the electrochemical oxidation of CB due to potential cycling between 0 and 1.2 V in 0.1 M perchloric acid at 60 °C, which simulates the operating condition in PEMFCs [43]. Using X-ray photoelectron spectroscopy (XPS), formation of several oxygen functional groups such as C=O, C–O–C, O–C=O on CBs were identified under potential cycling between 0 and 1.2 V for 16 h duration. The increase in hydroquinone-quinone redox couple and total surface oxygen on the surface of CB during potential cycling is much higher than that of the as-received CB. Potential cycling significantly increases the surface oxidation along with significant oxidation to gaseous oxides such as CO/CO₂ gases. The oxygen functional groups formed on the surface of the potentially cycled CB supports were found to be relatively higher compared to those exposed to ‘potential hold’ conditions.

Siroma et.al observed the carbon-corroded electrode by atomic force microscopy (AFM) and field emission-scanning electron microscopy (FE-SEM) studies using highly oriented pyrolytic graphite (HOPG) as shown in Figure 1.12 [38]. The formation of blisters on the surface of the model electrode is observed by AFM after it is kept at 1.0 V,

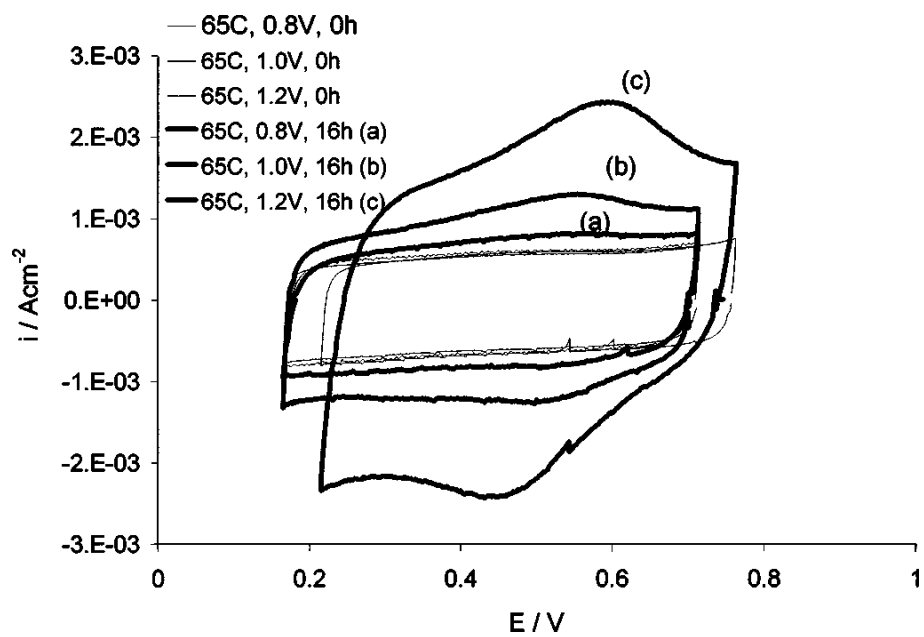


Figure 1.11 CVs of 10 wt% TFE-Vulcan composite after potential holds at 65 °C for 16 h at (a) 0.8, (b) 1.0, and (c) 1.2 V (sweep rate of 10 mV s⁻¹). The initial (0 h) CVs of the prefilled samples overlapped [37].

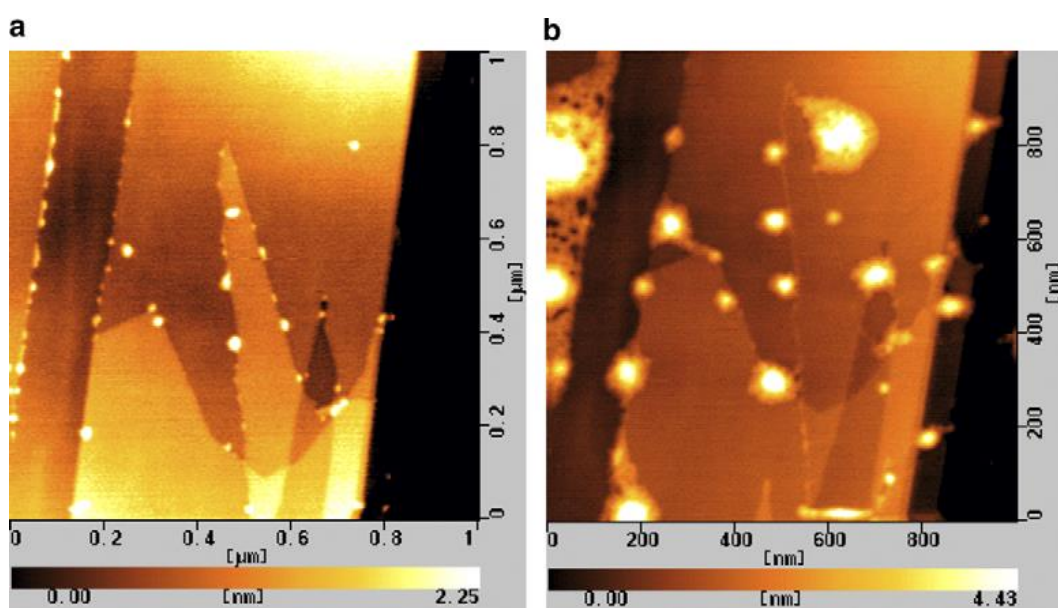


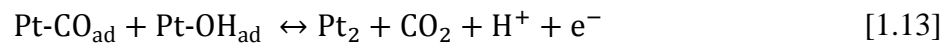
Figure 1.12 AFM images ($1 \mu\text{m} \times 1 \mu\text{m}$) of a Pt-catalyzed HOPG surface (a) before and (b) after potential retention at 1.0 V for 70 h in a 1.0 M HClO_4 solution [38].

especially at and around the Pt particles. FE-SEM observations using a backscattered electron detector revealed that the Pt particles remain unchanged at their original positions after the formation of blisters.

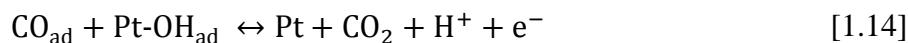
On the other hand, Kinumoto et.al investigated the effects of hydrogen peroxide on the degradation of Pt/C catalyst [39]. After immersed in acidic 1.0 mol l⁻¹ H₂O₂ solution at room temperature, many scars were formed by oxidative etching of HOPG and Pt-particle catalysts aggregated on the surface, while no surface change was observed without hydrogen peroxide. These resulted in significant deterioration of Pt/HOPG electrode and the active surface area of the Pt particles. Regarding the applied potential, the deterioration of the electrode was accelerated at potentials both more positive and negative than the open-circuit potential. Also, similar degradation phenomenon was observed when the potential was set at 0.1 V, at which a large amount of H₂O₂ is formed in oxygen reduction, in O₂-saturated H₂O₂-free acid solution for 5 days. Based on the results, they proposed the mechanism of Pt/C deterioration by hydrogen peroxide.



In the presence of Pt, an additional reaction can also be occurred [44]. Carbon monoxide is adsorbed on the metal surface at potentials below 0.55 V. At higher potentials, CO is oxidized to CO₂ according to following reaction.



Also, the overpotential of following reaction is decreased. This leads to an increase in corrosion rates compared to that of carbon only.



1.2.3 CARBON COMPOSITE CATALYST

The carbon composite catalyst (CCC) that was developed in Dr. Popov's laboratory has shown higher graphitized structure and better activity towards ORR than most of the commercially available CB supports. Most of the graphitic carbons like carbon nano-tubes are expensive. However, the CCC is made of cheap CB and nitrogen contained in the graphitic structure which produces the synergistic effect with noble metals like Pt.

The CCC was synthesized through the following three consecutive steps: (i) the deposition of transition metal-chelate complex, and (ii) the high-temperature pyrolysis, and (iii) the chemical post-treatment. Transition metals such as Co and Fe were used to facilitate and stabilize the incorporation of nitrogen within the carbon matrix.

The nitrogen atom in the CCC enhances the ORR activity. Many investigations on non-precious metal catalyst have shown the vast development using nitrogen active site for ORR. According to the earlier reports [45-53], their results agree with points in common as follows: (i) Active sites were formed in the presence of transition metal, carbon, and nitrogen, (ii) The nitrogen sites are believed as active sites for ORR, (iii) The Co and/or Fe are the effective metal to give a high activity for the carbon, (iv) The carbon heat-treated at 600 – 900 °C shows the high activity, and (v) The stability is increased as the temperature exceeds 900 °C.

Figure 1.13 shows the LSV diagrams of oxygen reduction on the CCC with different treatments [52]. One catalyst is heat-treated at 900 °C, while another is treated by a series of heat-treatment at 900 °C, leaching, and re-heat-treatment at 900 °C. The LSV was performed in O₂-saturated 0.5 M H₂SO₄ solution at a scan rate of 5 mV s⁻¹ and a rotation speed of 900 rpm. The oxygen reduction current on the catalyst that was heat-treated twice is higher than that heat-treated once, while the onset potential of oxygen reduction is same on both catalysts (ca. 0.85 V vs. NHE). As shown in Figure 1.14, the polarization curves of PEM fuel cells using those catalysts as a cathode shows the same performance as appeared in LSV measurements [52]. The observed activity difference between two catalysts may be explained as follows: the active sites of catalysts were formed at the first pyrolysis at high temperature. At the same time, inactive residues on the surface such as metals and metal oxides produced in the heat-treatment process cover and hinder the active site of catalyst surface. To remove those species, the acid leaching process is efficiently applied, resulting in ~ 40% weight loss of the catalysts. As a result, the catalyst heat-treated twice shows the better current density for the ORR.

According to the literature [54-58] and previous characterization studies [51, 53, 59-61] on the non-precious metal catalysts, high temperature pyrolysis produces the pyridinic and quaternary-type nitrogen on the surface of the carbon substrate. A strong Lewis basicity of such nitrogen-modified sites facilitates the reductive adsorption of oxygen without the irreversible formation of oxygen functionalities, due to an increased electron-donor property of carbon [56].

The long-term stability of CCC is shown in Figure 1.15. The catalysts were heat-treated at 800 °C (denoted as NMCC-800) and 1100 °C (denoted as NMCC-1100),

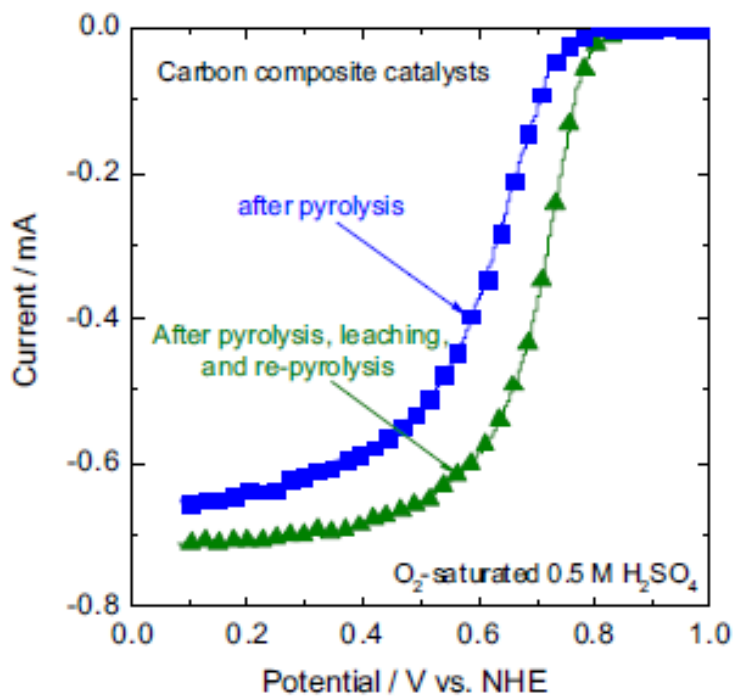


Figure 1.13 LSV curves of CCC treated by a pyrolysis alone and by a series of pyrolysis, leaching and 2nd pyrolysis. The measurements were performed in O₂-saturated 0.5 M H₂SO₄ solution using a potential scan rate of 5 mV sec⁻¹ and an electrode rotation rate of 900 rpm [52].

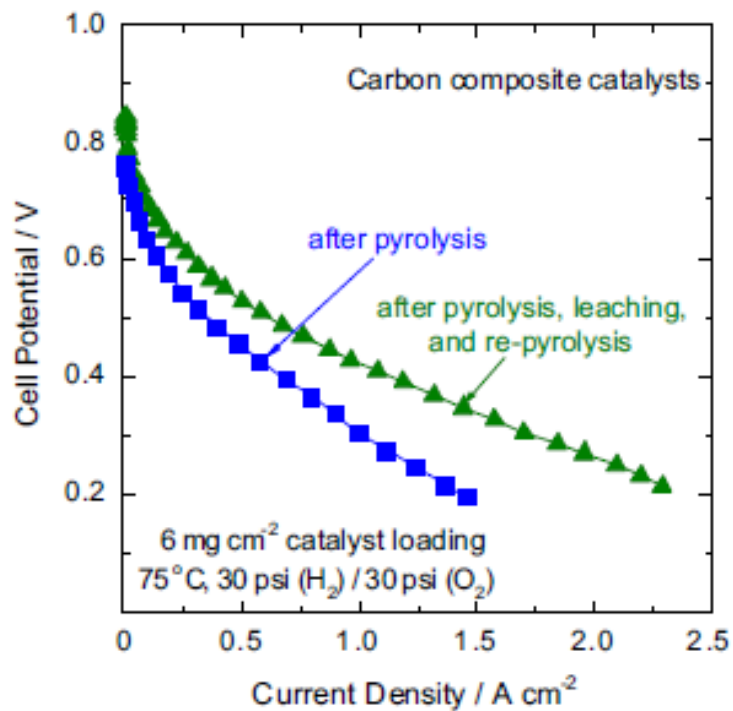


Figure 1.14 Polarization curves of PEMFCs prepared with CCC as a cathode treated by a pyrolysis alone and by a series of pyrolysis, leaching and 2nd pyrolysis. The CCC loading is 6 mg cm⁻². The test was run with H₂/O₂ back pressure of 30 psi/30 psi. The fuel cell operating temperature is 75 °C [52].

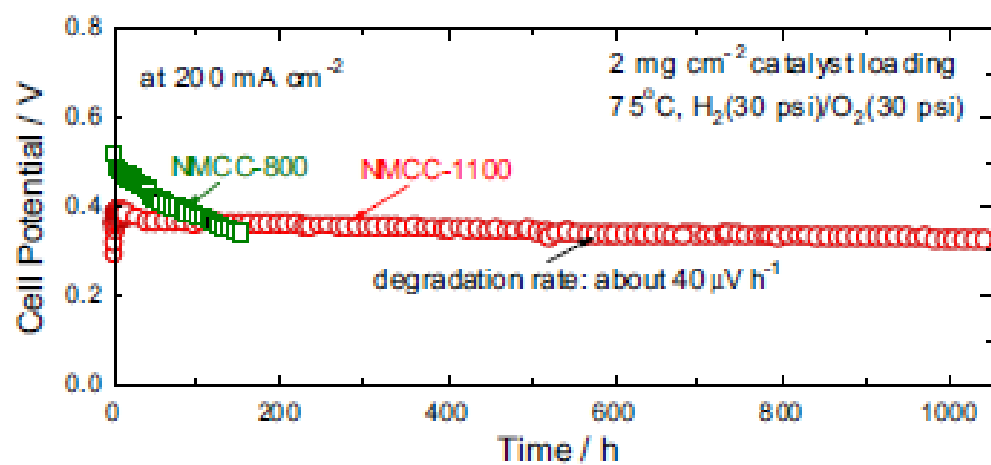


Figure 1.15 Long-term fuel cell stability test measured on the carbon composite catalysts at 200 mA cm^{-2} [62].

respectively. NMCC-800 shows a better initial activity, while its stability is very poor. This phenomenon has been evidenced previously by other research groups [47, 50, 63]. The NMCC-800 showed fast degradation in a range of 0 to 150 h. The NMCC-1100 showed much better stability than NMCC-800 at the 0 to 150 h. For example, from 6 to 16 h, NMCC-800 degraded at a rate of 980 mV h^{-1} while NMCC-1100 decreased at a rate of 400 mV h^{-1} . Since 16 h-operation, NMCC-1100 degraded at a rate of 40 mV h^{-1} .

According to the literatures [48, 63, 64] and previous studies [52, 59-61], the stability of catalysts is strongly dependent on the heat-treatment temperature. The hydrophilicity of the catalyst depending on pyrolysis temperature may strongly affect the water management and thus mass transfer in the cathode catalyst layer. It has been reported that the fast degradation may be attributed to the loss of the pyridinic-N sites which are alkaline in nature and react in a matter of minutes with the protons present at the cathode electrolyte interface; the slow decay is due to further loss of active sites through the oxidation decomposition of CCC under corrosive conditions, such as low pH, high temperature, high water content, high potential, high oxygen concentration, and hydrogen peroxide produced during the ORR [62]. The performance decay may also result from water flooding in the cathode due to the hydrophilic property of the catalyst and the thickness of cathode catalyst layer.

1.3 OBJECTIVES AND OUTLINE

The objective of this dissertation is to develop a novel technology based on a novel hybrid cathode catalyst (HCC) process in which a highly active compressive Pt-lattice catalyst is formed by the interaction of Pt with electrochemically active, transition-

metal-containing CCC. The proposed HCC method is a novel method to prepare the compressive Pt-lattice catalyst since both the carbon support and metal catalyst are electrochemically active for ORR and the transition metal required for the formation of highly active compressive Pt catalyst is encapsulated within the graphitic carbon structure. Our novel catalyst synthesis procedure avoids the chemical leaching step thus enhancing the stability under high potentials.

In chapter 2, the synergetic effect of Pt and CCC was investigated. Variety of characterization techniques such as XPS, XRD, HR-TEM, and RDE together with fuel cell testing were carried out to study the structure-property relationship of the synthesized catalyst. RDE studies of the CCC chelated with nitrogen-containing organic compound showed a high electrochemical activity for ORR in 0.1 M HClO₄ electrolyte. Moreover, the Pt nanoparticles deposited on CCC as a support exhibited better ORR performance than the conventional Pt/C catalyst.

In chapter 3, the HCC based on a novel catalyst synthesis process was optimized with respect to the annealing temperature. The catalyst stability was measured in 25 cm² MEAs under PEM fuel cell operating conditions which revealed higher activity and stability for the HCC than the one prepared using conventional impregnation process.

In chapter 4, the support stability of heat-treated CB was investigated under potential cycling (1-1.5 V) conditions. Raman spectroscopy and XRD are employed to analyze the effects of temperature on the structure and electrochemical stability of the heat-treated CB supports. The catalyst stability was evaluated by measuring the polarization curves under H₂/Air atmosphere before and after potential cycles.

In chapter 5, a novel method for the preparation of Co-doped Pt was employed to make supported catalyst using heat-treated, graphitized CB as support. The prepared catalyst was subjected to physical characterization tools such as XPS, XRD, HR-TEM, and the performance was evaluated using polarization studies. The stability of catalyst is enhanced at high potential (1-1.5 V) while the catalyst stability is remained under PEMFC operating conditions.

CHAPTER 2

SYNERGISTIC EFFECT OF CCC AND PT CATALYST

2.1 INTRODUCTION

Recently polymer electrolyte membrane fuel cells (PEMFCs) are emerging as a promising candidate for automotive industries. Still the cost reduction is critically necessary for commercializing PEMFCs. To reduce the overall cost, the activity and stability of ORR catalyst should be further improved. In general, the cathode catalyst development focuses on two specific areas namely highly-active and stable Pt-based catalyst development and highly-stable catalyst support development to withstand the harsh operating environment of automotive PEMFCs. In this regard, research has been focused on the development of various Pt-alloy cathode catalysts such as PtCo, PtNi, and PtFe and more corrosion-resistant graphitic carbon supports such as carbon nanotubes (CNTs), carbon nanocages (CNCs), and carbon nanofibers (CNFs). The above-mentioned graphitic carbon supports are chosen as alternative cathode catalyst support since the conventionally used CB is easily subjected to corrosion under PEMFC operating conditions like low pH at the cathode interface, high operating temperature ($> 80\text{ }^{\circ}\text{C}$), and high cathode interface potential (1.2-1.5 V). The selection of graphitic carbons as alternative support is not viable due to their high cost. Therefore, it is necessary to develop a catalyst consisting of catalytically-active support and Pt-based catalyst to

significantly reduce the cost while retaining ORR catalytic activity and stability under PEMFC operating conditions.

In this chapter, a novel approach for the preparation of cost-effective, highly-active, and stable carbon-based support HCC and its synergistic effect towards ORR is reported. HCC is a combination of pyridinic site-containing CCCs and platinum catalytic sites for oxygen reduction. Besides its own contribution to the overall catalyst activity (an advantage over conventional CB supports), the noble metal-free CCC can also enhance the activity of the Pt through synergistic effects. The enhanced activity of HCC is demonstrated both in half-cell using 0.1 M HClO₄ as electrolyte and in 25 cm² MEAs.

2.2 EXPERIMENTAL

2.2.1 PREPARATION OF SUPPORT AND CATALYST

For a typical CCC preparation [51-53, 61, 65], 2 ml of the ethylenediamine was chelated with iron (III) nitrate nonahydrate (Fe(NO₃)₃·9H₂O) and cobalt (II) nitrate hexahydrate (Co(NO₃)₂·6H₂O) in isopropyl alcohol (IPA). 0.4 g of pre-oxidized CB (Ketjen Black EC-300J) was added to the chelating solution followed by refluxing at 85 °C for 3 h. The solvent was removed by rotary evaporating and the product was dried in an air oven at 80 °C for 12 h. Subsequently, the resultant mass was pyrolyzed in a tube furnace under the pure nitrogen atmosphere for 1 h. After cooling down to room temperature, the sample was leached in 0.5 M H₂SO₄ at 80 °C for 8 h to remove the unreacted transition metals present on the surface. The CCC was obtained after washing and drying at 80 °C overnight. 5 wt% Pt on the CCC was deposited by the electroless deposition using sodium formate as a reducing agent. 5 wt% Pt on high surface area carbon (denoted as Pt/CB) was prepared using the same method as Pt/CCC using CB

(Ketjen Black EC-300J) as a support. Also 30 wt% Pt was deposited by the same method on both supports for comparison studies in fuel cell.

2.2.2 PHYSICAL CHARACTERIZATION

The nitrogen adsorption/desorption isotherms were obtained at $-196\text{ }^{\circ}\text{C}$ using a Quantachrome NOVA 2000 BET analyzer. Specific surface area was determined by a multipoint Brunauer-Emmett-Teller (BET) analysis. Pore size distribution (PSD) curves were calculated by the Barrett-Joyner-Halenda (BJH) method using the adsorption/desorption branch. X-ray diffraction (XRD) analysis was performed using a Rigaku D/Max 2500 V/ PC with a $\text{Cu K}\alpha$ radiation. A tube voltage of 30 kV and a current of 15 mA were used during the scanning. To estimate the particle size of samples, we employed the following Scherrer equation [66]:

$$D = \frac{k\lambda}{10B \cos \theta} \quad [2.1]$$

where D is the crystallite size in nm, k is a coefficient (0.9), λ is the wavelength of X-ray (1.5404 \AA), B is the line broadening at half the maximum intensity in radians, and θ is the angle at the position of the maximum peak known as Bragg angle. High resolution transmission electron microscope (HR-TEM) was used to study the morphology and particles size distribution of the catalysts using Hitachi 9500 HR-TEM operated at 300 kV accelerating voltage. X-ray fluorescence (XRF, Fischer XDAL) was used to determine Pt loading in the catalyst coated membrane.

2.2.3 ELECTRODE PREPARATION

In a typical RDE experiment, for the CCC, 8 mg of CCC was ultrasonicated in 1 ml of IPA. 15 μl of the ink ($0.12\text{ mg}_{\text{CCC}}\text{ cm}^{-2}$) was deposited on the glassy carbon

electrode. In the case of Pt/CCC and Pt/CB, the catalyst ink was prepared by mixing the respective catalysts with absolute ethanol and DI water in an ultrasonic bath. The catalyst ink was deposited onto the glass carbon electrode with a target Pt loading of $20 \mu\text{g}_{\text{Pt}} \text{cm}^{-2}$. For all RDE tests, $5 \mu\text{l}$ of 0.25 wt% ionomer (Alfa Aesar) was additionally deposited on the catalyst layer to give a good adhesion of catalyst onto the glassy carbon electrode.

For the MEA fabrication, the in-house synthesized Pt/CCC catalyst was employed as the cathode catalyst while commercial 46% Pt/C (Specifications of TKK catalyst) was used as a catalyst for the anode. Catalyst inks were prepared by ultrasonically mixing the respective catalysts (32 mg), IPA (1.8 ml), Nafion[®] ionomer (5% solution, Alfa Aesar), and DI water (0.2 ml). The ionomer content was 30% and 20% in the anode and cathode inks, respectively. The catalyst inks were sprayed directly on the Nafion[®] 212 membrane. The Pt loading on the anode is kept at 0.1 mg cm^{-2} , while the cathode Pt loading is varied from 0.04 to 0.15 mg cm^{-2} . The catalyst coated membrane was then hot pressed at $140 \text{ }^\circ\text{C}$ using a pressure of 20 kg cm^{-2} for 6 min. in between the gas diffusion layers (Sigracet GDL 10BC, SGL) and Teflon gaskets to prepare the MEA for the performance evaluation studies in fuel cell. For the comparison, Pt/CB as a cathode was used at the Pt loading of 0.04 and 0.15 mg cm^{-2} .

2.2.4 ELECTROCHEMICAL MEASUREMENT

Electrochemical experiments of the CCC and Pt/CCC were performed in a rotating disk electrode (RDE) setup using a Pine bi-potentiostat (Model AFCBP1). A glassy carbon disk (0.247 cm^2) was acted as a working electrode. The Ag/AgCl electrode

and platinum mesh were used as a reference and counter electrodes, respectively. All electrode potentials reported here were converted into the reversible hydrogen electrode (RHE). RDE tests were performed in 0.1 M HClO₄ solution as an electrolyte at the room temperature. The CV was swept at a scan rate of 50 mV s⁻¹ from 0.005 to 1.0 V in deaerated electrolyte under N₂ atmosphere. Linear sweep voltammetry (LSV) measurements were conducted at a scan rate of 5 mV s⁻¹ in O₂-saturated electrolyte by sweeping the potential between 0.2 and 1.1 V anodically. The LSV curves presented in this work are properly corrected using the background capacitance current that is measured in the N₂ atmosphere at a scan rate of 5 mV s⁻¹.

For the PEMFC test, the MEA was activated under a supply of H₂ and O₂ at 80 °C to the anode and cathode compartments, respectively with a flow rate of 750 ml min⁻¹ and 100% relative humidity (RH). After MEA activation, the mass activity at 0.9 V_{iR-free} was evaluated under H₂/O₂ (2/9.5 stoic.) at 80 °C, 100% RH, and 150 kPa_{abs.} back pressure. The fuel cell polarization was conducted using a fully automated fuel cell test station (Scribner Associates Inc., model 850e) at 80 °C.

2.3 RESULTS AND DISCUSSION

2.3.1 CCC SUPPORT SYNTHESIS

Figure 2.1 (a) and (b) show the nitrogen adsorption-desorption isotherms and BJH PSD curves of CCC and CB. The specific BET surface area of CCC and CB are 231.9, and 826.4 m² g⁻¹, respectively. The CCC exhibits characteristic Type IV adsorption/desorption isotherm behavior according to IUPAC (The International Union of Pure and Applied Chemistry) classification indicating its mesoporous nature [67]. The

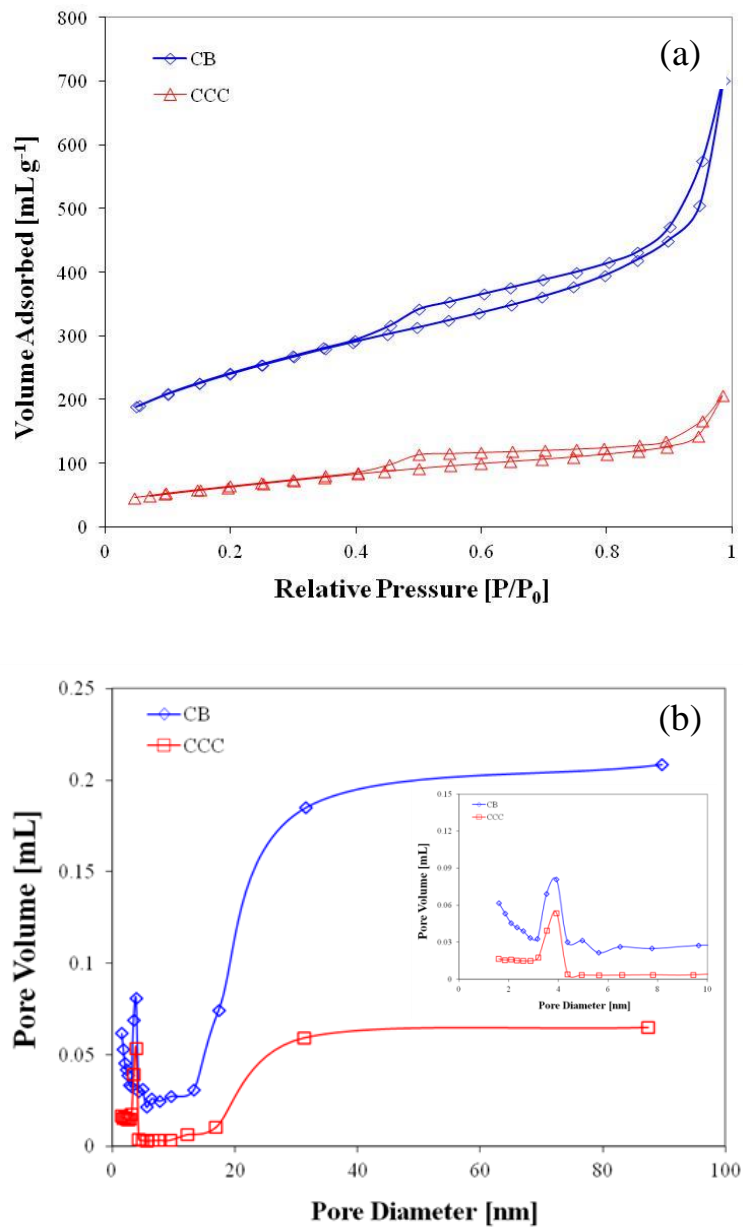


Figure 2.1 (a) N_2 adsorption/desorption isotherms and (b) BJH pore-size distribution curves obtained from the adsorption branch of CB and CCC. The inset in (b) compares the PSD in the range 0-10 nm.

isotherms show hysteresis loop with sharp adsorption and desorption branches over a relative pressure range of 0.4-0.8. The nitrogen uptake is observed when (P/P₀) ratio is 0.94-1.0, which indicates the presence of mesopores [67]. As shown in Figure 2.1 (b) inset, after the metal-catalyzed pyrolysis the peak pore diameter is ca. 4 nm, which is the same as that of CB.

Figure 2.2 (a) presents XRD patterns of the CCC and CB. In general, the characteristic diffraction peaks of (002) and (101) planes for graphite are found at ca. 26 and 43° (PDF#97-003-1829). The diffraction peaks of CCC are sharper with increased intensity and slightly shifted to higher angles. Consequently, the interlayer spacing of CCC based on (002) plane decreases to 0.3437 nm, while that of CB is 0.3615 nm. The results indicated that the surface of CCC has been partially graphitized during metal-catalyzed pyrolysis. Furthermore, the CCC shows characteristic diffraction peaks at 44.45° which corresponds to the (110) plane of body-centered cubic (BCC) structure of FeCo metal particle (PDF#49-1568), respectively.

The HR-TEM images of CCC and CB are shown in Figure 2.3 (a) and (b), respectively. The apparent difference between them is the presence of FeCo particles encapsulated by graphitic carbon shells in the CCC support. The graphitic carbon shells derived from EDA protects FeCo particles, while the FeCo particles present on the surface are removed during acid leaching. Nanostructured fibers or tubes of graphitic carbon are also formed as a result of pyrolysis in the presence of Fe and Co metals [55, 56] while KB showed amorphous morphology as shown in Figure 2.3 (b).

The results of XPS analysis performed on CCC and CB supports are presented in Figure 2.4 (a) and (b), respectively. Figure 2.4 (a) shows the survey scans for CCC and

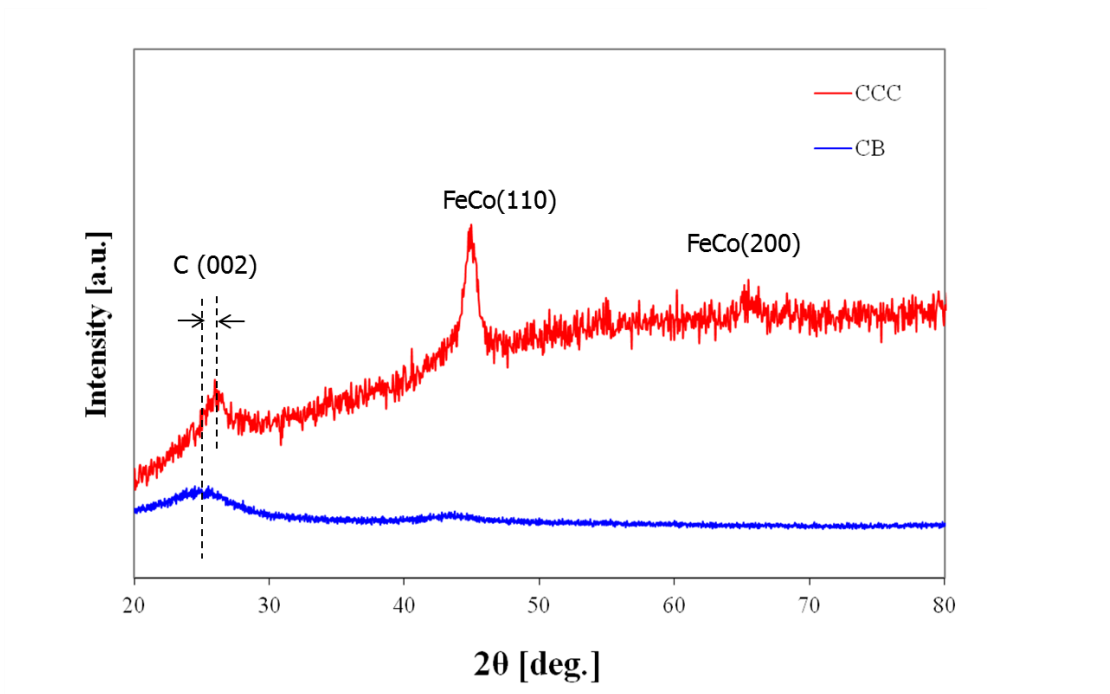


Figure 2.2 Comparison of XRD patterns of CCC and CB.

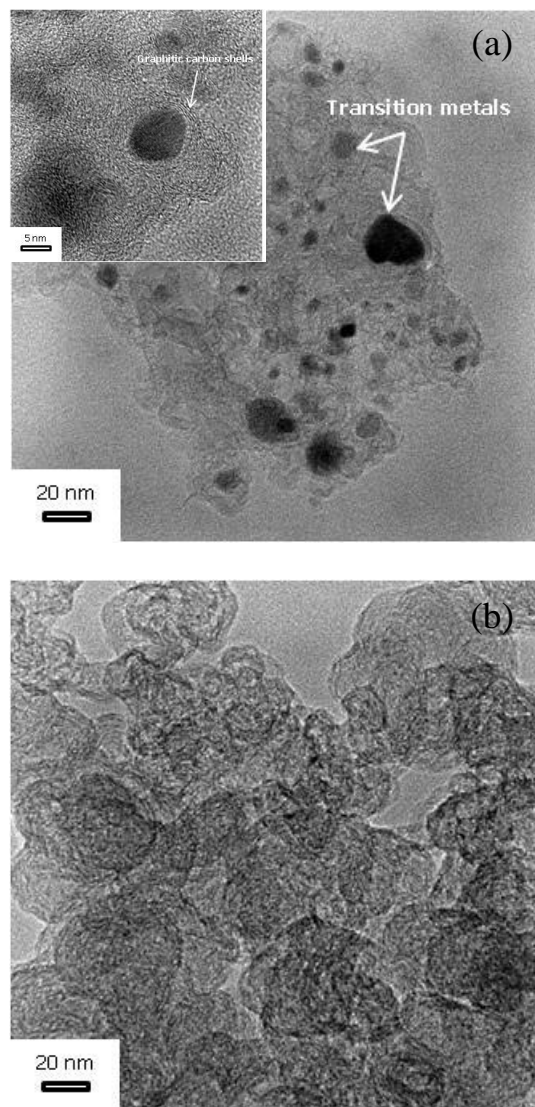


Figure 2.3 HR-TEM images of (a) CCC and (b) CB.

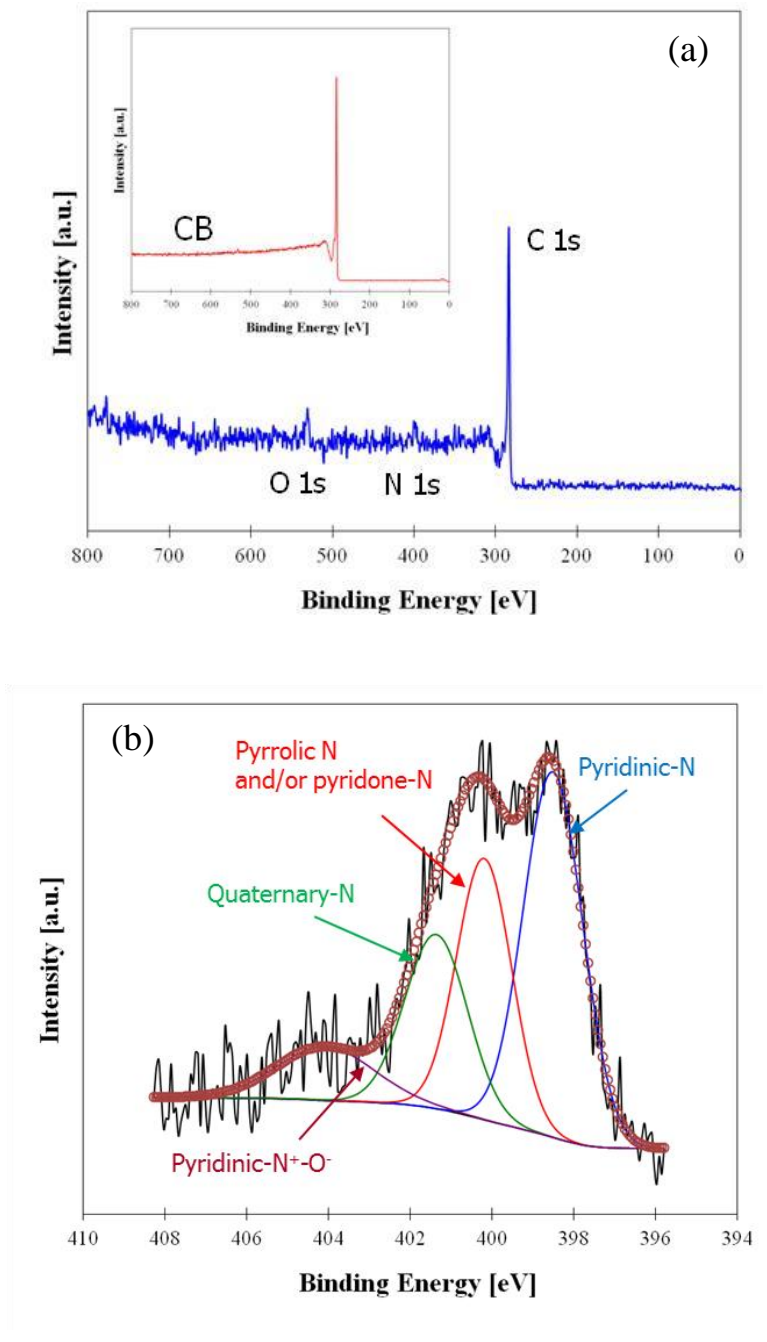


Figure 2.4 (a) XPS survey scans of CCC and CB and (b) deconvoluted N1s XPS spectra of CCC.

CB. The XPS spectrum of CCC alone, as shown in Figure 2.4 (b), represents a peak around 398.4 eV which corresponds to the nitrogen atom. The nitrogen peak shown in Figure 2.4 (b) for CCC can be deconvoluted into four major peaks corresponding to pyridinic, pyrrolic and/or pyridone, quaternary, and pyridinic-N⁺-O⁻ (oxidized nitrogen). The peak at 398.5 eV accounts for the presence of pyridinic-N whereas the peak at 400.2 eV corresponds to the pyrrolic-N and/or pyridine-N. The peaks at 401.4 and 404.1 eV are ascribed to the presence of quaternary-N and pyridinic-N⁺-O⁻, respectively. Relative percentages of pyridinic-N and pyrrolic-N and/or pyridine-N are 41.7 and 27.5 % of total nitrogen, respectively. Quaternary-N accounts for 21.0 % while pyridinic-N⁺-O⁻ occupies 9.9%. It is well-known that pyridinic-N situated on the edge of the graphite planes promotes ORR by donating one p-electron to the aromatic π system [55, 68, 69]. Moreover, previous studies report that the quaternary-N plays a role as stable ORR active sites [55, 56, 61, 70]. The results for the deconvolution of the N 1s spectra are summarized in Table 2.1.

The electrochemical characteristics of CCC, CB, and Pt/C in 0.1 M HClO₄ at room temperature using three-electrode electrochemical cell are shown in Figure 2.5. The CV in Figure 2.5 (a) was performed at a scan rate of 50 mV s⁻¹ by sweeping the potential between 0.005 V and 1.0 V in N₂-saturated electrolyte. Unlike CB, CCC exhibits the quinone/hydroquinone redox coupling at 0.6 V. Interestingly, the oxidation current of CCC decreases with sweeping 0.8 to 1.0 V, while that of CB increases. LSV in Figure 2.5 (b) was measured at a scan rate of 5 mV s⁻¹ in O₂-saturated electrolyte by sweeping potential between 0.2 and 1.1 V in the anodic direction. The rotation speed was 1600 rpm for LSV measurement. The LSV curves presented in this work are properly

Table 2.1 Characteristics of CCC obtained from XPS N1s peak

	BE [eV]	FWHM	Relative intensity [%]
Pyridinic- N	398.5	1.711	41.7
Pyrrolic N and or pyridone-N	400.2	1.581	27.5
Quaternary-N	401. 4]	1.806	21.0
Pyridinic-N ⁺ -O ⁻	404.1	2.785	9.9

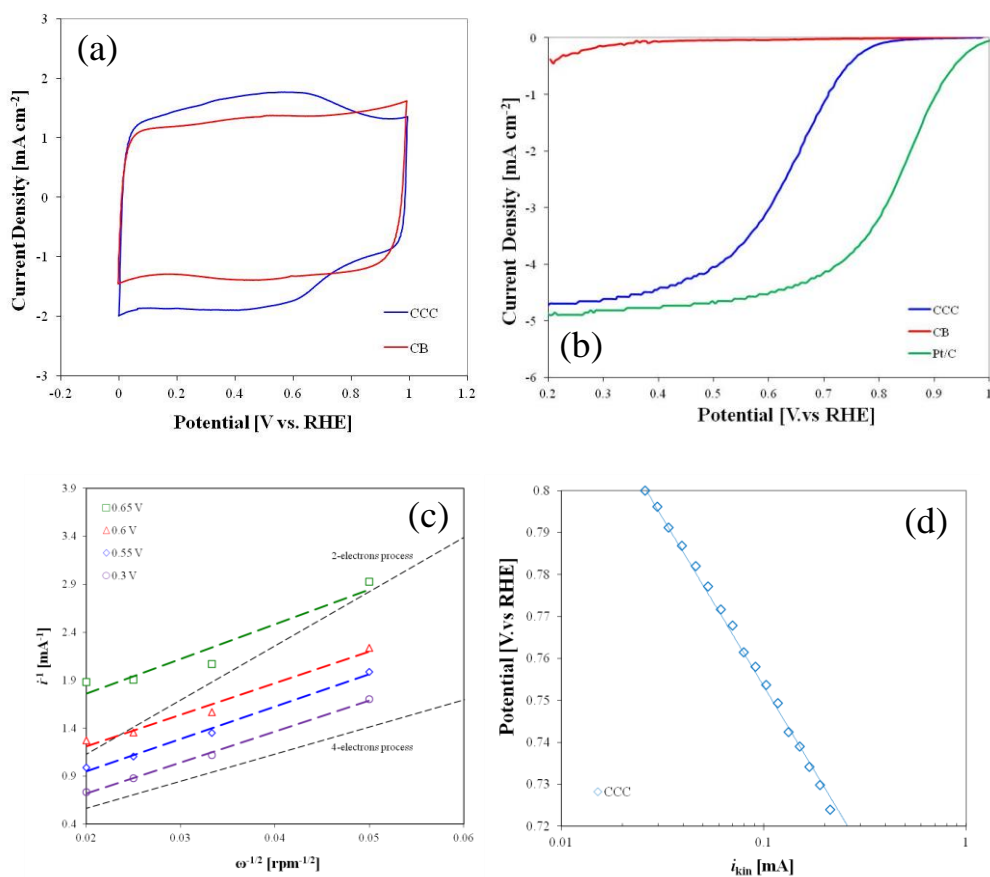


Figure 2.5 (a) CV diagrams of CCC and CB in N_2 -saturated 0.1 M HClO_4 at room temperature and scan rate of 50 mV s^{-1} . (b) LSV curves of Pt/C, CCC and CB in O_2 -saturated 0.1 M HClO_4 at room temperature and scan rate of 5 mV s^{-1} with 1600 rpm. (c) The Koutechy-Levich plots from LSV data of CCC at different potentials. (d) Tafel plot from LSV data of CCC at 1600 rpm.

corrected using the background capacitance current that is measured in the N₂ atmosphere at a scan rate of 5 mV s⁻¹. Figure 2.5 (b) shows that the CCC exhibits better activity than CB. The on-set potential is significantly enhanced by ca. 0.5 V as compared to the CB. The half-wave potential of the CCC is 0.640 V. The diffusion-limited plateau is well-defined, which indicates that the active sites are evenly distributed over the CCC. Figure 2.5 (c) exhibits the Koutechy-Levich plot derived from LSV curves with different rpm by means of the following equations:

$$\frac{1}{i} = \frac{1}{i_k} + \frac{1}{i_{dl}} \quad [2.2]$$

$$i_{dl} = B\omega^{1/2} \quad [2.3]$$

$$B = 0.62nFC_{O_2}D_{O_2}^{2/3}\nu^{-1/6} \quad [2.4]$$

where i is the measured current density, i_k is the kinetic current density, i_{dl} is the diffusion-limited current density, B is the Levich slope, n is the number of electron exchanged in ORR, F is the Faraday constant, C_{O_2} is the bulk concentration of oxygen (1.3×10^{-6} mol cm⁻³), D_{O_2} is the diffusion coefficient of oxygen in the bulk solution (1.7×10^{-5} cm² s⁻¹), ω is the rotation rate in rpm, and ν is the kinematic viscosity of the solution (0.01 cm² s⁻¹). As a result, the calculated n values of CCC at 0.3-0.65 V is ca. 3.7 indicating the 4-electron ORR process on CCC. With 2-electron process, the catalytic poison species, H₂O₂, is produced and degrades the membrane and carbon support [71]. The Tafel plot obtained from the LSV curves that are corrected for diffusion effects using Eq. (2.5) is shown in Figure 2.5 (d).

$$i_k = \frac{i_{dl} \cdot i}{i_{dl} - i} \quad [2.5]$$

As shown in Figure 2.5 (d), the Tafel slope is about 81 mV dec^{-1} at low current density. This value may be attributed to the transfer of the first electron as the rate-determining step and the Temkin conditions of intermediate adsorption [72].

2.3.2 Pt/CCC ELECTRO-CATALYST SYNTHESIS

Figure 2.6 shows the XRD patterns of Pt/CCC and Pt/CB which indicated that the Pt is present on CCC as a single element without making the alloy with transition metal encapsulated within the CCC since the peaks at $2\theta = 39.8, 46.7, 67.7,$ and 81.2° are corresponding to the (111), (200), (220), and (311) planes of face-centered cubic (FCC) Pt, respectively. As shown in Figure 2.2, peaks at 44.45 and 55° correspond to the (110) and (200) planes of BCC-FeCo. The particle size calculated by Scherrer equation using Pt(111) plane indicated 3.3 nm for Pt/CCC and 2.4 nm for Pt/CB catalysts.

Figure 2.7 (a) and (b) represent HR-TEM images of Pt/CCC and Pt/CB. The HR-TEM images reveal that the Pt nanoparticles are successfully deposited on the graphitized CCC support. For each samples, approximately 100 particles were analyzed to obtain the mean particle size. The mean particle size of Pt/CCC is 2.1 nm , while that of Pt/CB is 2.0 nm . The particles are evenly deposited on both the supports. The Pt/CB shows a good agreement with particle size from XRD but the Pt/CCC represents a big difference since FeCo peaks interfere with the unique Pt peaks during half-width calculation required for particle size measurement using Scherrer equation.

Figure 2.8 presents the XPS spectra for Pt/CCC and Pt/CB catalysts. The XPS is a powerful technique to analyze the oxidation states of metals on the catalyst surface. Figure 2.8 (a) and (b) shows the Pt 4f spectra of Pt in Pt/CCC and Pt/CB catalysts,

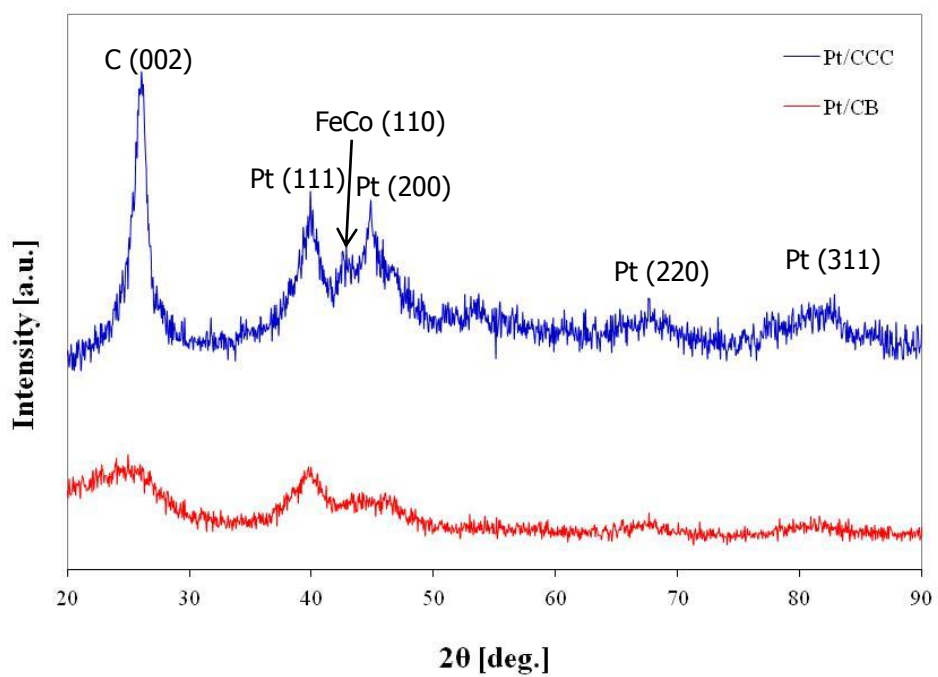


Figure 2.6 Comparison of XRD patterns of Pt/CCC and Pt/CB catalysts.

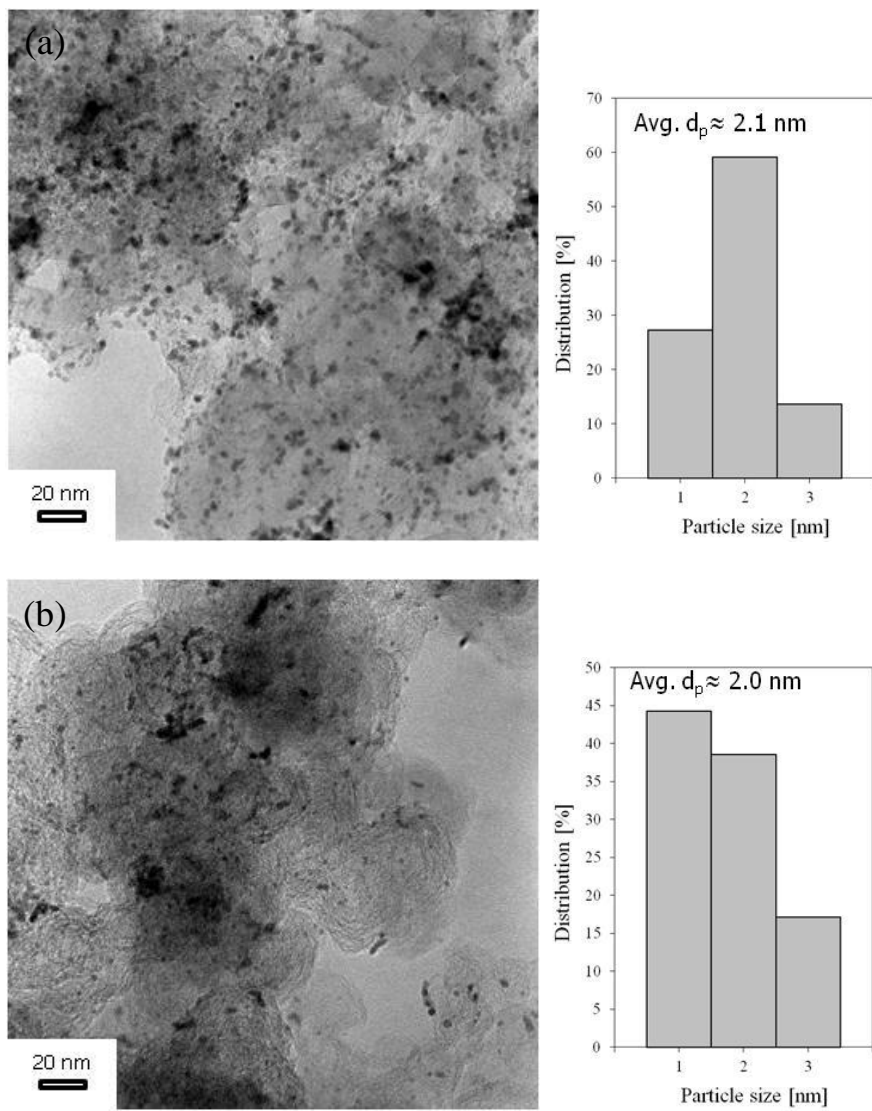


Figure 2.7 HR-TEM images of (a) Pt/CCC and (b) Pt/CB catalysts.

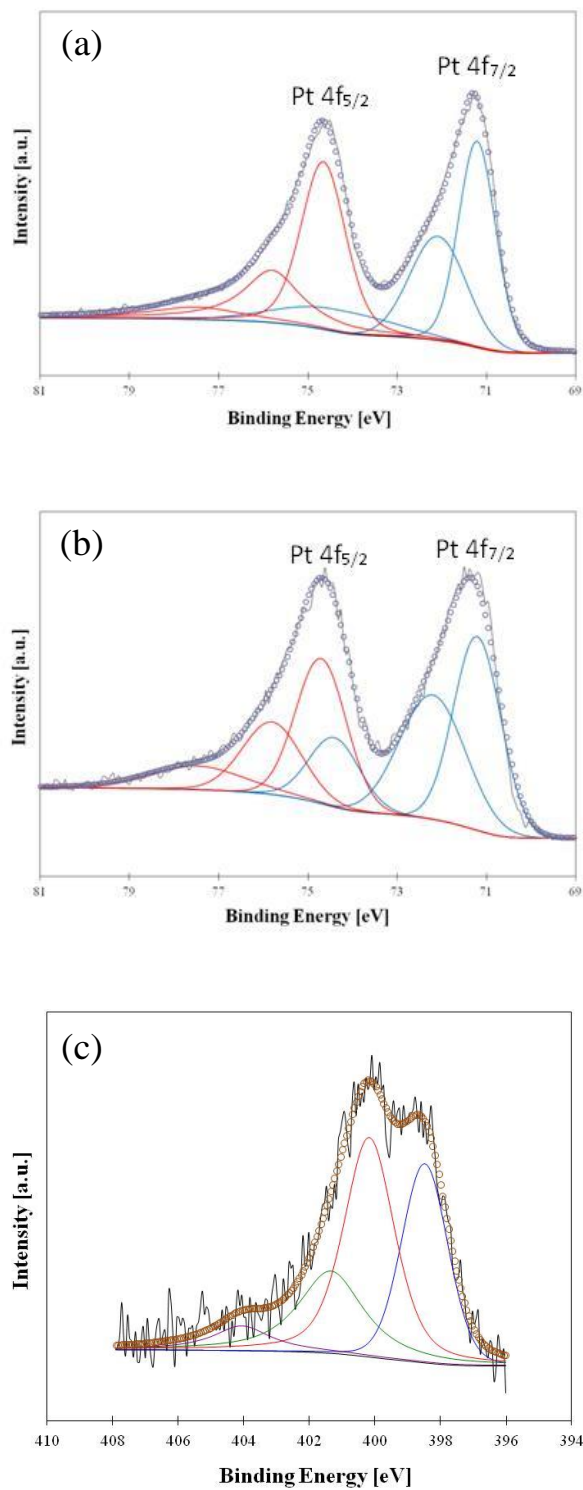


Figure 2.8 Deconvoluted XPS spectra of Pt4f in (a) Pt/CCC and (b) CB. (c) Deconvoluted XPS spectra of N1s Pt/CCC.

respectively, which is deconvoluted to three pairs of doublets corresponding to Pt⁰, Pt²⁺, and Pt⁴⁺. The metallic Pt⁰ for Pt/CCC is observed at 71.2 eV (Pt 4f_{7/2}) and 74.7 eV (Pt 4f_{5/2}). The second doublet at 72.1 and 75.8 eV could be assigned to the Pt²⁺ chemical state as PtO or Pt(OH)₂ [73, 74]. The third doublet of Pt at 74.4 and 77.5 eV was the weakest in intensity, which are ascribed to Pt⁴⁺ chemical state as PtO₂ [74-76]. The deconvoluted Pt data of Pt/CB indicates that the Pt binding energy (BE) values are nearly similar to that of Pt/CCC. The percentage of Pt⁰ for Pt/CCC is higher than that for Pt/CB, (53% for HCC and 46.8% for Pt/CB). The N 1s spectra of Pt/CCC are shown in Figure 2.8 (c). Four different types of nitrogen namely, pyridinic, pyrrolic and/or pyridone, quaternary, and pyridinic-N⁺-O⁻ are assigned to the N 1s spectra as in the case of pure CCC (Figure 2.4 (b)). Relative ratios of pyridinic-N and pyrrolic-N and/or pyridine-N are 29.8 and 41.0% of total nitrogen, respectively. Quaternary-N accounts for 22.6 % while pyridinic-N⁺-O⁻ occupies the remaining 6.5%. As compared to the CCC, the pyridinic-N decreases by 11.9% and pyrrolic-N and/or pyridine-N increases by 13.5%. It may result from the oxidation of pyridinic-N during Pt deposition. Wang et al. studied the change of nitrogen types in accordance with electrochemical reduction and oxidation [77]. They found that the oxidation of nitrogen doped carbon monolith caused the decrease of pyridinic-N and increase of pyridone -N. The possible mechanism is that the electrons from nitrogen are consumed by Pt species, followed by formation of metallic Pt⁰. As shown in Pt oxidation state, Pt/CCC contains higher Pt⁰ concentration than Pt/CB. The results for the deconvolution of the Pt 4f and N 1s spectra are summarized in Table 2.2 and 2.3, respectively.

Table 2.2 Characteristics of the Pt/CB and Pt/CCC catalysts obtained from XPS Pt4f peaks

	Catalyst	BE [eV]		Relative Intensities [%]
		4f _{7/2}	4f _{5/2}	
Pt ⁰	Pt/CB	71.2	74.7	46.8
	Pt/CCC	71.2	74.7	53.0
Pt ²⁺	Pt/CB	72.2	75.8	35.8
	Pt/CCC	72.1	75.8	33.3
Pt ⁴⁺	Pt/CB	74.4	77.5	17.4
	Pt/CCC	74.4	77.5	13.7

Table 2.3 Characteristics of Pt/CCC obtained from XPS N1s peak

	BE [eV]	FWHM	Relative intensity [%]
Pyridinic- N	398.5	1.663	29.8
Pyrrolic N and or pyridone-N	400.2	1.823	41.0
Quaternary-N	401.4	2.328	22.6
Pyridinic-N ⁺ -O ⁻	404.1	2.11	6.5

The electrochemical characteristics of Pt/CCC and Pt/CB in 0.1 M HClO₄ at room temperature using three-electrode electrochemical cell are shown in Figure 2.9. The CV was performed at a scan rate of 50 mV s⁻¹ by sweeping the potential between 0.005 V and 1.0 V in N₂-saturated electrolyte as shown in Figure 2.9 (a). The ECSA was calculated from the integrated charge in the hydrogen desorption peak using the following equation:

$$\text{ECSA} = \frac{Q_{\text{H}}}{0.21 \times L_{\text{Pt}}} \quad [2.6]$$

where, Q_{H} (mC cm⁻²) is the coulombic charge for hydrogen desorption, L_{Pt} (mg cm⁻²) represents the Pt loading on the glassy carbon electrode and 0.21 mC cm⁻² is the charge required to oxidize a ML of H₂ on the Pt site [78]. The calculated value of ECSA for Pt/CCC is 67.2 m² g⁻¹, while the Pt/CB shows 56.8 m² g⁻¹. LSV in Figure 2.9 (b) was measured at a scan rate of 5 mV s⁻¹ in O₂-saturated electrolyte by sweeping the potential between 0.2 and 1.1 V in the anodic direction. The rotation speed is 1600 rpm for LSV measurement. The LSV curves presented in this work were properly corrected using the background capacitance current that was measured in the N₂ atmosphere at a scan rate of 5 mV s⁻¹. Figure 2.9 (b) shows that the Pt/CCC exhibits better ORR performance than the Pt/CB. The diffusion-limited current density of Pt/CCC is 5.67 mA cm⁻², while that of Pt/CB is 4.9 mA cm⁻². The half-wave potential of the Pt/CCC is 0.852 V, while that of Pt/CB is 0.769 V. Tafel plot obtained from Figure 2.9 (b) is presented in Figure 2.9 (c) which shows that Pt/CCC exhibits 3.5-fold higher kinetic current than the Pt/CB catalyst. The Tafel slope of Pt/CCC (80mV dec⁻¹) is lower than that of Pt/CB (88mV dec⁻¹). The results obtained from half-cell studies indicate that the Pt/CCC catalyst outperforms the Pt/CB catalyst in kinetic, mixed kinetic-diffusion, and diffusion regions. The enhancement in the ORR activity can be attributed to the use of CCC as a support which

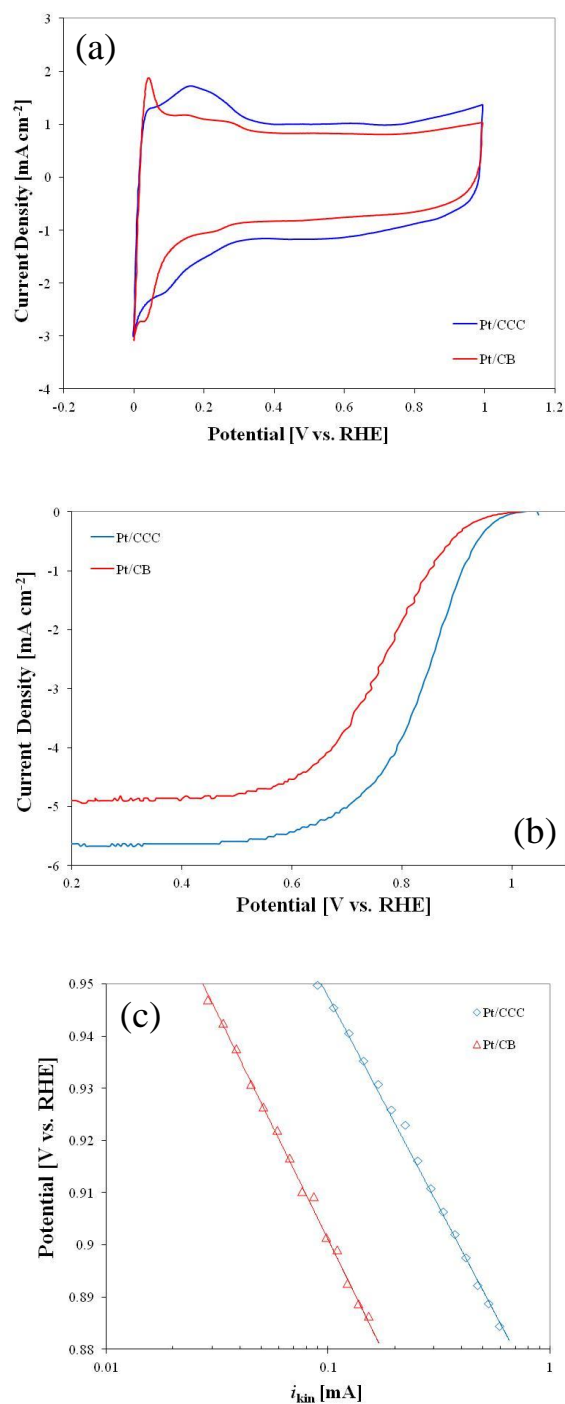


Figure 2.9 (a) CV diagrams of Pt/CCC and Pt/CB in N₂-saturated 0.1 M HClO₄ at room temperature and scan rate of 50 mV s⁻¹. (b) LSV curves of Pt/CCC and Pt/CB in O₂-saturated 0.1 M HClO₄ at room temperature and scan rate of 5 mV s⁻¹ at 1600 rpm. (c) Tafel plots from LSV data of Pt/CCC and Pt/CB at 1600 rpm.

significantly contributed to the overall activity through the synergistic effect. The origin of synergetic effect of Pt/CCC may come from the enhanced adsorption strength with the metals [79], improvement of electronic properties due to lone pairs of electrons on nitrogen atoms [80-82], and well-dispersed metal on support due to a strong Lewis basicity [56]. Additionally, the support used in this work is extremely active for ORR, which may reduce the oxygen in addition to the activity of Pt for the oxygen reduction. The increased Pt⁰ may also contribute to the high activity of Pt/CCC since the Pt⁰ is more active for ORR than Pt oxide. Electrochemical properties of the Pt/CB and Pt/CCC are summarized in Table 2.4.

2.3.3 EVALUATION OF FUEL CELL PERFORMANCE

In order to evaluate the fuel cell performances, Pt/CCC and Pt/CB are used as a cathode electrode in an MEA. The Pt loading at the anode is constant at 0.1 mg cm⁻² for all the MEAs tested. Two different Pt loadings (0.15 and 0.04 mg cm⁻²) are used for both Pt/CCC and Pt/CB catalysts. Figure 2.10 (a) represents PEMFC polarization curves obtained at 80 °C with reactants supplied at 100% RH and without backpressure. The fuel cell performance of Pt/CCC is significantly increased when compared to that of Pt/CB catalyst. The difference is prominent as the Pt loading decreases in the MEA. That is, at 0.04 mg cm⁻² Pt loading, Pt/CCC exhibits 1.5 to 6-fold increase in current density in the potential range of 0.6-0.8 V when compared with that of Pt/CB. The Pt/CCC exhibits 202 and 1252 mA cm⁻², while Pt/CB shows only 34 and 728 mA cm⁻² at 0.8 and 0.6 V, respectively. Figure 2.10 (b) exhibits the effect of backpressure when 0.04 mg cm⁻² Pt loading is used in the MEA. As the backpressure increases, the fuel cell performance

Table 2.4 Electrochemical properties of the Pt/CB and Pt/CCC catalysts obtained from CV diagrams and LSV curves

	Tafel slope [mV dec ⁻¹]	I_{kin} at 0.9 V vs. RHE [mA]	Half wave potential [V vs. RHE]	ECSA [m ² g ⁻¹]
Pt/CB	-80	0.11	0.769	56.8
Pt/CCC	-88	0.39	0.852	67.2

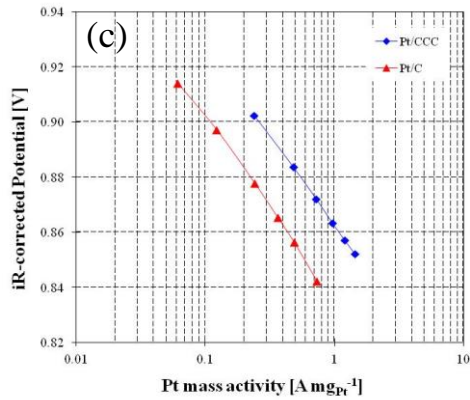
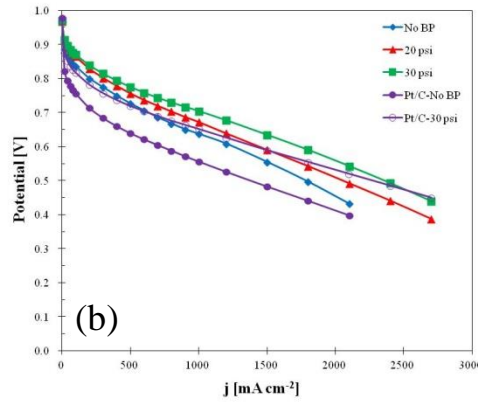
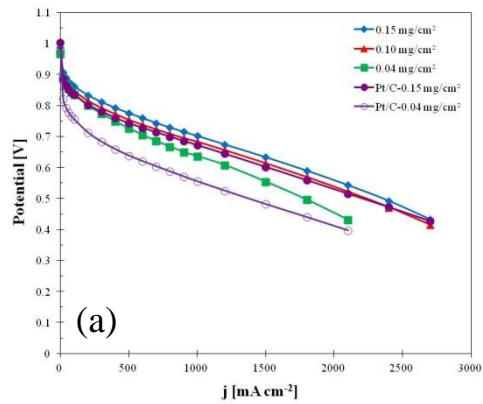


Figure 2.10 (a) PEMFC polarization curves of Pt/CCC and Pt/CB with various Pt loading at 80 °C and 100% RH and without backpressure. (b) PEMFC polarization curves of Pt/CCC and Pt/CB with various backpressures at 0.04 mg cm⁻² Pt loading at 80 °C and 100% RH. (c) Mass activities of Pt/CCC and Pt/CB at 80 °C and 100% RH applying a backpressure of 7.3 psi.

increased. As a result, Pt/CCC at 0.04 mg cm^{-2} with backpressure of 30 psi shows higher performance than Pt/CB at 0.15 mg cm^{-2} without backpressure. In the range of 0.6-0.8 V, the current density of Pt/CCC has increased 15-73% more than that of the Pt/CB. However, Pt/CCC and Pt/CB show similar performances at the mass transfer region. Similar results were observed in RDE tests shown in Figure 2.9 (b). The LSV curves showed a small difference in diffusion-limited current density region as compared to the difference in kinetic and mixed kinetic-diffusion regions. The mass activities shown in Figure 2.10 (c) were obtained by applying a backpressure of 7.3 psi and supplying H_2 and O_2 (70 and 160 sccm) to the anode and cathode, respectively. The mass activity of Pt/CCC is $0.26 \text{ A mg}_{\text{Pt}}^{-1}$, which is higher than that of Pt/CB ($0.1 \text{ A mg}_{\text{Pt}}^{-1}$). The results obtained from LSVs and fuel cell polarization curves indicate that the synergistic effect of CCC when used as a support for Pt catalyst is mainly effective in the kinetic and mixed kinetic-diffusion regions.

2.4 CONCLUSION

A novel non-precious metal CCC containing electrochemically active sites for ORR was prepared. The CCC exhibits high activity and good selectivity for ORR due to the presence of pyridinic and quaternary-nitrogen catalytic sites. The electrochemical performances of 5 wt% Pt deposited on CCC and CB were evaluated. Kinetic current of Pt/CCC calculated from LSV is 3.5-fold higher than that of Pt/CB. Tafel slope and half-wave potential of Pt/CCC exhibit higher activity than the Pt/CB. The enhanced activity may be attributed to the increased metallic Pt^0 concentration in Pt/CCC catalyst as confirmed by XPS analysis. XPS studies also confirmed the oxidation of nitrogen

resulting in an increase of metallic Pt⁰ during Pt synthesis. The Pt/CCC showed improved overall fuel cell performance. That is, in the potential range between 0.6 and 0.8 V, the current density of Pt/CCC is 1.5 to 6-fold higher than that of Pt/CB when employing ultra-low Pt loading (0.04 mg_{Pt} cm⁻²). Furthermore, by applying a backpressure of 30 psi, the Pt/CCC with 0.04 mg cm⁻² exhibited much higher fuel cell performance than Pt/CB with approximately four time higher Pt loading (0.15 mg cm⁻²) without applying backpressure. The HCC comprising of Pt and non-precious metal catalyst provides the enormous activity through the combined activity of catalytic sites present in the CCC support and Pt. Furthermore, the catalyst- support interaction of Pt and CCC enhanced the overall activity of Pt/CCC towards ORR. It is envisaged that the use of catalytically-active CCC as a cathode catalyst support may play a key role in achieving ultra-low Pt loading catalysts for automotive fuel cell application.

CHAPTER 3

DEVELOPMENT OF HIGHLY ACTIVE AND STABLE HYBRID CATHODE CATALYST UNDER POTENTIAL CYCLING CONDITIONS FOR PEMFCs

3.1 INTRODUCTION

PEMFCs are attractive power sources of the future for variety of applications including portable electronics, stationary power, and electric vehicles. However, sluggish cathode kinetics, high Pt cost, and durability issues inhibit the use of PEMFCs for automobile applications [83, 84]. A number of factors contribute to the performance degradation of PEMFCs including catalyst dissolution [12, 85-89], catalyst sintering [90, 91], membrane degradation [92-94], and carbon support corrosion [95-99].

One of the efforts in achieving increased catalytic activity is by alloying Pt with 3d transition metals to obtain high kinetic activity at 0.9 V_{iR-free} for ORR [100-104]. In PEMFCs, Pt-alloys with various transition metals such as Cr, Co, Ni, etc. have been extensively studied and shown superior electrocatalytic activity for the ORR when compared to pure Pt [102-106]. The enhancement in kinetic activity over Pt by alloying Pt with transition metals is due to various factors including lowering of the Pt oxidation state [107], suppression of Pt oxide formation [107, 108], formation of a new electronic structure with higher Pt 5d orbital vacancies [100], decrease in the Pt-Pt interatomic distance and therefore a more favorable O₂ adsorption [100], formation of a thin Pt skin

on the surface of the alloy core [109-111], and the altered electronic structures of the topmost Pt atoms [102, 103, 112].

Amongst the Pt-alloy catalysts, the PtCo catalyst has attracted much attention due to its high kinetic activity and stability in acidic environment [16, 105]. Paulus et al. studied the bulk compositions of 50 and 75 at.% Pt with Ni and Co as alloying elements [101]. In comparison to pure Pt, the results revealed a small activity enhancement of ca. 1.5 times for the 25 at. % Ni and Co catalysts, and a more significant enhancement by a factor of 2-3 for the 50 at.% Co. Huang et al. showed that PtCo alloy nanoparticles exhibit kinetic activity and specific activity enhancements by a factor of ~ 3.2 and ~ 2.2 , respectively for the ORR when compared to pure Pt [113]. Antolini et al. reviewed the activity and stability of various Pt-alloy catalysts, and concluded that PtCr and PtCo are more stable than PtV, PtNi, and PtFe due to their high degree of alloying and particle size [105]. Jayasayee et al. studied the activity and durability of PtCo, PtNi, and PtCu in PEMFC cathodes as a function of alloying elements in a systematic manner [104]. They showed that the performance of PtCo and PtCu catalysts was found to be most attractive when compared to PtNi and Pt catalysts. Mani et al. investigated the kinetic activity of dealloyed PtCu, PtCo, and PtNi in PEMFCs [106]. They found that Pt-alloy with Co and Cu are more active than PtNi. Mass and specific activities of PtCo and PtCu were enhanced by a factor of 3~4 times, compared to the commercial Pt/C catalyst.

The durability of carbon-supported PtCo catalysts is the core advantage as cathode catalysts in PEMFCs. Yu et al. studied the durability of Pt/C and PtCo/C cathode catalysts with continuous water fluxing on the cathode under a potential cycling test between 0.87 and 1.2 V vs. RHE [18]. The authors found that cobalt dissolution neither

detrimentally reduced the cell voltage nor dramatically affected the membrane conductance. Cell performance enhancement by PtCo/C over Pt/C catalyst was sustained over 2400 cycles and the overall performance loss of the PtCo/C membrane electrode assemblies (MEAs) was less than that of the Pt/C MEA. Arico et al. reported the performance and durability of carbon-supported PtCo under high temperature (110-130 °C) operation in PEMFCs [114]. A potential cycling test at 130 °C in a pressurized PEMFC showed a better stability for the PtCo alloy than pure Pt/C. Furthermore, better performance was obtained at high temperatures for the pre-leached PtCo/C than the Pt/C catalyst. They observed that the amount of Pt oxides on the outermost atomic layers was much smaller in PtCo than in Pt catalyst. These characteristics appeared to influence catalysts' performance and durability. Stassi et al. investigated the effect of thermal treatment on the structure and surface composition of PtCo catalysts during accelerated stress test (AST) [115]. They reported that different thermal treatments caused significant structural and morphological modifications in the PtCo catalysts. Yu et al. studied the cycling stability of dealloyed PtCo₃ and PtCu₃ catalysts between 0.6 and 1.0 V (vs. RHE) for up to 30,000 cycles [116]. In situ X-ray absorption spectroscopy (XAS) analysis showed stronger bulk Pt-Pt compressive strains and higher bulk d-band vacancies for the dealloyed PtCu₃ than the dealloyed PtCo₃ which was correlated to the higher initial activity of dealloyed PtCu₃. MEA tests showed poor durability towards voltage cycling for the dealloyed PtCu₃ catalyst when compared to dealloyed PtCo₃ catalyst due to Cu plating on the anode.

In general, PtM₃ (M = Cu, Co, Ni, Fe, Cr) catalysts are prepared by impregnating excess amount of transition metal salts into Pt/C catalyst followed by a heat-treatment

under a reducing atmosphere and acid leaching procedures [106, 116, 117]. Since excess transition metal salts are used for the catalyst synthesis, the leaching is carried out in strong acids for prolonged time which may be detrimental to the support stability when the cathode experiences high potentials during startup/shutdown cycles. In our previous studies, we reported a novel method of preparing Co-doped Pt catalysts on CCC supports [85, 118]. In the present study, Co was initially doped into the CB at high temperature using metal-catalyzed pyrolysis which was used as a transition metal source for the formation of Co-doped Pt. The Co-doped carbon prepared in this manner was used as a support to deposit Pt nanoparticles (Pt/CCC catalyst synthesis). The Pt supported on Co-doped carbon was heat-treated under reducing atmosphere to obtain Co-doped Pt catalyst with controlled particles size. During heat-treatment, Co, which is doped within the carbon, diffuses to the surface and forms Co-doped Pt catalyst with a core-shell structure. The kinetic activity and durability of kinetic activity of Co-doped Pt prepared by the novel approach were examined and compared with those of commercial PtCo/C as well as state-of-the-art Pt/C catalyst [119, 120].

3.2 Experimental

3.2.1 PREPARATION OF SUPPORT AND CATALYST

The CCC support was prepared using the procedure developed at the University of South Carolina [51-53, 61, 65]. In brief, as-received CB (Ketjen Black EC-300J) was oxidized with 9.8 M HNO₃ solution at 85 °C for 9 h under refluxing conditions. After filtering, the oxidized CB was washed with DI water several times and dried under vacuum at 80 °C for 12 h. A desired amount of Co(NO₃)₂ and ethylene diamine, used as

Co and N precursors, respectively, were mixed with the oxidized CB in 200 ml IPA. The mol ratio of Co and N precursors was maintained at 1:9. The mixture was refluxed for 3 h at 85 °C under vigorous stirring, followed by drying under vacuum at 80 °C. The resultant powder was subjected to heat-treatment under inert atmosphere at 800 °C for 1 h followed by leaching in 0.5 M H₂SO₄ at 80 °C for 3 h to remove excess Co. The final product is denoted as CCC. The CCC was non-covalently activated by the 1-pyrenecarboxylic acid (PCA) before the Pt deposition [121, 122].

Pt deposition was accomplished by a polyol reduction method for the preparation of 30% Pt/CCC catalyst. First, the CCC support was dispersed in 25 ml of ethyleneglycol in a sonication bath (Branson ultrasonic cleaner). A desired amount of PtCl₄ was added and the pH was adjusted to 11 by the addition of 0.1 M NaOH solution. The resulting solution was refluxed at 160 °C for 3 h and allowed to cool to room temperature. Then, the solution was filtered, washed with DI water, and dried at 160 °C for 1 h. Prior to heat-treatment, the Pt/CCC was subjected to a protective coating procedure using polyaniline. Oxidative polymerization of aniline sulfate was carried out at room temperature using ammonium peroxydisulfate as the oxidizing agent [123, 124]. The polyaniline-coated Pt/CCC was placed in an alumina crucible and heat-treated at 700 -900 °C for 2 h in a tubular furnace under 5% H₂ (balance N₂) atmosphere. The catalyst thus prepared is denoted as Co-doped Pt/CCC.

For comparison, the PtCo catalyst was prepared by the conventional impregnation method with the same ratio of Pt to Co as in the Co-doped Pt/CCC. Briefly, the 46 % Pt/C (TEC10E50E, Tanaka Kikinzoku Kogyo K.K, Japan) is mixed with Co(NO₃)₂ at an atomic ratio of 1:1. The mixture was stirred for 12 h to obtain

homogeneous slurry. The resultant slurry was dried in an oven for 12 h under vacuum followed by heat-treatment at 800 and 900 °C for 2 h under 5% H₂ (balance N₂) atmosphere. The catalysts thus obtained were denoted as PtCo/C-Imp-800 and PtCo/C-Imp-900, respectively.

3.2.2 PHYSICAL CHARACTERIZATION

The nitrogen adsorption/desorption isotherms were obtained at −196 °C using a Quantachrome NOVA 2000 BET analyzer. Specific surface area was determined by a multipoint BET analysis. PSD curves were calculated by the BJH method using the adsorption/desorption branch. XRD analysis was performed using a Rigaku D/Max 2500 V/ PC with a Cu K α radiation. A tube voltage of 30 kV and a current of 15 mA were used during the scan. To estimate the particle size of samples, we employed the following Scherrer equation [66]:

$$D = \frac{k\lambda}{10B \cos \theta} \quad [3.1]$$

where D is the crystallite size in nm, k is a coefficient (0.9), λ is the wavelength of X-ray (1.5404 Å), B is the line broadening at half the maximum intensity in radians, and θ is the angle at the position of the maximum peak known as Bragg angle. Raman spectroscopy was used to evaluate the degree of graphitization of the carbon supports using HORIBA "LABRAM 1B" (He-Ne 20mW laser, wave length 632.817 nm). Inductively coupled plasma atomic emission spectroscopy (ICP-AES, Perkin Elmer) analysis was used to determine the composition of the catalysts. HR-TEM was used to study the morphology and particles size distribution of the catalysts using Hitachi 9500 HR-TEM operated at

300 kV accelerating voltage. XRF (Fischer XDAL) was used to determine PtCo composition in the catalyst and Pt loading in the catalyst coated membrane.

3.2.3 RDE MEASUREMENTS

A glassy carbon disk electrode (0.247 cm^2) was acted as a working electrode. The Ag/AgCl electrode and platinum mesh were used as a reference and counter electrodes, respectively. All electrode potentials reported here were converted into the RHE. In a typical RDE experiment, 8 mg of CCC and CB was ultrasonicated in 1 ml of IPA. 15 μl of the ink (0.12 mg cm^{-2}) was deposited on the glassy carbon electrode. For the Pt/CCC and Pt/CB, the catalyst was mixed with absolute ethanol and DI water ultrasonically. The catalyst ink was deposited onto the glassy carbon electrode.

RDE tests were performed in 0.1 M HClO_4 solution as an electrolyte at room temperature using a Pine bi-potentiostat (Model AFCBP1). The CV was swept at a scan rate of 50 mV s^{-1} from 0.005 to 1.0 V in deaerated electrolyte under N_2 atmosphere. LSV measurements were conducted at a scan rate of 5 mV s^{-1} in O_2 -saturated electrolyte by sweeping potential between 0.2 and 1.1 V anodically. The LSV curves presented in this work are properly corrected using the background capacitance current that is measured in the N_2 atmosphere at a scan rate of 5 mV s^{-1} .

3.2.4 MEA FABRICATION AND ELECTROCHEMICAL MEASUREMENT

For the MEA fabrication, the in-house synthesized catalysts were employed as the cathode catalyst while commercial 46% Pt/C was used as a catalyst for the anode. Catalyst inks were prepared by ultrasonically mixing the respective catalysts (32 mg),

IPA (1.8 ml), Nafion[®] ionomer (5% solution, Alfa Aesar), and DI water (0.2 ml). The ionomer content was 30% and 20% in the anode and cathode inks, respectively. The catalyst inks were sprayed directly on the Nafion[®] 212 membrane covering an active area of 25 cm². The Pt loading on the anode and cathode electrodes is kept at 0.1 and 0.15 mg cm⁻², respectively. The catalyst coated membrane was then hot pressed at 140 °C using a pressure of 20 kg cm⁻² for 6 min. in between the gas diffusion layers (Sigracet GDL 10BC, SGL) and Teflon gaskets to prepare the MEA for the performance evaluation studies in fuel cell.

Initially, the MEA was activated under a supply of H₂ and O₂ at 80 °C to the anode and cathode compartments, respectively with a flow rate of 750 sccm and 100% RH. After MEA activation, the initial kinetic activity at 0.9 V_{iR-free} was evaluated under H₂/O₂ (2/9.5 stoic.) at 80 °C, 100% RH, and 150 kPa_{abs.} back pressure. The electrochemical surface area (ECSA) was estimated using CV experiments carried out between 0.05 and 0.6 V (vs. RHE) at 80 °C under fully humidified H₂ and N₂ supply to the anode and the cathode, respectively. The mass activity measurements were performed using the AST protocol suggested by U.S DRIVE Fuel Cell Tech Team [125]. During AST, 200 sccm H₂ and 75 sccm N₂ were supplied to the anode and cathode, respectively and the potential was swept between 0.6 and 1.0 V (vs. RHE) at 50 mV s⁻¹ in a triangle profile for up to 30,000 cycles. The fuel cell polarization was conducted using a fully automated fuel cell test station (Scribner Associates Inc., model 850e) at 80 °C. The mass activity and ECSA measurements were performed after 0, 1000, 5000, 10,000, 20,000, and 30,000 cycles. The cell potential loss at 800 mA cm⁻² was used as one of the criteria to evaluate the catalyst performance. For comparison purposes, MEAs with commercial

PtCo/C (TEC36EA52, 46.8% Pt and 6.7% Co, Tanaka Kikinzoku Kogyo K.K, Japan) and 46% Pt/C (TEC10E50E, Tanaka Kikinzoku Kogyo K.K, Japan) as cathode catalysts were also prepared and evaluated under the same experimental conditions.

3.3 RESULTS AND DISCUSSION

3.3.1 CCC SUPPORT SYNTHESIS

Figure 3.1 illustrates the schematic diagram of the approach used to synthesize CCC and Co-doped Pt/CCC. Surface modification on the carbon support introduces oxygen and nitrogen groups on the surface [51, 65]. The metal-catalyzed pyrolysis increases the carbon graphitization degree at high temperatures (800~900 °C), introduces 7-15% Co in the carbon matrix, and incorporates nonmetallic (nitrogen-containing) active sites on the carbon surface. Next, the chemical leaching removes excess Co, and Co particles encapsulated with thin carbon layer is remained in the support which is used to dope Pt for preparing Co-doped Pt/CCC catalyst. Modified polyol process was used for uniform platinum deposition [118]. In the subsequent annealing step, the Co encapsulated within the CCC support diffuses to the surface to form Co-doped Pt catalyst in the presence of polymer protective coating [118]. The heat-treatment process was optimized to control the particle size between 3-5 nm, resulting in compressive Pt-lattice catalyst having Pt-shell/doped metal core structure.

Figure 3.2 (a) and (b) show the nitrogen adsorption-desorption isotherms and BJH PSD curves of CCC and CB. The specific surface areas of CCC and CB are 398 and 826 $\text{m}^2 \text{g}^{-1}$, respectively. The CCC exhibits characteristic Type IV adsorption/desorption

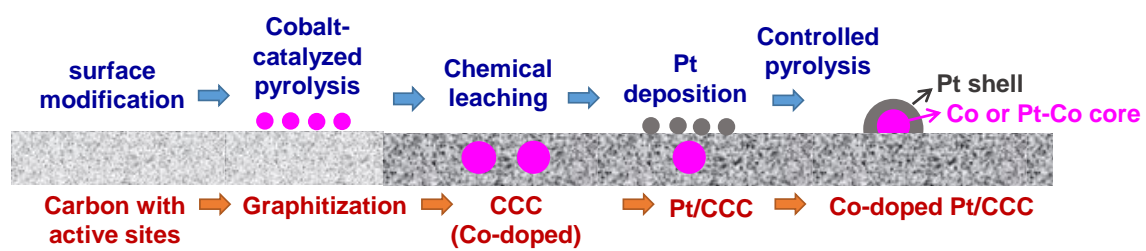


Figure 3.1 Schematic diagram for CCC support and Co-doped Pt/CCC catalyst synthesis.

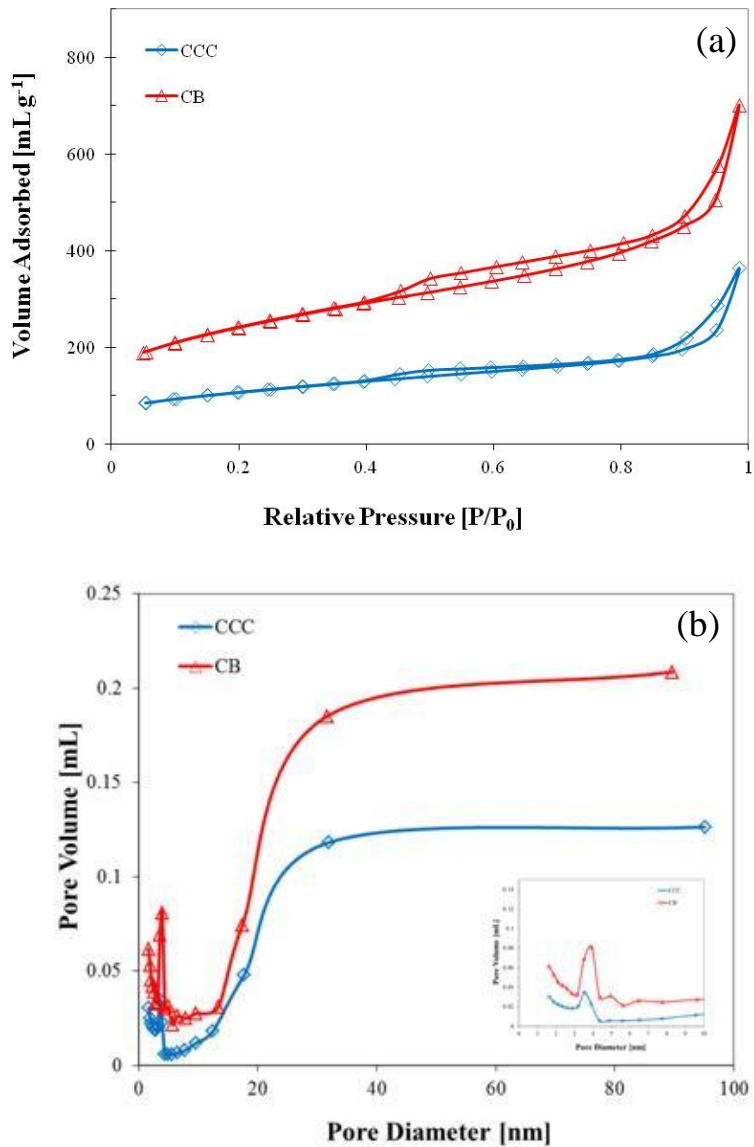


Figure 3.2 (a) N₂ adsorption/desorption isotherms and (b) BJH pore-size distribution curves obtained from the adsorption branch of CCC and CB. The inset in (b) compares the PSD in the range 0-10 nm.

isotherm behavior according to the IUPAC classification indicating its mesoporous nature [67]. The isotherms show hysteresis loop with sharp adsorption and desorption branches over a relative pressure range of 0.4-0.8. The nitrogen uptake is observed when (P/P_0) ratio is 0.94-1.0, which indicates the presence of mesopores [67]. The total pore volume was reduced from 0.846 to 0.688 ml g⁻¹. As shown in Figure 3.2 (b) inset, after the metal-catalyzed pyrolysis the peak pore diameter is ca. 4 nm.

Figure 3.3 (a) presents XRD patterns of the CCC and CB. Generally the characteristic diffraction peaks of (002) and (101) planes for carbon are found at ca. 26 and 43°. The diffraction peaks of CCC are sharper with increased intensity and shift to more positive angles. Consequently, the interlayer spacing of CCC based on (002) plane decreases to 0.3456 nm, while that of CB is 0.3615 nm. The results indicated that the carbon surface of CCC has been partially graphitized during metal-catalyzed pyrolysis. Furthermore, the CCC shows characteristic diffraction peaks at 44.2, 51.5, and 75.8° which correspond to the (111), (200), and (220) planes of FCC structure of Co metal particle (PDF#97-007-6632), respectively. The XRD results confirm the presence of Co metal after acid-leaching at 80 °C. Additionally, Figure 3.3 (b) reveals the Raman spectra for CCC and CB. Both CCC and CB show the D band and G band at approximately 1350 and 1580 cm⁻¹, respectively. The D band originates from structural defects and disorder-induced features on carbon, while the G band corresponds to the stretching vibration mode of graphite crystals [70, 126]. Relative ratio of D band to the G band (I_D/I_G) for CCC and CB is estimated to be 2.42 and 2.60, respectively, indicating that CCC is more graphitized than CB.

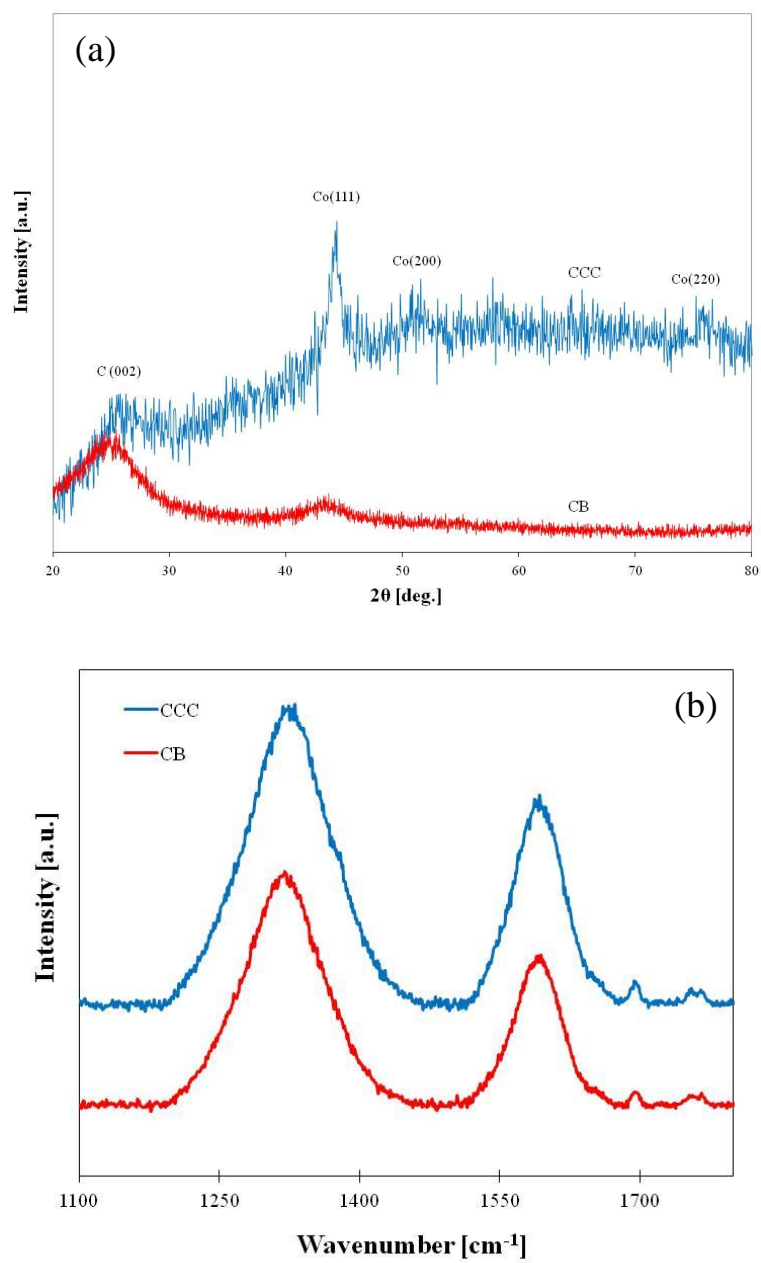


Figure 3.3 Comparison of (a) XRD patterns and (b) Raman spectra of CCC and CB.

The HR-TEM images of CCC (after acid leaching) and CB are shown in Figure 3.4 (a) and (b), respectively. The apparent difference between them is the presence of Co particles encapsulated by carbon shells in the CCC support since the Co particles present on the surface are removed during acid leaching. Nanostructured fibers or tubes of graphitic carbon are also formed as a result of pyrolysis in the presence of Co metal [55, 56] while CB showed amorphous morphology as shown in Figure 3.4 (b). ICP-AES analysis of CCC indicated a cobalt content of ~13 wt% in the CCC synthesized at 800 °C.

The results of XPS analysis performed on CCC and CB supports are presented in Figure 3.5 (a) and (b), respectively. Figure 3.5 (a) shows the survey scans for CCC and CB. Only XPS spectrum of CCC, as shown in Figure 3.5 (b), exhibits a broad peak around 398.9 eV which corresponds to the nitrogen atom. The nitrogen peak shown in Figure 3.5 (b) for CCC can be deconvoluted into four major peaks corresponding to pyridinic, pyrrolic and/or pyridone, quaternary, and pyridinic-N⁺-O⁻ (oxidized nitrogen). The peak at 398.4 eV accounts for the presence of pyridinic-N whereas the peak at 400.3 eV corresponds to the pyrrolic-N and/or pyridine-N. The peaks at 401.1 and 403.4 eV are ascribed to the presence of quaternary-N and pyridinic-N⁺-O⁻, respectively. Relative percentages of pyridinic-N and pyrrolic-N and/or pyridine-N are 41 and 38.5 % of total nitrogen, respectively. Quaternary-N accounts for 6.6 % while pyridinic-N⁺-O⁻ occupies 13.9 %. It is well-known that pyridinic-N situated on the edge of the graphite planes promotes ORR by donating one p-electron to the aromatic π system [55, 68]. Moreover, previous studies report that the quaternary-N plays a role as stable ORR active sites [55, 56, 61, 70]. Results for the deconvolution of the N 1s spectra are summarized in Table 3.1.

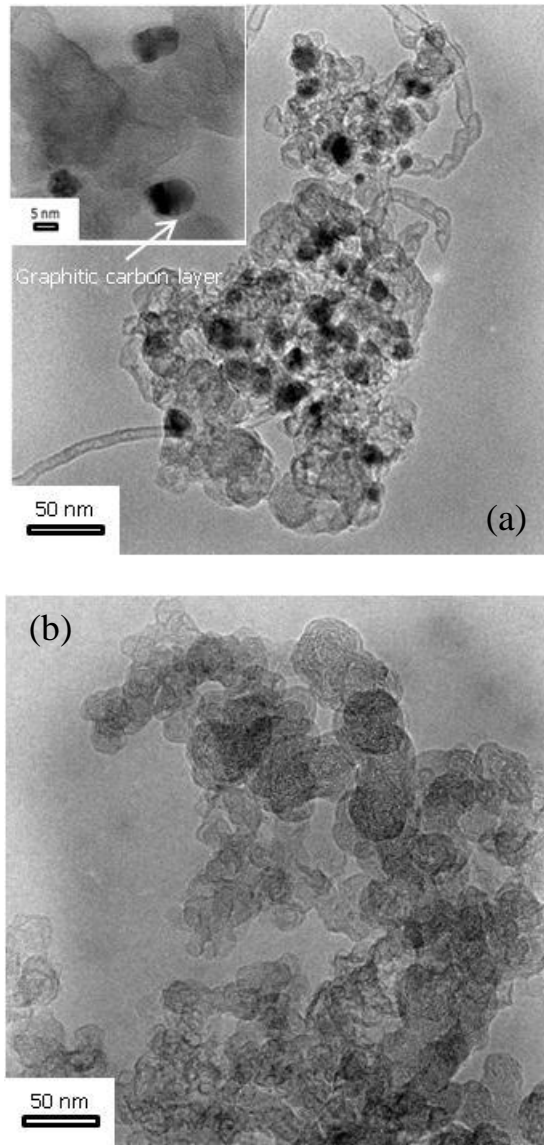


Figure 3.4 HR-TEM images of (a) CCC and (b) CB.

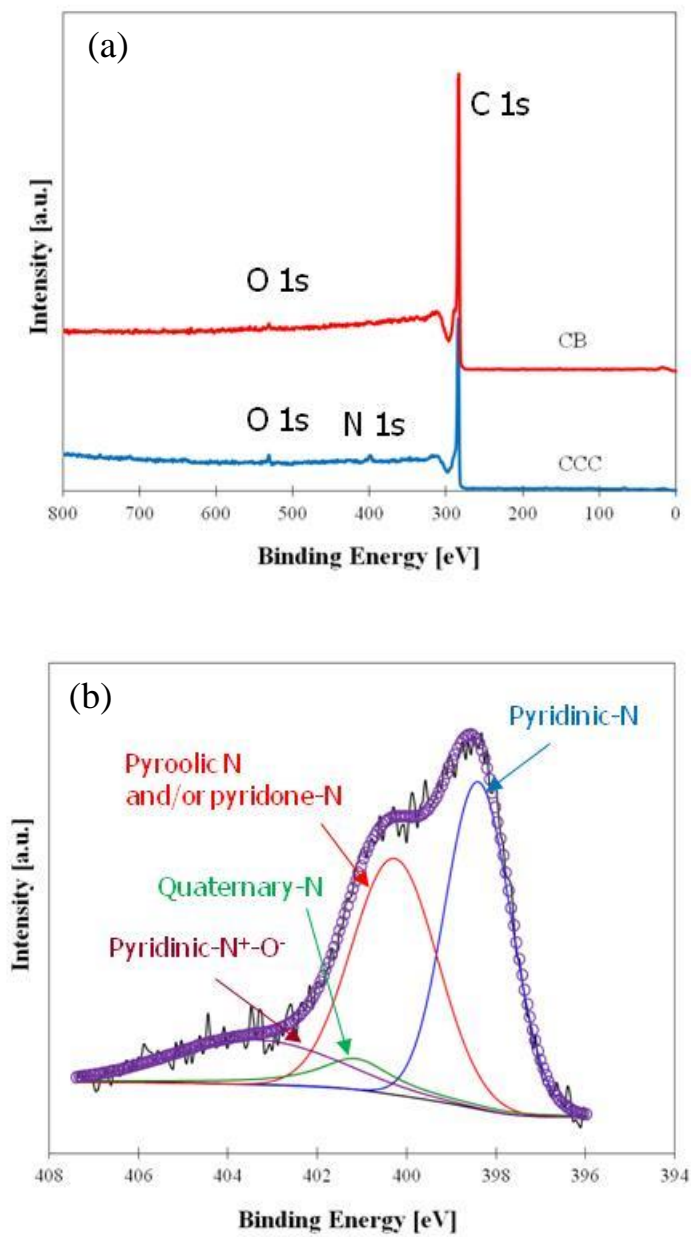


Figure 3.5 (a) XPS survey scans of CCC and CB and (b) deconvoluted N1s XPS spectra of CCC.

Table 3.1 Characteristics of CCC obtained from XPS N1s peak

	BE [eV]	FWHM	Relative intensity [%]
Pyridinic- N	398.4	1.736	41.0
Pyrrolic N and or pyridone-N	400.3	2.254	38.5
Quaternary-N	401.1	2.000	6.6
Pyridinic-N ⁺ -O ⁻	403.4	4.331	13.9

3.3.2 ELECTROCHEMICAL CHARACTERIZATION OF CCC

Figure 3.6 exhibits the electrochemical properties of CCC in a half-cell employing 0.1 M HClO₄ as the electrolyte. Figure 3.6 (a) represents the CV curves of CCC and CB at room temperature. CCC shows the quinone/hydroquinone redox coupling peaks at ca. 0.6 V; as the potential increases, the oxidation current of CB also increases while that of CCC remains almost constant. The low oxidation current may be attributed to the increase in the degree of graphitization for CCC support as confirmed by XRD and Raman spectroscopy analyses. In Figure 3.6 (b), LSV curves of CCC and CB recorded at a rotating rate of 1600 rpm and a scan rate of 5 mV s⁻¹ in O₂-saturated electrolyte are shown. The potential was swept between 0.2 and 1.1 V anodically. All the LSV curves were properly corrected using the background capacitance current obtained from the respective CVs recorded in N₂-saturated electrolyte. The on-set potential of CCC is 0.45 V higher than the CB. The plateau of diffusion-limited current density is well-developed at approximately 0.5 V indicating that the active sites for ORR were uniformly distributed on the CCC support. The LSV results show that the CCC support itself is active for the ORR which is advantageous when compared to the conventionally used CB.

3.3.3 SYNTHESIS OF CO-DOPED Pt/CCC CATALYST

The elemental compositions in the bulk of Pt/CCC and Co-doped Pt/CCC catalysts were determined using ICP-AES and XRF. Initially, the metal-catalyzed pyrolysis resulted in 13.2 wt% Co within the partially graphitized CCC support synthesized at 800 °C. As described earlier, the novelty of the process is to use the Co particles embedded in the CCC support for the formation of Co-doped Pt catalyst when

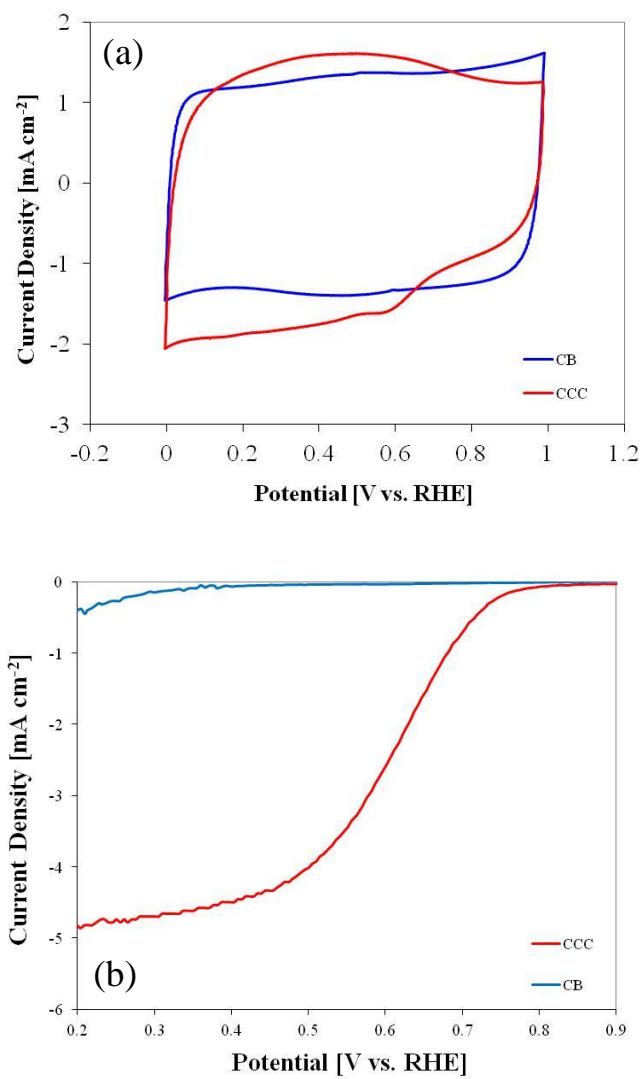


Figure 3.6 (a) CV diagrams of CCC and CB in N_2 -saturated 0.1 M HClO_4 at room temperature and scan rate of 50 mV s^{-1} . (b) LSV curves of CCC and CB in O_2 -saturated 0.1 M HClO_4 at room temperature and scan rate of 5 mV s^{-1} at 1600 rpm.

subjected to heat-treatment at 800 °C for 2 h under 5% H₂. ICP-AES and XRF analyses indicated initial Pt:Co atomic ratios of 1:1 and 1.1:1, respectively for Pt/CCC and Co-doped Pt/CCC catalysts.

In Figure 3.7, XRD is carried out to confirm that the Co is doped into Pt as a function of temperature. The catalyst is heat-treated for 2 h at the desired temperature under 5% H₂ atmosphere. The last 3 digits in the sample names represent the temperature, for example, the Co-doped Pt/CCC-700 is prepared at 700 °C. Deconvolution is carried out for the peaks obtained in 2 θ angles in the range 37-44°. The characteristic diffraction peaks of fresh Pt/CCC at 39.8, 46.25, 67.7, and 81.25° correspond to the (111), (200), (220) and (311) planes of FCC-Pt, respectively, while those at 44.2, 51.5, and 75.8° are ascribed to (111), (200), and (220) planes of pure Co, respectively, as shown in Figure 3.7 (a). The Co-doped Pt/CCC-700 and Co-doped Pt/CCC-750 represent split peaks, while the Co-doped Pt/CCC-800 and Co-doped Pt/CCC-900 show one single peak. Deconvoluted peaks for Co-doped Pt/CCC-700 and Co-doped Pt/CCC-750 are shown in Figure 3.7 (b) and (c), respectively. For Co-doped Pt/CCC-700, the peaks are located at 40.2 and 41.62°, while those are positioned at 40.65 and 41.45° when heat-treatment was carried out at 750 °C. A single peak was observed at 41.25 and 41.27° for Co-doped Pt/CCC-800 and Co-doped Pt/CCC-900, respectively. As a function of temperature, the Co metal is slowly diffused into the Pt particles and homogeneous Co-doped Pt is formed at 800 and 900 °C. As a result of Co diffusion into Pt particles, the peaks of Pt in Pt/CCC have shifted to higher angles and resulted in reduced lattice parameter. It indicates that the Co particles immobilized in the CCC support diffused to the surface at high temperature, which resulted in the formation of Co-doped Pt catalyst particles. Synthesis

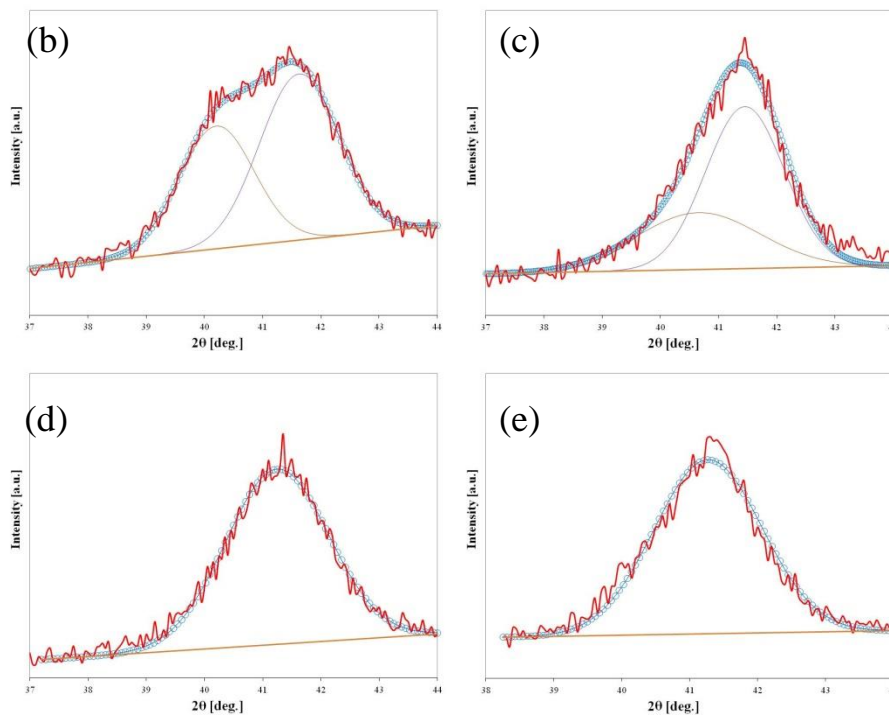
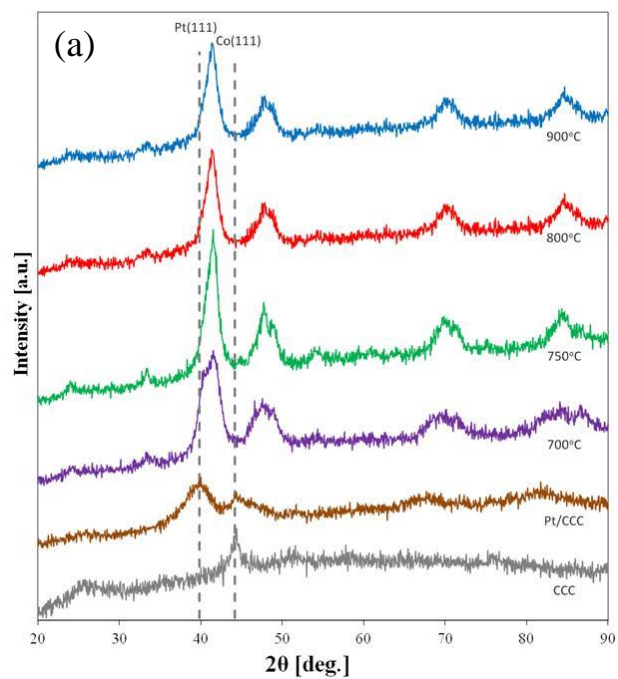


Figure 3.7 (a) XRD patterns of CCC, Pt/CCC, and Co-doped Pt/CCC prepared at 700, 750, 800, and 900 °C. Deconvoluted peaks of (b) Co-doped Pt/CCC-700, (c) Co-doped Pt/CCC-750, (d) Co-doped Pt/CCC-800 and (e) Co-doped Pt/CCC-900.

conditions, structural characteristics and composition for the Co-doped Pt/CCC are summarized in Table 3.2. On the other hand, the catalyst prepared by the conventional impregnation method exhibits one single peak for the sample heat treated at 900 °C, while multiple peaks are observed at 800 °C, as shown in Figure 3.8 (a). PtCo/C-Imp-800, as shown in Figure 3.8 (b), shows the 3 peaks at 40, 41, 41.48°. When the temperature is raised to 900 °C, only a single peak is observed at 41.18° (Figure 3.8 (c)). These results show that, in order to obtain a homogeneous structure of catalyst successfully, the conventional impregnation method must be carried out at 100 °C higher temperature than the novel method developed in the current study. Both Co-doped Pt/CCC-800 and PtCo/C-Imp-900 show chemically ordered face centered tetragonal (FCT) structure. The (001) and (100) superlattice planes at ca. 24 and 33°, respectively, confirm the FCC to FCT phase transformation [127]. Co-doped Pt/CCC-800 and PtCo/C-Imp-900 are used as cathode catalysts to study their electrochemical performance and the results are presented in section 3.3.4 (Figure 3.11).

The HR-TEM images of Pt/CCC, Co-doped Pt/CCC-700, Co-doped Pt/CCC-750, Co-doped Pt/CCC-800, and Co-doped Pt/CCC-900 are shown in Figure 3.9 (a)-(e), respectively. The average particle sizes and the particle size distribution were measured using the values obtained from over 100 nanoparticles. As shown in Figure 3.9 (a), the Pt nanoparticles are deposited with uniform size and distribution on the CCC support. The mean particle size is approximately 2.5, 4.9, 5.0, 5.4 and 6.2 nm for the Pt/CCC, Co-doped Pt/CCC-700, Co-doped Pt/CCC-750, Co-doped Pt/CCC-800, and Co-doped Pt/CCC-900, respectively. For the Pt/CCC catalyst, the Pt nanoparticles are uniformly deposited on the support and 2-3 nm-sized particles are dominant. Most of the particles in

Table 3.2 Summary of synthesis conditions, structural characteristics, and composition of Co-doped Pt/CCC

Synthesis temperature [°C]	Composition (at. Pt:Co =)	Catalyst phase	Lattice parameters a/c [Å/ Å]	Particle size [nm]	Relative FCT ratio [%]
700	1.1:1	disordered FCC	3.882/3.882	2.5	58.8
		ordered FCT	2.688/3.667		
750	1.1:1	disordered FCC	3.841/3.841	4.4	64.3
		ordered FCT	2.688/3.709		
800	1.1:1	ordered FCT	2.688/3.759	3.9	100
900	1.1:1	ordered FCT	2.688/3.754	4.6	100

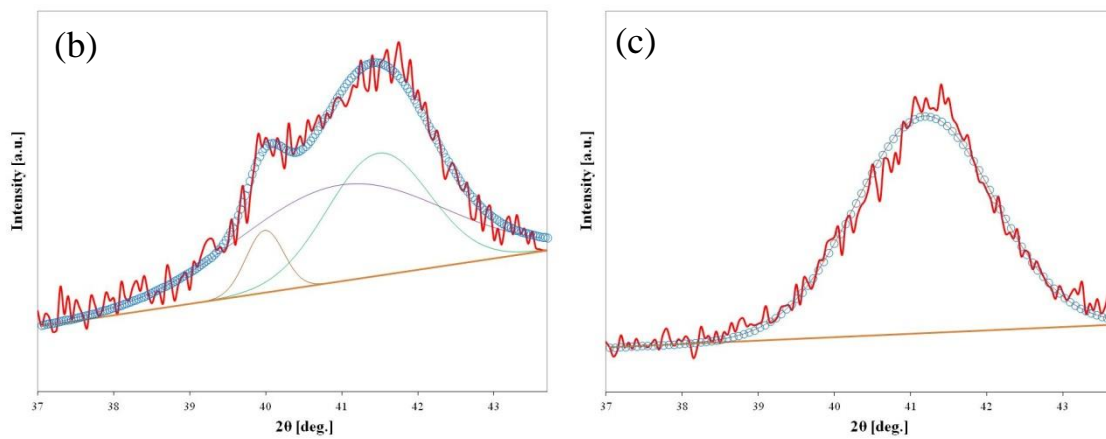
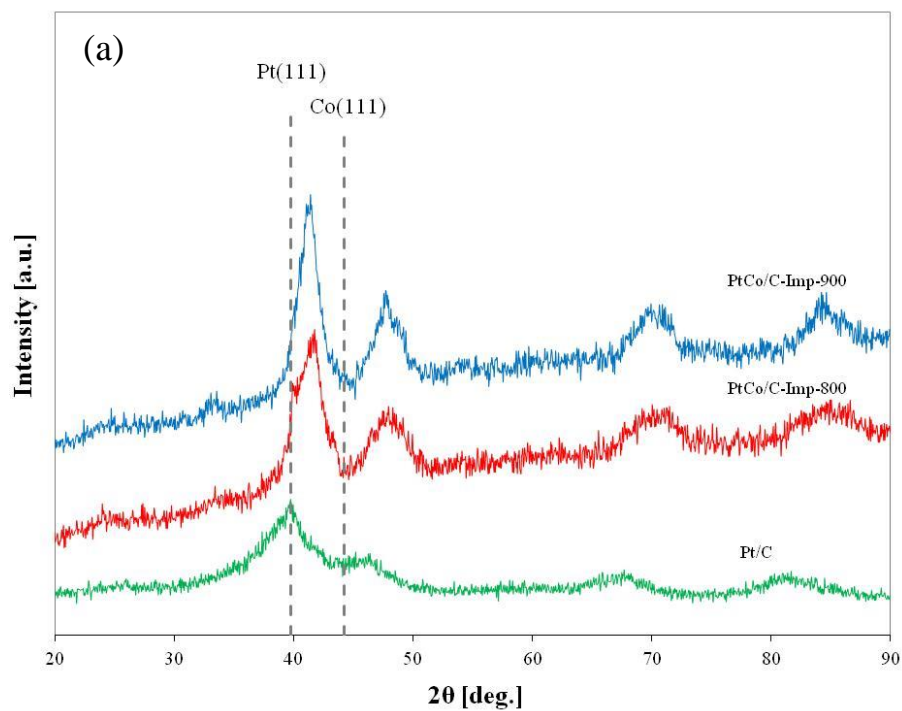


Figure 3.8 (a) XRD patterns of Pt/C, PtCo/C-Imp-800, and PtCo/C-Imp-900 prepared at 800, and 900 °C. Deconvoluted XRD patterns of (b) PtCo/C-Imp-800, and (c) PtCo/C-Imp-900.

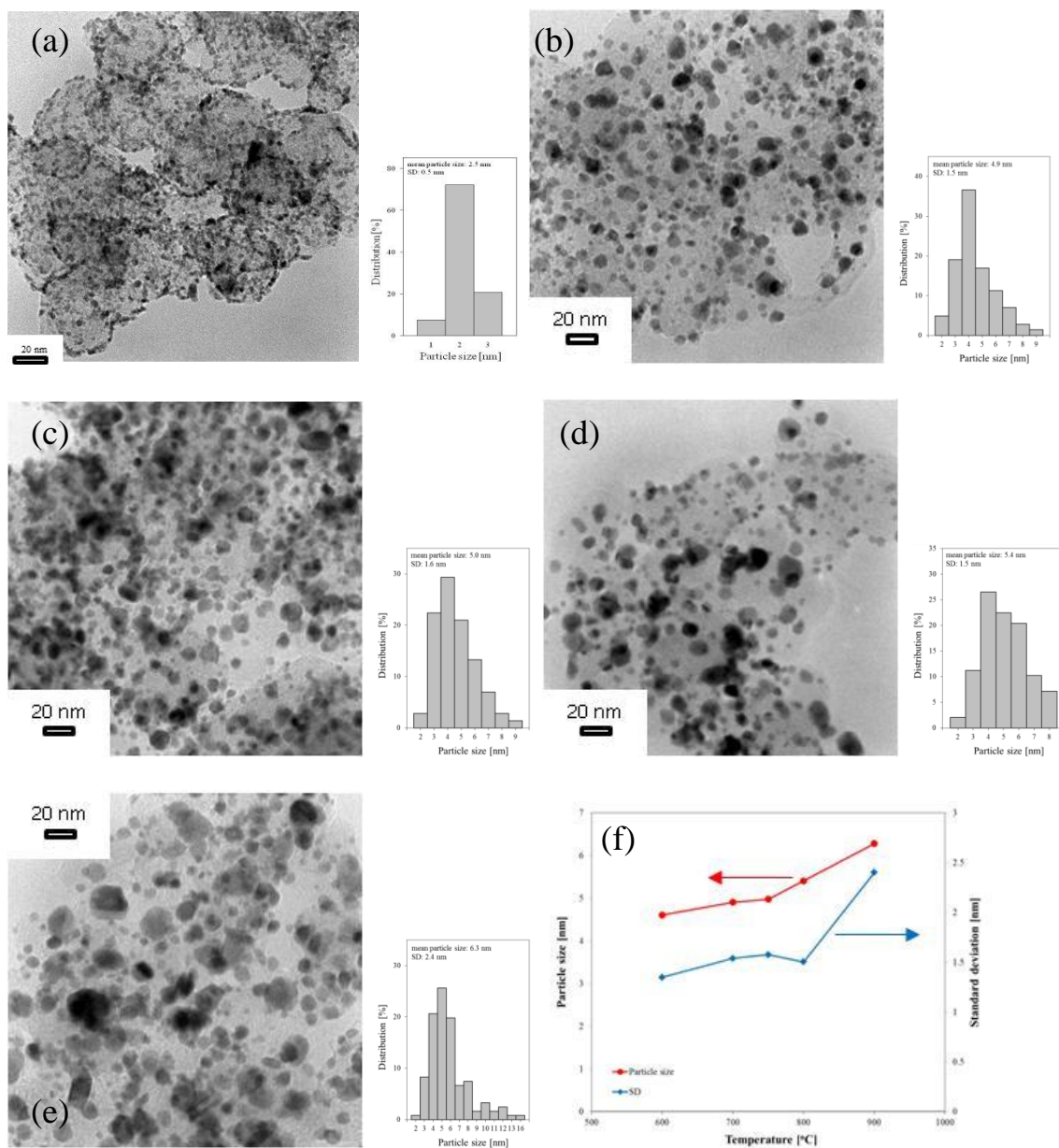


Figure 3.9 HR-TEM images of (a) Pt/CCC , (b) Co-doped Pt/CCC-700, (c) Co-doped Pt/CCC-750, (d) Co-doped Pt/CCC-800 and (e)Co-doped Pt/CCC-900

Co-doped Pt/CCC catalyst are in the range of 4-7 nm while a few large particles are also formed due to the high temperature treatment, but they are well-distributed on the support. In Figure 3.9 (f), the particle size and standard deviation (SD) are plotted. The particle size and SD increase gradually for the samples prepared at temperatures in the range of 600 to 800 °C, while significant increase is observed for the sample heat treated at 900 °C. Especially, 900 °C resulted in poor particle size distribution when compared to other catalysts.

3.3.4 DURABILITY OF CO-DOPED Pt/CCC IN PEMFC TESTING.

Figure 3.10 represents the catalyst durability of Co-doped Pt/CCC-700, Co-doped Pt/CCC-750, and Co-doped Pt/CCC-800 samples subjected to 0.6-1.0 V potential sweeping at a scan rate of 50 mV s⁻¹. The AST was performed for 30,000 cycles at 80 °C and 100% RH and the potential loss at 800 mA cm⁻² in H₂/air polarization was used for comparing the fuel cell performances of various catalysts. For the Co-doped Pt/CCC-700, the potential loss at 800 mA cm⁻² was 69 mV, while that of Co-doped Pt/CCC-750 is 48 mV. The Co-doped Pt/CCC-800 with a single diffraction peak as shown in XRD (Figure 3.7 (d)) shows a performance decay of 40 mV. The current density at 0.6 V_{iR-free} reduced by 39 and 31% for the Co-doped Pt/CCC-700 and Co-doped Pt/CCC-750, respectively. The Co-doped Pt/CCC-800 shows the most stable current density with 20% loss. The results obtained from AST reveal that the durability of Co-doped Pt/CCC increases as the synthesis temperature increases which may be attributed to the formation of chemically ordered FCT-structural catalyst at high annealing temperatures [127, 128].

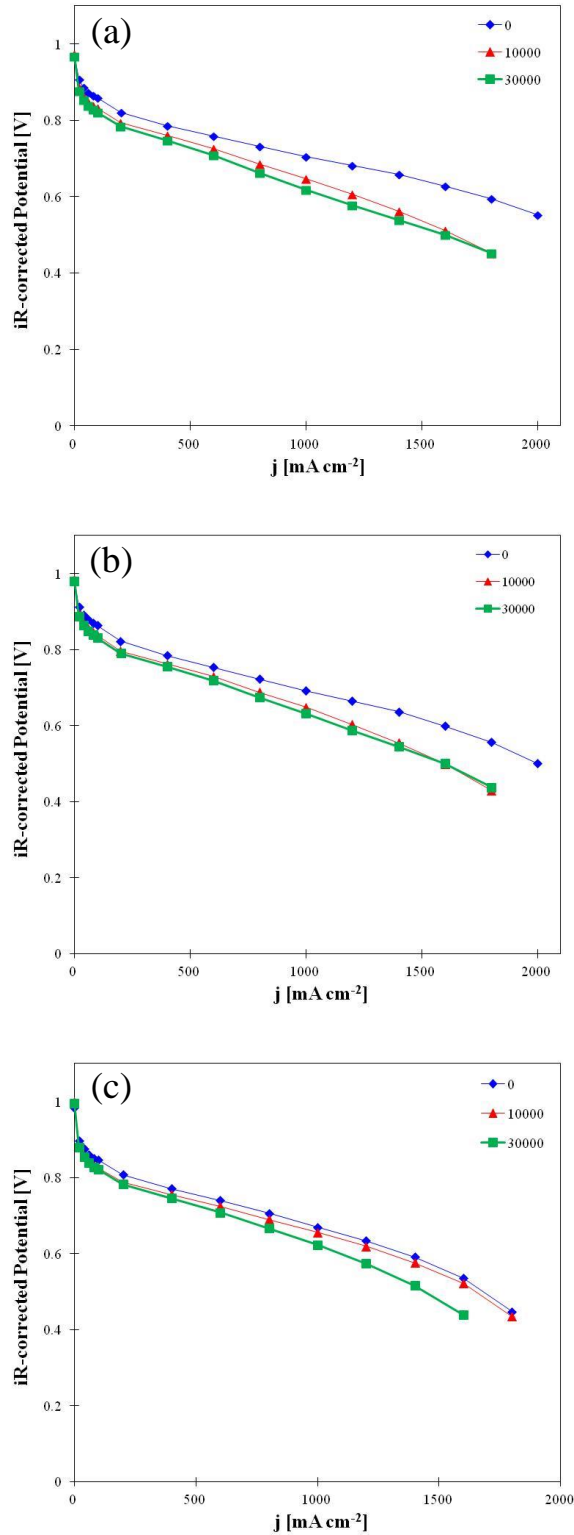


Figure 3.10 H_2/air polarization curves of (a) Co-doped Pt/CCC-700, (b) Co-doped Pt/CCC-750, and (c) Co-doped Pt/CCC-800 (initial and after 10,000 and 30,000 cycles).

Figure 3.11 shows the durability of Co-doped Pt/CCC, PtCo/C-Imp, PtCo/C, and Pt/C before and after 30,000 potential cycles between 0.6 and 1.0 V. The Co-doped Pt/CCC initially shows 1358 mA cm^{-2} at $0.6 \text{ V}_{\text{iR-free}}$, while that of PtCo/C-Imp exhibits 992 mA cm^{-2} . High Co concentration leads to a low fuel cell performance at high current density [129, 130]. However, despite the same ratio of Pt to Co, H_2/air polarization performance of Co-doped Pt/CCC is higher than that of PtCo/C-Imp and is similar to that of commercial Pt/C. After 30,000 cycles the current density of Co-doped Pt/CCC at $0.6 \text{ V}_{\text{iR-free}}$ decreases by 20%, while that of PtCo/C-Imp is 17.3%. The performance of Pt/C exhibits high performance (1467 mA cm^{-2}) at $0.6 \text{ V}_{\text{iR-free}}$ but its performance after 30,000 cycles significantly decreased by 76.2%. Commercial PtCo/C shows 51.8% loss from the initial current density of 930 mA cm^{-2} . After the AST, the potential loss of Co-doped Pt/CCC at 800 mA cm^{-2} is $40 \text{ mV}_{\text{iR-free}}$ while PtCo/C and Pt/C showed no activity at that current density after 30,000 cycles and the potentials are not measurable. The PtCo/C-Imp showed 60 mV loss after 30,000 cycles. The drastic performance degradation for the commercial PtCo/C and Pt/C catalysts can be attributed to Ostwald ripening, Pt dissolution and re-deposition [12, 85, 86, 89, 131].

The initial mass activities and stability of mass activities of Co-doped Pt/CCC, PtCo/C-Imp, PtCo/C, and Pt/C catalysts at $0.9 \text{ V}_{\text{iR-free}}$ are shown in Figure 3.12 (a)-(d), respectively. The mass activity is defined as the ORR rate per gram of Pt measured at $0.9 \text{ V}_{\text{iR-free}}$ [125]. The mass activity measurements were performed using the AST protocol suggested by U.S DRIVE Fuel Cell Tech Team. The Co-doped Pt/CCC shows much higher mass activity ($0.44 \text{ A mg}_{\text{Pt}}^{-1}$) at $0.9 \text{ V}_{\text{iR-free}}$ than commercial PtCo/C ($0.38 \text{ A mg}_{\text{Pt}}^{-1}$) and Pt/C ($0.18 \text{ A mg}_{\text{Pt}}^{-1}$) catalysts due to the formation of Co-doped Pt core and

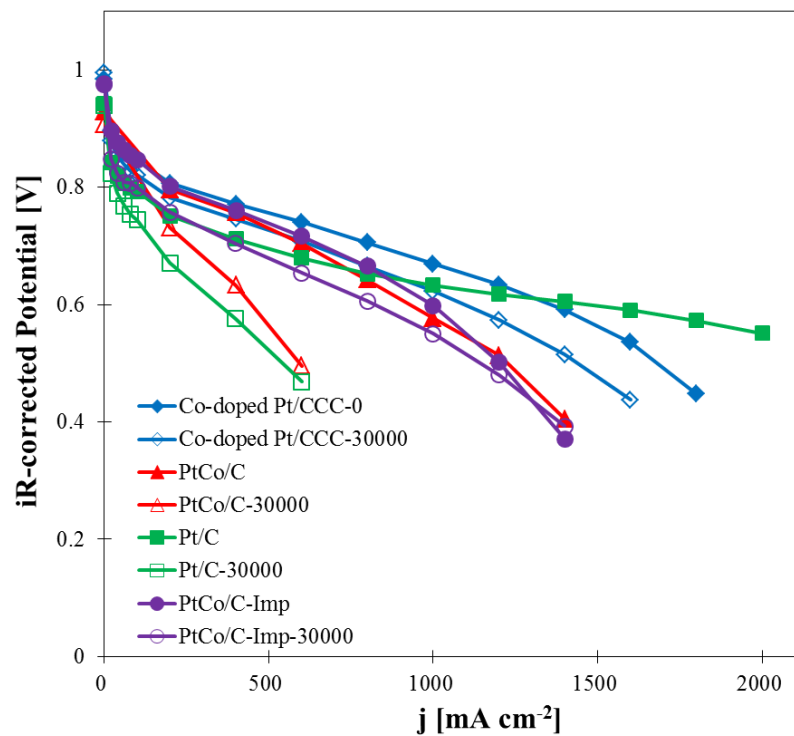


Figure 3.11 H_2/air polarization curves of Co-doped Pt/CCC, PtCo/C-Imp, PtCo/C, and Pt/C before and after 30,000 potential cycles between 0.6 and 1.0 V.

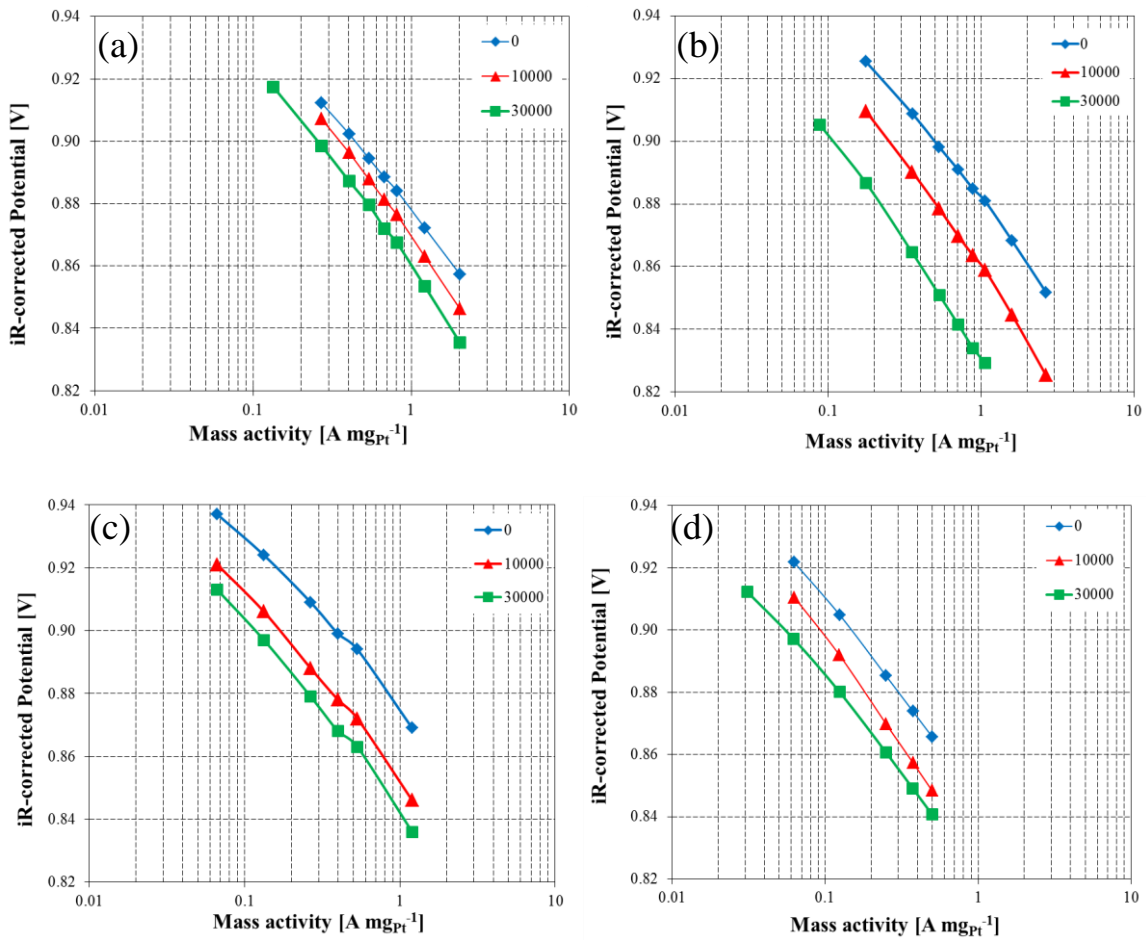


Figure 3.12 Comparison of mass activities of (a) Co-doped Pt/CCC, (b) PtCo/C-Imp, (c) PtCo/C, and (d) Pt/C catalysts as a function of cycle number. The activities were measured under the following operating conditions: H_2/O_2 (2/9.5 stoic.), 80 °C, 100% RH, and 150 kPa_{abs} . back pressure.

Pt-rich shell type catalyst particles with compressive Pt lattice during heat-treatment [103, 132, 133]. When transition metals such as Co are used to modify electronic properties of Pt, two major effects namely, strain effect and ligand effect, are induced within the Pt host lattice [134-137]. The ligand effect is the change in the local electronic, and therefore, the catalytic properties of a central metal atom brought about by varying its near neighbor atoms [138]. The strain effect leads to a decrease in the Pt-Pt interatomic distance when compared to pure Pt while the ligand effect results in the modification of the surface electronic structure due to hetero-metallic bonding interactions [135].

The mass activity degradation tendencies of Co-doped Pt/CCC, PtCo/C-Imp, PtCo/C, and Pt/C catalysts are plotted in Figure 3.13. It shows a linear decrease until 20,000 cycles and stabilized after 20,000 cycles. After 30,000 cycles, the decrease in mass activity is ca. 42.8%, 78.8%, 69.6%, and 63% for Co-doped Pt/CCC, PtCo/C-Imp, PtCo/C, and Pt/C, respectively. Furthermore, the Co-doped Pt/CCC still retained a significant amount of mass activity ($0.25 \text{ A mg}_{\text{Pt}}^{-1}$) even after 30,000 potential cycles which is much higher than that of initial mass activity of Pt/C ($0.18 \text{ A mg}_{\text{Pt}}^{-1}$). This may be due to the fact that the Co dissolution rate in Co-doped Pt/CCC is much smaller than that in commercial PtCo/C and Co doping has increased the durability of Co-doped Pt/CCC catalyst under potential cycling conditions. After potential cycling between 0.6 and 1.0 V, thick Pt skin ($\sim 1.8 \text{ nm}$) is formed on the catalyst due to Pt dissolution/re-deposition (Figure 3.14), which is still active for the ORR as indicated by the high mass activity even after 30,000 cycles. The thick Pt skin reduces the electronic effect in Co-doped Pt which may be one of the reasons for the kinetic activity loss besides the well-explained Pt particle agglomeration effect [139, 140]. On the other hand, Co from

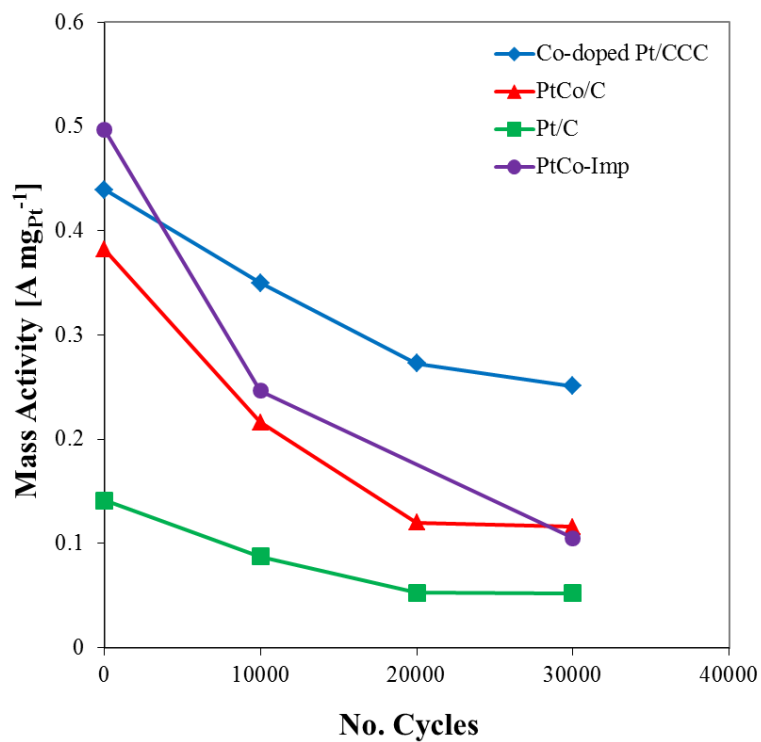


Figure 3.13 Mass activity degradation of Co-doped Pt/CCC, PtCo/C-Imp, PtCo/C, and Pt/C catalysts as a function of cycle number.

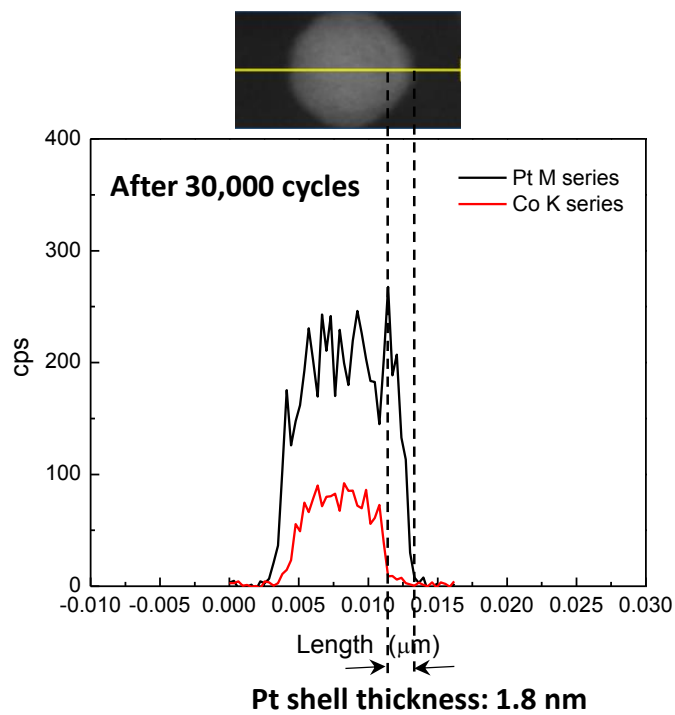


Figure 3.14 X-ray energy dispersive spectrometry (XEDS) particle line-scan of Co-doped Pt/CCC catalyst (after 30,000 cycles).

PtCo/C–Imp and PtCo/C catalyst is rapidly dissolved after 10,000 cycles and the mass activity reached a value which is close to that of initial value for the Pt/C catalyst. Thus, after 10,000 cycles, the commercial PtCo/C catalyst performs like a pure Pt/C catalyst and further performance degradation is caused by the Pt dissolution and redeposition mechanism which occurs at higher rate than the one observed for Co-doped Pt/CCC.

To further understand the loss in kinetic activity, the normalized ECSAs of Co-doped Pt/CCC, PtCo/C–Imp, PtCo/C, and Pt/C as a function of cycle number are shown in Figure 3.15. The integration of hydrogen desorption area in the CV can be obtained with subtraction of the current density due to double layer charging. The ECSA was calculated using the following equation:

$$\text{ECSA} = \frac{Q_{\text{H}}}{0.21 \times L_{\text{Pt}}} \quad [3.2]$$

where, Q_{H} (mC cm^{-2}) is the coulombic charge for hydrogen desorption, L_{Pt} (mg cm^{-2}) represents the Pt loading and 0.21 mC cm^{-2} is the charge required to oxidize a ML of H_2 on the Pt site [78]. Initial ECSA values of 75, 41, 68, and $75 \text{ m}^2 \text{ g}_{\text{Pt}}^{-1}$ were obtained for Co-doped Pt/CCC, PtCo/C–Imp, PtCo/C, and Pt/C catalysts, respectively. Generally ECSAs of all the catalysts decrease rapidly by 10,000 cycles, while those are linearly reduced from 10,000 to 30,000 cycles. The Pt/C shows rapid degradation in the first 1,000 cycles comparing to stable Co-doped Pt/CCC and PtCo/C–Imp. After 1,000 cycles, Co-doped Pt/CCC and PtCo/C–Imp show ca. 5% decrease of initial ECSAs, while the ECSA of Pt/C decreases ca. 17%. Finally, after 30,000 cycles, 64% of the initial ECSA is remained for the Co-doped Pt/CCC, while 53, 21, and 22% of initial ECSAs are retained for PtCo/C–Imp, PtCo/C, and Pt/C, respectively. This result indicates that the Co-doped Pt/CCC is remarkably more stable than PtCo/C–Imp, PtCo/C, and Pt/C catalysts.

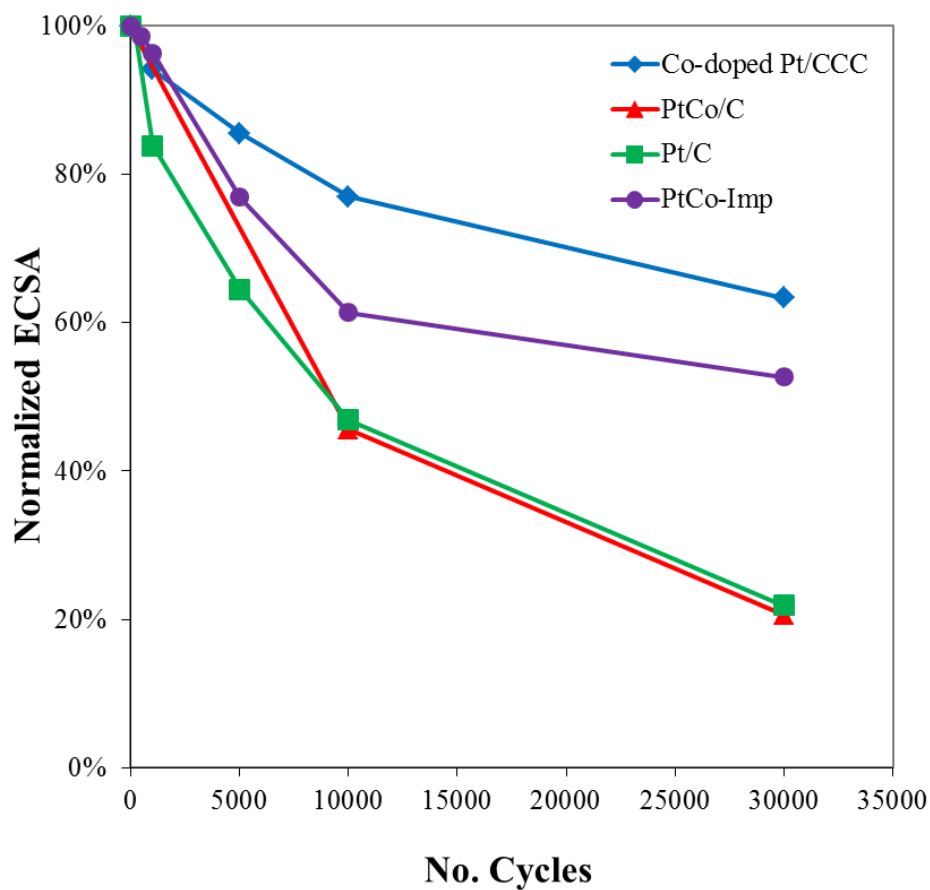


Figure 3.15 Normalized ECSA of Co-doped Pt/CCC, PtCo/C –Imp, PtCo/C, and commercial Pt/C catalysts as a function of cycle number. ECSAs were calculated from cyclic voltammograms obtained between 0.05 and 0.6 V (vs. RHE) at 80 °C. Fully humidified H₂ (200 sccm) and N₂ (75 sccm) were supplied to the anode and the cathode, respectively.

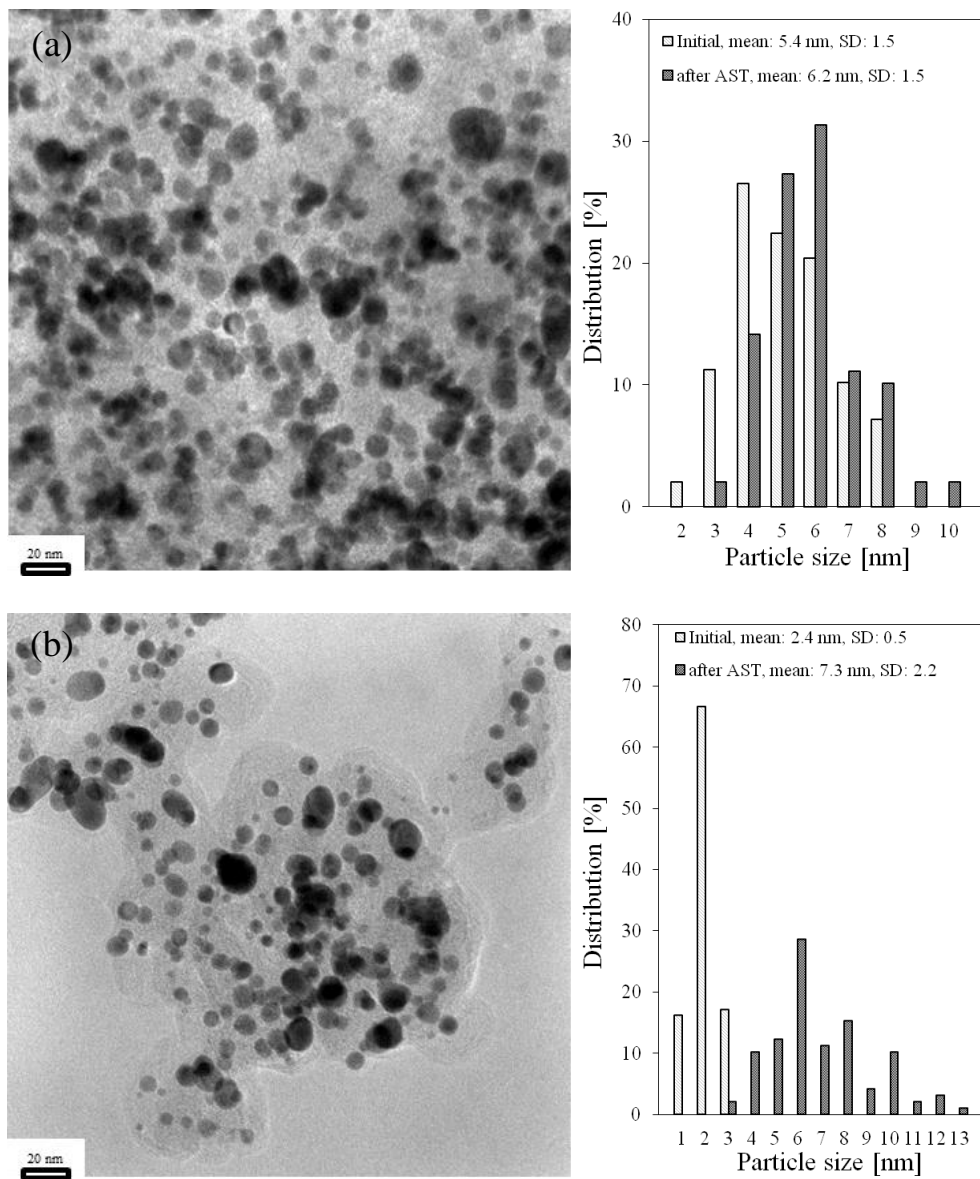


Figure 3.16 HR-TEM images and particle size distribution for (a) Co-doped Pt/CCC and (b) Pt/C catalysts before and after 30,000 cycles.

The HR-TEM images of Co-doped Pt/CCC and Pt/C after AST are shown in Figure 3.16 (a) and (b), respectively. After AST, the mean particle size of Co-doped Pt/CCC and Pt/C increased to 6.2 nm and 7.3 nm, corresponded to 15 and 204% increase, respectively. The Pt/C shows large particles (> 10 nm) and significant catalyst aggregation indicating poor particle distribution. Several mechanisms are suggested for the phenomenon such as Pt dissolution/redeposition, Pt migration and aggregation [141-144]. On the other hand, the particle size distribution based on the histograms represents that the particle size of Co-doped Pt/CCC still exhibits good catalyst dispersion and the narrow particle size distribution is well maintained. Since the ECSA and particle aggregation are related to the catalyst activity, the performance of Co-doped Pt/CCC is more stable than that of Pt/C catalyst.

Composition of Co-doped Pt/CCC catalyst before and after AST was examined using XRF as shown in Table 3.3. The results indicated that for the PtCo/C–Imp, the ratio of Pt:Co increased from 0.9:1 to 2.2:1 after AST, while the initial Pt:Co atomic ratio (1.1:1) for the Co-doped Pt/CCC increased to 2.3:1. The retained Co amount was 38.5% for PtCo/C–Imp, while that for the Co-doped Pt/CCC was 49.3% due to the dissolution of Co from the catalyst during potential cycling. A variety of studies have also reported that the PtCo catalyst degradation under fuel cell operating conditions is due to rapid Co dissolution, which results in the formation of a “Pt skeleton” structure at the outmost surface layer within the first few hours of operation [145-148]. Further degradation forms a thick Pt shell/PtCo core structure due to Co surface segregation/leaching and Ostwald ripening of Pt [145, 146]. It has been found that the Co content in the bulk PtCo

Table 3.3 Pt:Co atomic compositions of Pt/CCC and Co-doped Pt/CCC measured by ICP-AES, XPS, and XRF

	ICP	XPS	XRF	
			Initial	After AST
Pt/CCC	1:1	-	-	-
Co-doped Pt/CCC	1.1:1	1.2:1	1.1:1	2.3:1
PtCo/C-Imp	-	-	0.9:1	2.2:1

decreased and Co concentration of near-surface PtCo was lower than the bulk concentration after degradation [146, 149].

Structural change of Co-doped Pt/CCC and PtCo/C–Imp catalysts was studied by XRD investigation before and after AST as shown in Figure 3.17 and Table 3.4. As shown in Figure 3.17 (a), after the AST, the Co-doped Pt/CCC obviously shows Bragg angle shift to lower angles near to the peak position of pure Pt. The peak around 40° is deconvoluted into 2 peaks in Figure 3.17 (b). One peak is located at 39.87° and the other is positioned at 40.23° . The relative ratio is 12.1 and 87.9% for peaks at 39.87° and 40.23° , respectively. This result indicates that both thick Pt layer and Co-doped Pt co-exist in the cathode electrode due to the electrochemical leaching of Co and Pt dissolution/re-deposition phenomenon during potential cycling between 0.6 and 1.0 V. The Co on the catalyst surface is removed electrochemically during potential cycling between 0.6 and 1.0 V. Recently, some researchers have investigated the effect of structural and compositional changes on the degradation of PtCo catalyst stability [149-151]. Hidai et al., using Co 2p soft X-ray photoemission spectroscopy (SXPS) spectra of the cycle-tested PtCo catalyst, showed absence of cobalt on the surface of catalyst particles and the presence of thick Pt skin layer (> 1.4 nm) on the catalyst surface [149]. XRD patterns of the PtCo/C–Imp showed that the 2θ angle of metal planes moved to lower angle in Figure 3.17 (c). Deconvoluted peaks in Figure 3.17 (d) are observed at 40.03 and 39.90° . When compared to Co-doped Pt/CCC, the Bragg angle and relative ratio of PtCo characteristic peak are lower than those of Co-doped Pt/CCC. Interestingly, Pt characteristic peak is observed in both Co-doped Pt/CCC and PtCo/C–Imp. These results indicate that pure Pt

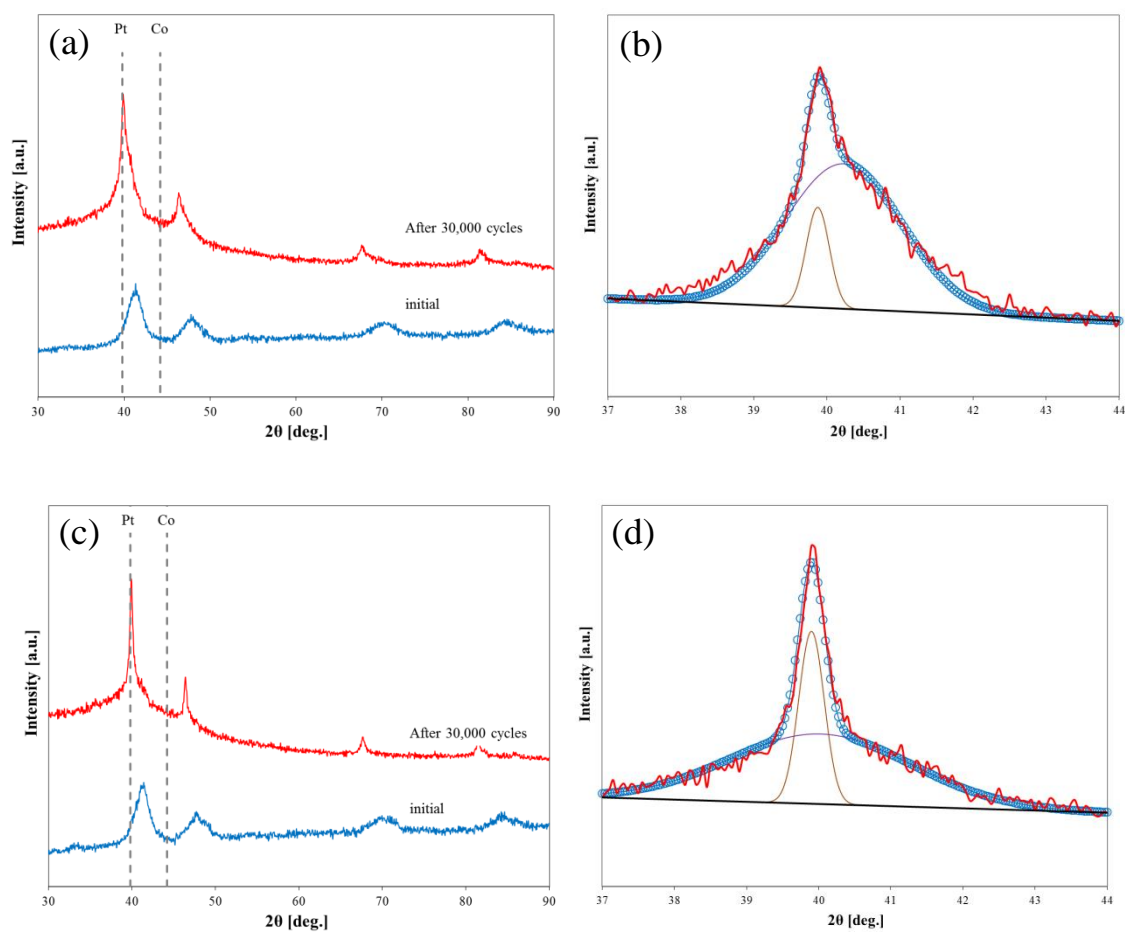


Figure 3.17 Comparison of XRD patterns of (a) Co-doped Pt/CCC and (c) PtCo/C-Imp before and after 30,000 cycles. Deconvoluted peaks of (b) Co-doped Pt/CCC and (d) PtCo/C-Imp after 30,000 cycles.

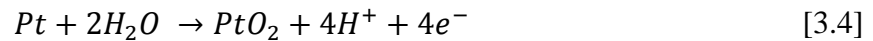
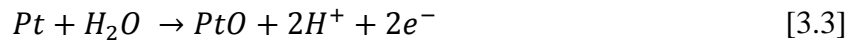
Table 3.4 Characteristics of XRD peak for Co-doped Pt/CCC and PtCo/C-Imp after 30,000 cycles

	Catalyst phase	Initial			After 30,000 cycles		
		2 θ	FWHM	Ratio [%]	2 θ	FWHM	Ratio [%]
Co-doped Pt/CCC	Pt	-	-	-	39.87	0.375	12.1
	PtCo	41.25	2.082	100	40.23	1.874	87.9
PtCo/C-Imp	Pt	-	-	-	39.90	0.416	25.9
	PtCo	41.18	2.155	100	40.03	2.955	74.1

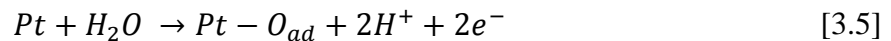
is deposited during dissolution/re-deposition when subjected to potential cycling, which corresponds to the results of compositional analysis shown in Table 3.3.

Table 3.5 compares the mass activities in H₂-O₂ at 0.9 V_{iR-free}, open circuit potentials (OCP) in H₂/air, and maximum power density in H₂/air fuel cell for Co-doped Pt/CCC, commercial PtCo/C, and commercial Pt/C catalysts. The OCP measurements indicated stable and very high values for the Co-doped Pt/CCC during the entire potential cycling period. Specifically, the OCP after 10,000 cycles is close to 1.0 V which may be attributed to the Co dissolution and formation of Pt-rich surface layer during potential cycling.

It has been reported that water activation and Pt-OH formation on PtCo catalyst surface is shifted to higher potentials when compared to pure Pt [101, 152, 153]. The cyclic voltammograms recorded in rotating ring disk electrode (RRDE) for Co-doped Pt/CCC and Pt/CCC catalysts shown in Figure 3.18 indicate a shift in Pt-OH formation by ~40 mV for the Co-doped Pt/CCC when compared to Pt/CCC. Figure 3.18 also shows two regions namely, H adsorption/desorption below 0.4 V and oxygen-related reactions (Pt oxidation/reduction) between 0.6 and 1.0 V. During potential cycling from 0.6 to 1.0 V, Pt oxides are formed according to the following reactions [11]:



At high potentials, adsorbed oxygen (Pt-O_{ad}) is formed due to water oxidation:



In the reverse scan from 1.0 to 0.6 V, platinum oxides are reduced to Pt according to the following reactions:

Table 3.5 Comparison of mass activities, OCPs in H₂/air, and maximum power density for Co-doped Pt/CCC, PtCo/C-Imp, PtCo/C, and Pt/C catalysts

Catalyst	Measured activity at 0.9 V _{iR-free} *			OCP (V)**		Maximum power density**		
	Initial (A mg _{Pt} ⁻¹)	After 30k cycles (A mg _{Pt} ⁻¹)	Loss (%)	Initial	30,000 cycles	Initial (mW cm ⁻²)	After 30k cycles (mW cm ⁻²)	Loss (%)
Co-doped Pt/CCC	0.44	0.25	43	0.984	0.995	857	721	16
PtCo/C-Imp	0.50	0.11	79	0.974	0.976	602	576	4
PtCo/C	0.38	0.116	69	0.922	0.907	482	251	48
Commercial Pt/C	0.18	0.06	67	0.960	0.917	746	274	63

* H₂/O₂ (2/9.5 stoic.), 80 °C, 100% RH, 150 kPa_{abs.} back pressure.

** H₂/air (2/2 stoic.), 80 °C, 50% RH, 170 kPa_{abs.} back pressure.

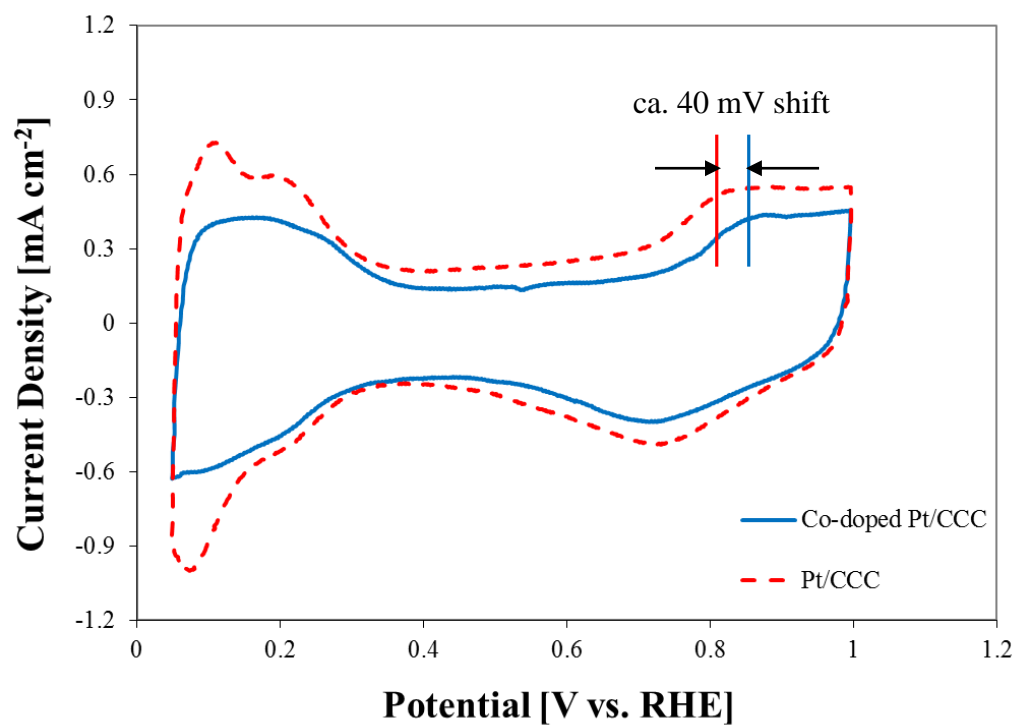
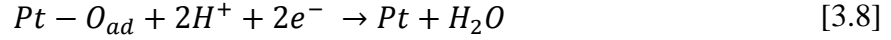
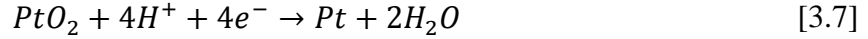
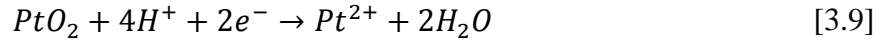


Figure 3.18 Cyclic voltammograms of Pt/CCC and Co-doped Pt/CCC. The measurements were carried out at room temperature by sweeping the potential from 0.05-1.0 V vs. RHE at 50 mV s^{-1} in nitrogen-purged 0.1 M HClO_4 .



The potential shift for Pt oxidation to higher values, as indicated by the higher OCP observed in H₂/air polarization curve, increases the kinetic mass activity (from 0.15 to > 0.4 A mg_{Pt}⁻¹) due to the suppression of Pt oxide formation which has much lower exchange current density for ORR ($i^0 = 1.7 \times 10^{-10}$ A cm⁻²) when compared to pure Pt ($i^0 = 2.8 \times 10^{-7}$ A cm⁻²) [154]. Besides the effect of higher kinetic activity, Co-doped Pt catalyst also illustrates improved stability when compared to pure Pt catalyst. Since Pt oxide dissolves during potential cycling conditions according to Eq. (8). Less PtO₂ formation in the forward scan due to higher Pt oxidation potential in the case of Co-doped Pt/CCC catalyst alleviates Pt dissolution in the reverse scan and enhances the catalyst stability.



However, in automotive applications at applied potentials of ~0.6-0.7 V, only pure Pt catalytic sites will be present on the catalyst surface for ORR at high current regions due to electrochemical reduction of Pt oxides formed when the cathode catalyst is subjected to high potentials during startup/shutdown cycles and/or fuel starvation. Thus, the H₂/air performance at low potentials will not be greatly affected as much as in the case of mass activity which is measured at 0.9 V_{iR-free}.

3.4 CONCLUSION

A novel procedure was developed for the synthesis of Co-doped Pt/CCC catalyst using Co-doped CCC as a support, which contains pyridinic-nitrogen active sites, through

platinum deposition and heat-treatment procedures. HR-TEM indicated uniform Pt deposition for the Pt/CCC and Co-doped Pt/CCC catalysts with average particle sizes of 2.5 and 5.4 nm, respectively. The Co-doped Pt/CCC catalyst showed initial mass activity of $0.44 \text{ A mg}_{\text{Pt}}^{-1}$ and $0.25 \text{ A mg}_{\text{Pt}}^{-1}$ at $0.9 \text{ V}_{\text{iR-free}}$ after 30,000 potential cycles between 0.6 and 1.0 V while the for the PtCo/C–Imp, PtCo/C, and Pt/C showed initial mass activity of 0.50, 0.38, and $0.14 \text{ A mg}_{\text{Pt}}^{-1}$ and ca. 60 ~ 70% loss of activity after 30,000 cycles. The enhanced catalytic activity at high potentials and stability of mass activity for the Co-doped Pt/CCC catalyst are attributed to the formation of compressive Pt lattice catalyst due to Co doping. The Co-doped Pt/CCC showed stable OCP close to 1.0 V under H_2/air with an initial power density of 857 mW cm^{-2} and only 16% loss after 30,000 cycles. Physical characterization such as XRD, XRF, and HR-TEM after 30,000 cycles showed that the Co-doped Pt/CCC exhibited more stable properties than other catalysts. Electrochemical characterization indicated that Co doping increased the potential for PtO_2 formation to a more positive value and suppressed the detrimental Pt dissolution/re-deposition process while enhancing the catalyst stability under potential cycling conditions.

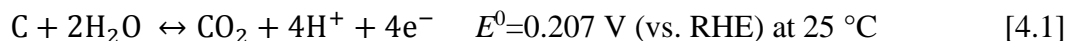
CHAPTER 4

EVALUATION OF CARBON NANOSTRUCTURE OBTAINED AT HIGH TEMPERATURE AND ITS DURABILITY UNDER PEMFC START-UP/SHUTDOWN CYCLING CONDITIONS

4.1 INTRODUCTION

PEMFCs are attracting huge attention as new power source for automotive and stationary applications, due to their intrinsic advantages such as low emission, high energy density, and high efficiency. However, there are still some problems to solve like the high activity and durability of catalysts in order to advance to the commercialization stage. In general, the carbon supported Pt or Pt-based alloy is used as catalysts.

Degradation mechanisms for catalysts involve dissolution of Pt [12, 85-89], migration of Pt [155, 156] and carbon corrosion [95-99]. Especially, since the standard electrode potential of carbon is very low as shown in the equation below, the carbon support is electrochemically oxidized under high temperature and humidity employed in normal operating conditions.



It is believed that there are two parallel pathways for carbon degradation [25, 35]. One is the direct carbon oxidation reaction in the presence of water and the other is the indirect carbon oxidation via surface oxides. In the presence of Pt, the Pt accelerates the

formation of CO-like species, which is further oxidized in the presence of water to produce CO₂ [27].

Reiser et.al proposed the reverse-current mechanism related to the local hydrogen starvation [31]. During transient conditions of the cell operation such as start-up and shut-down, a high interfacial potential difference causes carbon corrosion. When hydrogen is introduced into the anode during startup, a condition is created where hydrogen occupies only part of the anode. At this moment, the carbon corrosion is occurred at the cathode. During the shutdown procedure, a similar phenomenon can be occurred, when the air from the outside or through the membrane, replaces the hydrogen causing carbon corrosion at the anode [31-35]. Moreover, according to a reverse-current decay mechanism, after the shut down or during start-up, the cathode in PEMFC can experience a higher potential than the OCV. Such a high potential rapidly oxidizes the carbon support [31, 35]. When the carbon support is oxidized, the Pt nanoparticles aggregate to larger particles and the porosity of catalyst layer is changed [157, 158]. These results bring about the reduction of ECSA, and decreased performance.

Roen et al. detected CO₂ in the cathode exhaust gas during CV with varying Pt mass fraction, catalyst type, and temperature [27]. An Arrhenius plot indicated higher apparent activation energy for CO₂ production at the positive potential limit of the CV on 0% Pt (carbon-only) electrode than on 39% Pt/C electrode. It was concluded that platinum accelerated the corrosion rate of carbon support. DEMS shows that pure carbon is oxidized only at potentials higher than 0.9 V (RHE) and that Pt catalyzes the oxidation of a CO_{surf} surface layer to CO₂ at potentials between 0.6 and 0.8 mV (RHE) in the sulfuric acid solution. The result indicates that the carbon corrosion by Pt occurs in the

neighborhood of Pt-sites, thus damaging the Pt to carbon contact [36]. The MIMS shows the formation of carbon oxidation products like CO₂, CO and HCOOH. In-situ EQCM study shows mass changes of a variety of carbon supports during the CV in deaerated 0.5M H₂SO₄ solution [42]. High surface area CBs ECP 600 and ECP 300 have a carbon loss of 0.0245 ngcm⁻² s⁻¹ and 0.0144 ngcm⁻² s⁻¹ and as compared to 0.0115 ngcm⁻² s⁻¹ for low surface area support XC-72. Graphitized XC-72 and MWNTs, with higher graphitization have higher carbon corrosion onset potential at 1.65V and 1.62V, respectively and appear to be more intrinsically resistant to corrosion.

Hara et al. analyzed commercial Pt/CB, and Pt/GCB, heat treated Pt/GCB, and nanocapsule Pt/GCB) under start/stop operating condition [159]. They suggested that the Pt catalyst degradation was influenced not only by the type of carbon support but also by the state of Pt dispersion and the average Pt particle size. It is proposed that the electrodes with better performance contained a relatively large proportion of graphitic carbon, and the nature of these catalysts gave rise to better electronic conductivity and, thus, better resistance to oxidation and corrosion, as well as lower chemical activity, compared to CB.

In the present study, we are suggesting that the carbon nanostructure supports obtained by heat-treating amorphous CB improves the corrosion resistance. We have synthesized a number of carbon nanostructures at various temperatures, deposited Pt nanoparticles using modified polyol method, and evaluated the durability of the synthesized catalysts using an electrochemical potential cycle protocol between 1.0 and 1.5 V. The activity has been evaluated by the kinetic current and half-wave potential in RDE studies, while the durability has been estimated by ECSA, potential loss, and current density loss in 25 cm² MEAs.

4.2 EXPERIMENTAL

4.2.1 PREPARATION OF SUPPORT AND CATALYST

For the treatment of carbon supports, the as-received Ketjen Black EC-300J (KB) was heat-treated at different temperatures in order to obtain carbon supports having different degree of graphitization. Before the heat-treatment, nitrogen gas was flown to purge the quartz tube furnace (OTF-1200X-SNT-110, MTI corp.) for 30 min. The nitrogen gas was fed to the tubular furnace during the heat-treatment. The temperatures of 900, 1300, and 1700 °C are used in this study. Supports thus prepared are denoted as KB-9, KB-13, and KB-17, while the un-heat-treated sample is denoted as KB. The supports were non-covalently activated by the PCA before the Pt deposition due to their high hydrophobicity deposition [121, 122].

Pt deposition was accomplished by a polyol reduction method for the preparation of 30% Pt/C catalyst. First, each support was dispersed in 25 ml of ethyleneglycol in a round bottom flask using an ultrasonication bath (Branson ultrasonic cleaner). A desired amount of PtCl₄ was added and the pH was adjusted to 11 by the addition of 0.5 M NaOH solution. The resulting solution was refluxed at 160 °C for 3 h and allowed to cool to room temperature. Then, the solution was filtered, washed with DI water, and dried at 160 °C for 30 min under air atmosphere.

4.2.2 PHYSICAL CHARACTERIZATION

The nitrogen adsorption/desorption isotherms were obtained at -196 °C using a Quantachrome NOVA 2000 BET analyzer. Specific surface area was determined by a multipoint BET analysis. PSD curves were calculated by the BJH method using the

adsorption/desorption branch. XRD analysis was performed using a Rigaku D/Max 2500 V/ PC with a Cu K α radiation. A tube voltage of 30 kV and a current of 15 mA were used during the scanning. To estimate the Pt particle size of the synthesized catalysts, we employed the following Scherrer equation [66]:

$$D = \frac{k\lambda}{10B \cos \theta} \quad [4.2]$$

where D is the crystallite size in nm, k is a coefficient (0.9), λ is the wavelength of X-ray (1.5404 Å), B is the line broadening at half the maximum intensity in radians, and θ is the angle at the position of the maximum peak known as Bragg angle. Raman spectroscopy was used to evaluate the degree of graphitization of the carbon supports using HORIBA "LABRAM 1B" (He-Ne 20mW laser, wave length 632.817 nm). HR-TEM was used to study the morphology and particles size distribution of the catalysts using Hitachi 9500 HR-TEM operated at 300 kV accelerating voltage. XRF (Fischer XDAL) was used to determine PtCo composition in the catalyst and Pt loading in the catalyst coated membrane.

4.2.3 ELECTROCHEMICAL CHARACTERIZATION

Electrochemical characterization was performed in a RDE setup using a Pine bi-potentiostat (Model AFCBP1). A glassy carbon disk electrode (0.247 cm²) was acted as a working electrode. The Ag/AgCl electrode and platinum mesh were used as a reference and counter electrodes. RDE tests were performed in 0.1 M HClO₄ solution as an electrolyte at room temperature. All the potentials are reported against RHE. In a typical experiment, Pt catalyst was mixed with IPA and DI water ultrasonically. The catalyst ink was deposited onto the glassy carbon electrode, leading to a catalyst loading of 20 μg_{Pt}

cm^{-2} . For all RDE tests, 5 μl of 0.25 wt% ionomer (Alfa Aesar) was additionally deposited on the catalyst layer to ensure good adhesion of the catalyst onto the glassy carbon electrode. LSV was measured at a scan rate of 5 mV s^{-1} by sweeping the potential between 0.2 V and 1.05 V under oxygen purging. The LSV curves presented in this work were properly corrected using the background capacitance current that was measured in the nitrogen atmosphere at a scan rate of 5 mV s^{-1} .

4.2.4 MEA FABRICATION AND PEMFC MEASUREMENT

The in-house synthesized Pt catalyst and commercial 46% Pt/C were employed as the cathode and anode catalysts, respectively. Catalyst inks were prepared by ultrasonically mixing the appropriate amount of catalysts, IPA, Nafion[®] ionomer (5% solution, Alfa Aesar), and DI water. The ionomer content was 30% and 20% in the anode and cathode inks, respectively. The catalyst inks were sprayed directly on Nafion[®] 212 membrane covering an active area of 25 cm^2 . The Pt loading on the anode and cathode electrodes is kept at 0.1 and 0.15 mg cm^{-2} , respectively. The catalyst coated membrane was then hot pressed at 140 $^{\circ}\text{C}$ using a pressure of 20 kg cm^{-2} for 6 min. in between the gas diffusion layers (Sigracet GDL 10BC, SGL) and Teflon gaskets to prepare the MEAs for the performance evaluation studies in fuel cell.

The initial mass activity at 0.9 $V_{\text{iR-free}}$ was evaluated under H_2/O_2 (2/9.5 stoic.) at 80 $^{\circ}\text{C}$, 100% RH, and 150 kPa_{abs} back pressure. For the polarization studies, H_2 and air were supplied to the anode and cathode, respectively at a constant stoichiometry of 2 and 2 (170 kPa_{abs} backpressure) at 80 $^{\circ}\text{C}$ and 40% RH. The ECSA was estimated using CV experiments carried out between 0.05 and 0.6 V (vs. RHE) at 80 $^{\circ}\text{C}$ under fully

humidified H₂ and N₂ supply to the anode and the cathode, respectively. For the AST, H₂ and N₂ were supplied to the anode and cathode at 100% RH, respectively and the potential was swept between 1.0 and 1.5 V (vs. RHE) at 500 mV s⁻¹ in a triangle profile for up to 3,000 cycles [125]. The fuel cell test was conducted using a fully automated fuel cell test station (Scribner Associates Inc., model 850e). The mass activity, ECSA, and H₂/air polarization measurements were performed every 1,000 cycles.

4.3 RESULTS AND DISCUSSION

4.3.1 CHARACTERIZATION OF SUPPORTS

Figure 4.1 (a) and (b) show the nitrogen adsorption-desorption isotherms and BJH PSD curves of KB, KB-9, KB-13, and KB-17. The specific surface area of KB is ca. 826 m² g⁻¹. The specific surface areas of KB-9, KB-13, and KB-17 are 760, 515, and 276 m² g⁻¹, respectively. The isotherms of all supports show hysteresis loop with sharp adsorption and desorption branches over a relative pressure range of 0.4–0.8, as shown in Figure 4.1 (a). Furthermore, nitrogen uptake for CCC and GCCC is observed at a relatively high pressure of 0.94 – 1.0, which is associated with the presence of mesopores. The isotherms of KB-9, KB-13, and KB-17 exhibit characteristic Type IV by IUPAC classification indicating that KB-9, KB-13, and KB-17 are the mesoporous support [67]. The total pore volume of KB, KB-9, KB-13, and KB-17 are 1083, 1097, 1042, and 921 ml mg⁻¹, respectively. In Figure 4.1 (b), as a function of temperature, the carbon supports heat-treated at higher temperature show larger volume than KB in the pore diameter range of 20 and 100 nm. In contrast, in the small pore diameter (< 3 nm), the carbons heat-treated at higher temperature represent the decrease of pore volume.

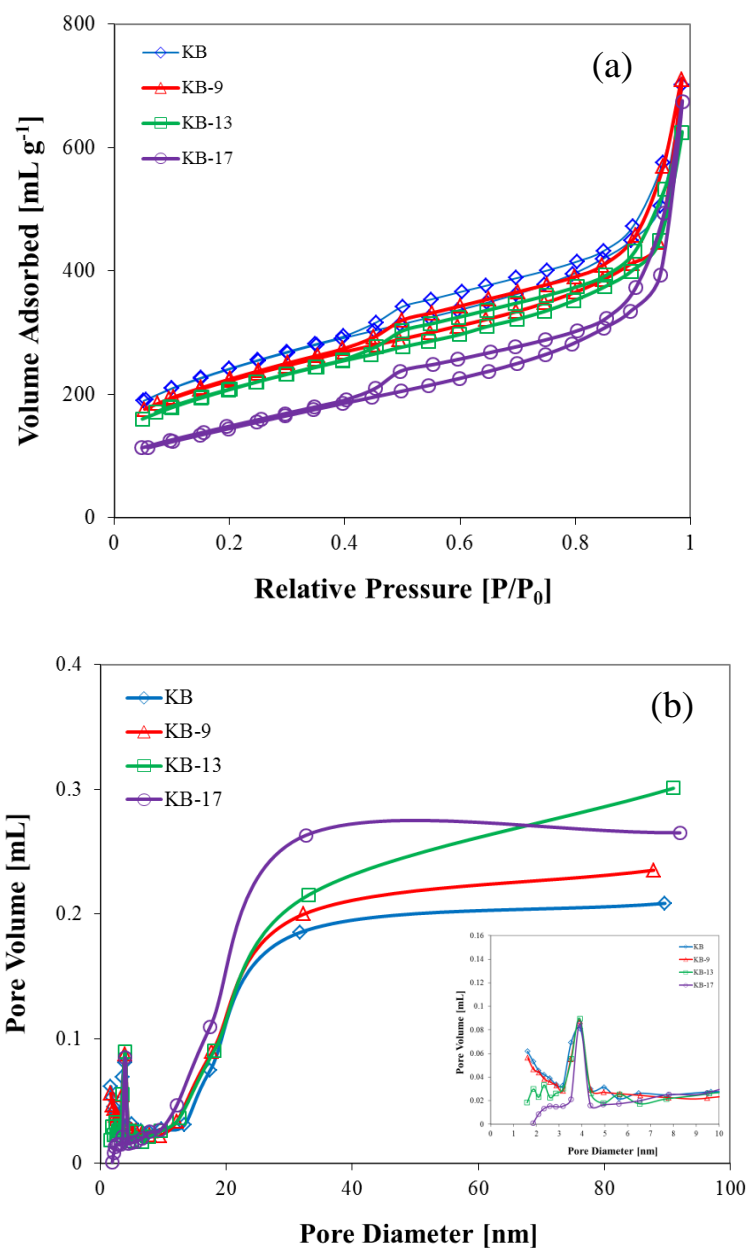


Figure 4.1 (a) N₂ adsorption/desorption isotherms and (b) BJH pore-size distribution curves obtained from the adsorption branch of KB heat-treated at different temperatures. The inset in (b) compares the PSD in the range 0-10 nm.

However, the peak pore volume at 3-4 nm is the same for all the supports as shown in Figure 4.1 (b) inset.

XRD patterns of the KB, KB-9, KB-13, and KB-17 are shown in Figure 4.2. XRD shows peaks for pure carbon material. The characteristic diffraction peaks of KB-17 at ca. 26, and 43 and 54° represent (002), (100), and (004) planes of hexagonal structural graphite, respectively. Based on (002) plane, as a function of temperature, the characteristic diffraction peaks are sharper with increased intensity and shift to more positive angles. Therefore, the interlayer spacing of KB-17 calculated from (002) plane is 0.3506 nm, while that of KB is 0.3607 nm. Since interlayer spacing of KB-17 shows closer to the graphite (0.3350 nm) than that of KB (JCPDS No. 41-1487), XRD results prove that the carbon surface is more crystallized and graphitized at elevated temperatures. Figure 4.3 (a)-(d) exhibit the Raman spectra for KB, KB-9, KB-13, and KB-17. All the supports show the D band and G band at ca. 1350 and 1600 cm^{-1} , respectively. The D band originates from structural defects and disorder-induced features on carbon, while the G band corresponds to the stretching vibration mode of graphite crystals [70, 126]. Two broad peaks at ca. 1200 and 1510 cm^{-1} are associated with carbon atoms outside of a perfectly planar graphene network (such as aliphatic or amorphous structures) and integrated five-member rings or heteroatoms in graphene-sheet structures, respectively [160-162]. The integrated intensity ratio of D band to the G band (I_D/I_G) is widely used for indicating the degree of graphitization or the defect quantity in graphitic materials. I_D/I_G for KB, KB-9, KB-13, and KB-17 are estimated to be 2.75, 2.80, 2.51, and 2.05, respectively, which is indicative of increase in the order of graphitization. In general, the results of Raman spectra agree well with the XRD analysis. The trend in

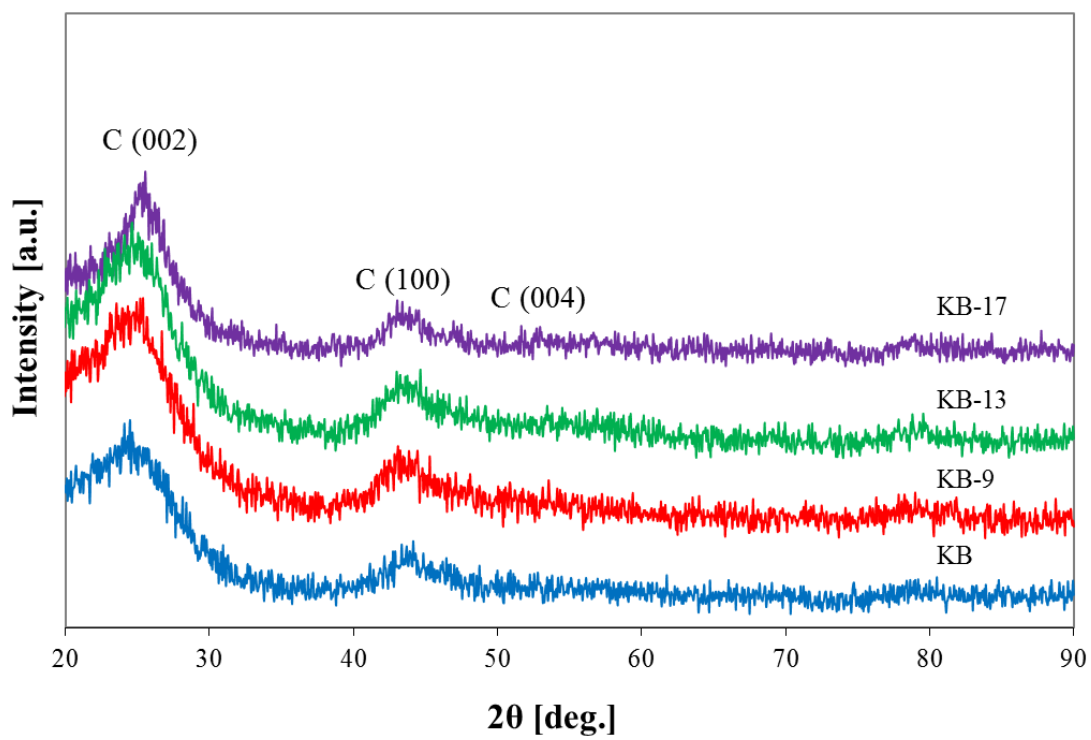


Figure 4.2 Comparison of XRD patterns of KB heat-treated at different temperature.

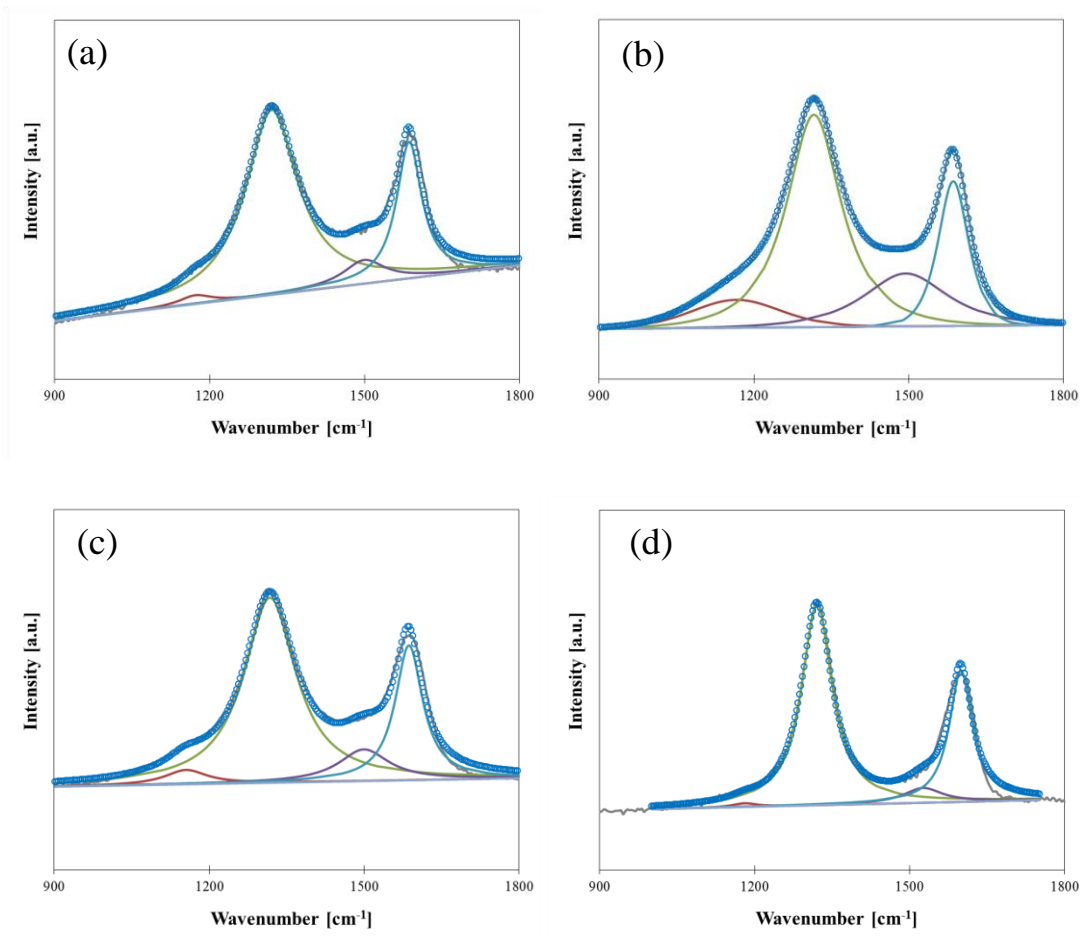


Figure 4.3 Raman spectra of (a) KB, (b) KB-9, (c) KB-13, and (d) KB-17.

specific surface area, interlayer spacing, and I_D/I_G as a function of temperature are shown in Figure 4.4 (a) and (b). In Figure 4.4 (a) and (b), as the temperature increases, the specific surface area, interlayer spacing, and I_D/I_G decrease. Both KB and KB-9 exhibit similar specific surface area, interlayer spacing, and I_D/I_G ratio. It suggests that the graphitic carbon starts to be formed between 900 and 1300 °C. The linear relation between the interlayer spacing and I_D/I_G is shown in Figure 4.4 (c). This relation exhibits that KB is more graphitized as the temperature is increased.

The HR-TEM images of KB and KB-17 are shown in Figure 4.5. KB is comprised of discontinuous and disordered graphite sheets, typical property of amorphous carbon [163] as shown in Figure 4.5 (a) and (b). HR-TEM images shown in Figure 4.5 (c) and (d) exhibit hollow structures for KB-17 with graphitic carbon outer layers. Thus, KB-17 possesses ordered and clear graphitic structure, while KB is apparently amorphous in nature.

4.3.2 CHARACTERIZATION OF PT ON KB AND KB-17

Figure 4.6 (a) shows the nitrogen adsorption-desorption isotherms of Pt/KB and Pt/KB-17. After Pt deposition, the isotherms of Pt/KB and Pt/KB-17 maintain the hysteresis loop with sharp adsorption and desorption branches in a relative pressure range of 0.4 – 0.8. Nitrogen uptake at a high relative pressure also indicates that both catalysts have mesoporous structure. Due to the blockade of pores by the loaded Pt nanoparticles [164], the specific surface areas of Pt/KB and Pt/KB-17 are reduced to 271 and 188 m² g⁻¹, respectively. Figure 4.6 (b) shows BJH PSD curves of Pt/KB and Pt/KB-17. In the range of large pore size (> 10 nm), there is no apparent difference between these

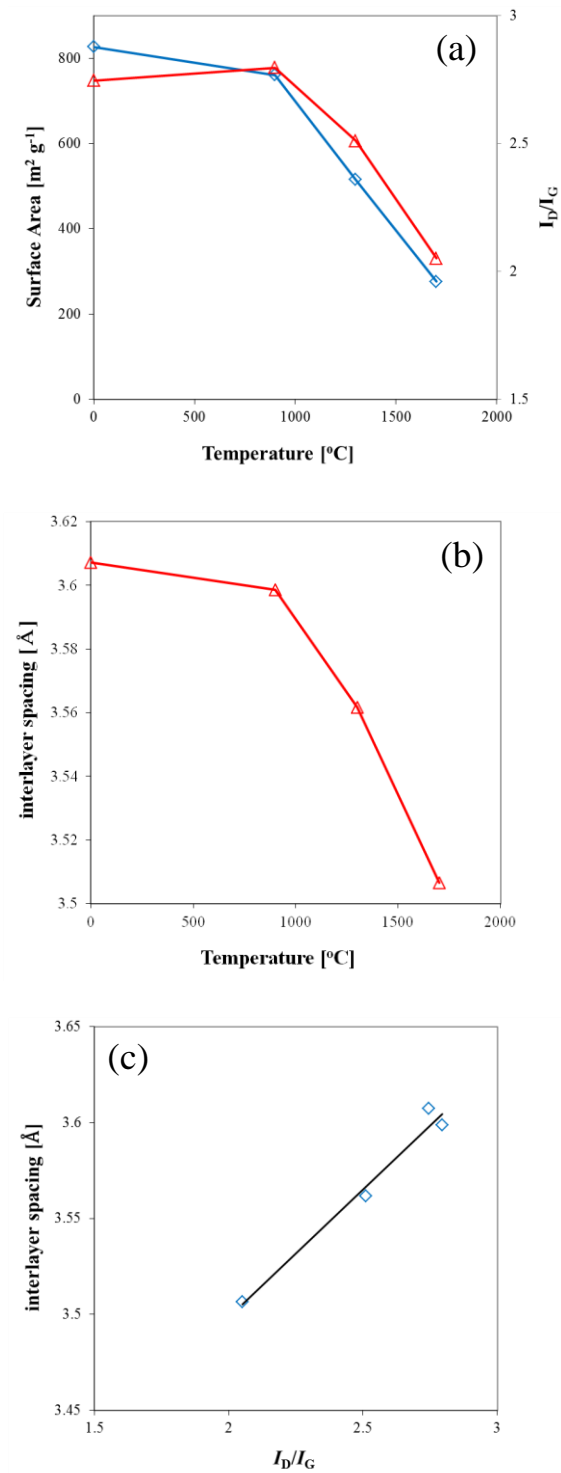


Figure 4.4 (a) Change of specific surface area and I_D/I_G as a function of temperature. (b) Change of interlayer spacing as a function of temperature. (c) Relationship between I_D/I_G and interlayer spacing.

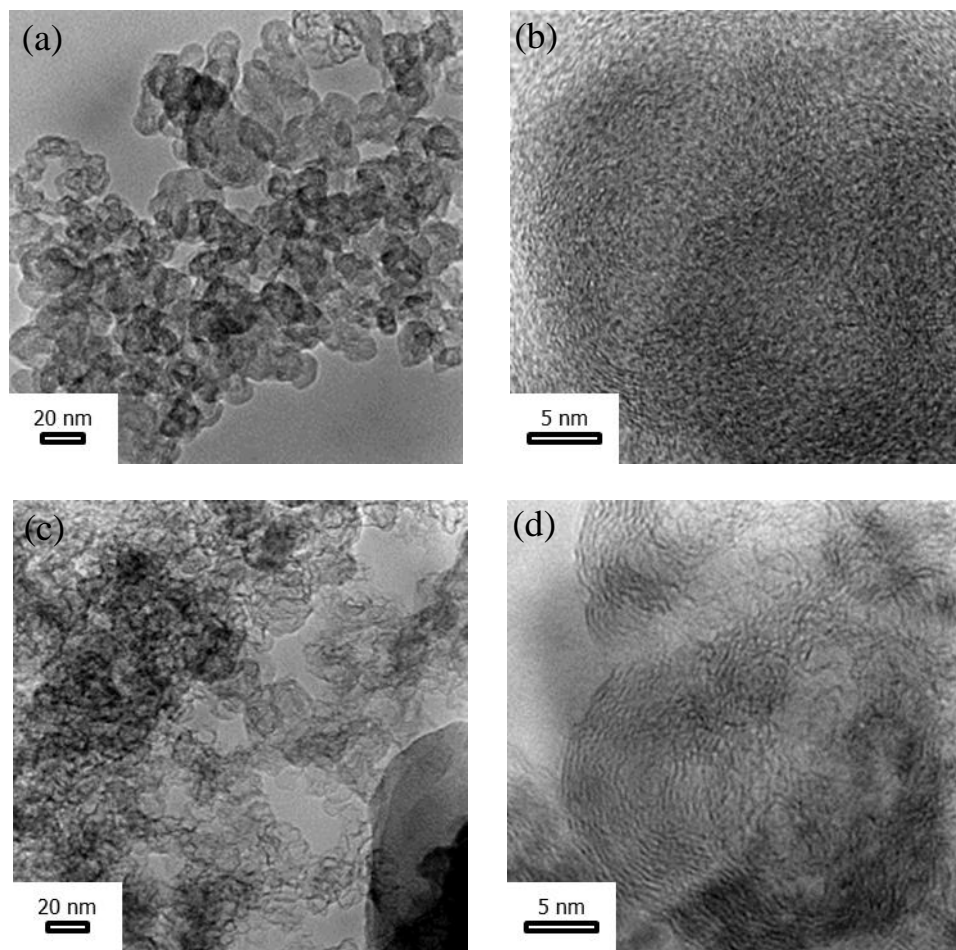


Figure 4.5 HR-TEM images of (a, b) KB and (c, d) KB-17.

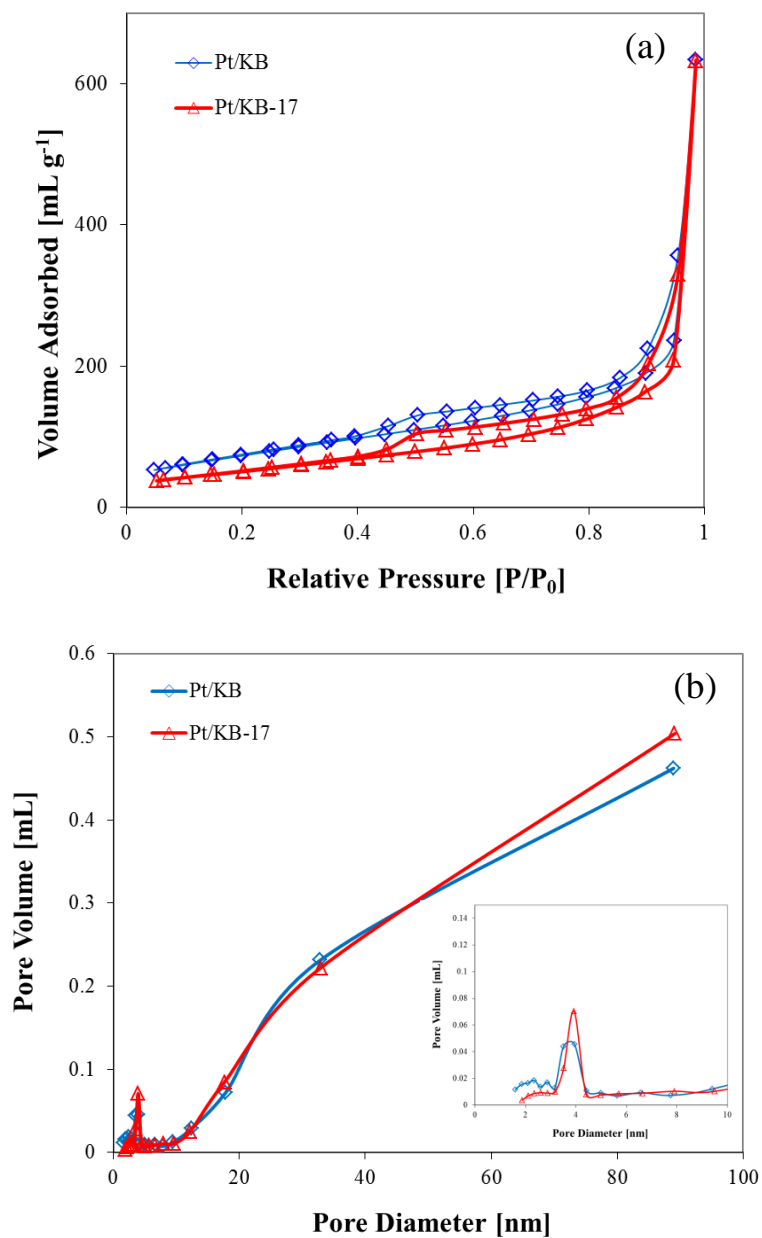


Figure 4.6 (a) N₂ adsorption/desorption isotherms and (b) BJH pore-size distribution curves obtained from the adsorption branch of Pt/KB and Pt/KB-17. The inset in (b) compares the PSD in the range 0-10 nm.

catalysts. In contrast, in the range of 2-3 nm, the pore volume of Pt/KB is decreased much comparing to fresh KB, while that of Pt/KB-17 exhibits no change before and after the Pt deposition, as shown in Figure 4.6 (b) inset. It suggests that the majority of Pt nanoparticles are deposited in the micro-pores of KB, whereas most of them are anchored on the meso and macro pores in the KB-17.

XRD patterns of Pt deposited on KB and KB-17 supports are shown in Figure 4.7. The characteristic diffraction peaks of Pt/KB and Pt/KB-17 at 39.8, 46.25, and 67.7° correspond to the (111), (200), and (220) planes of pure Pt, respectively (JCPDS No. 04-0783). Both Pt/KB and Pt/KB-17 exhibit the characteristics of the Pt with FCC structure. The mean particle size is determined from the (220) plane using the Scherer equation. According to the calculation, they have similar particle sizes, which results in no particle size effect on the catalytic activity and durability. The mean particle sizes are estimated to be 2.5, and 2.3 nm for Pt/KB and Pt/KB-17, respectively.

Figure 4.8 (a) and (b) show the HR-TEM images of Pt/KB and Pt/KB-17. Over 100 nanoparticles are used to measure the mean particle sizes and particle size distribution. The Pt nanoparticles are uniformly deposited and well-distributed on the supports. The mean particle sizes of Pt/KB and Pt/KB-17 are 2.6, and 2.5 nm, respectively which agrees well with the results obtained from XRD. Pt nanoparticles are dominantly distributed on both supports in the range of 2-3 nm. The SD is constant with 0.6 nm for both catalysts, which corresponds to the uniform Pt particle size distribution and larger numbers of sites for the deposition of Pt particles. XRD and HR-TEM results exhibit Pt nanoparticles with diameter of 2-3 nm and the narrow distribution, indicating

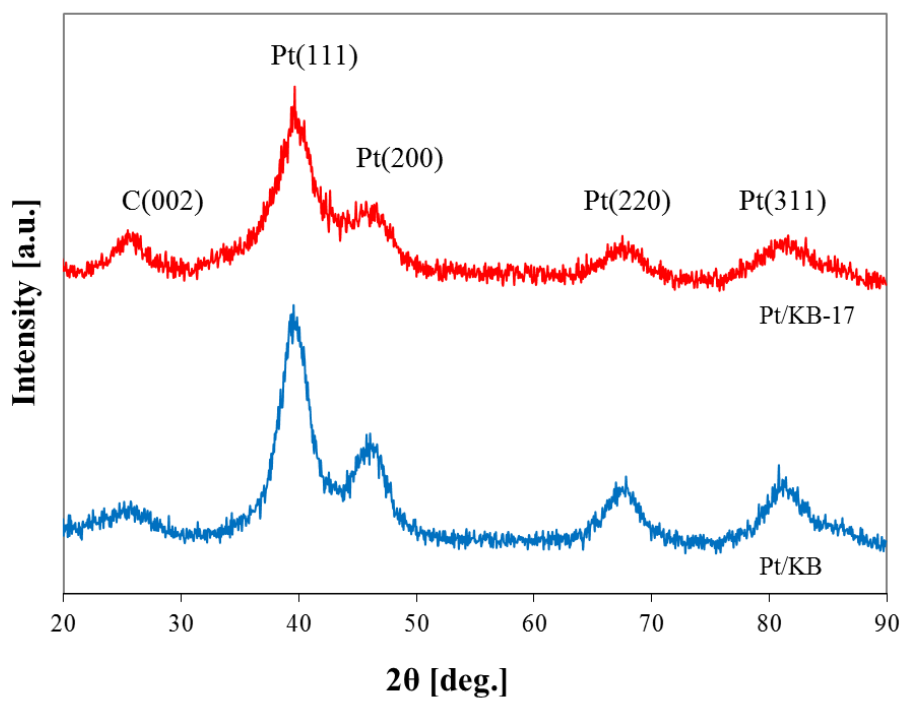


Figure 4.7 Comparison of XRD patterns of Pt/KB and Pt/KB-17 catalysts.

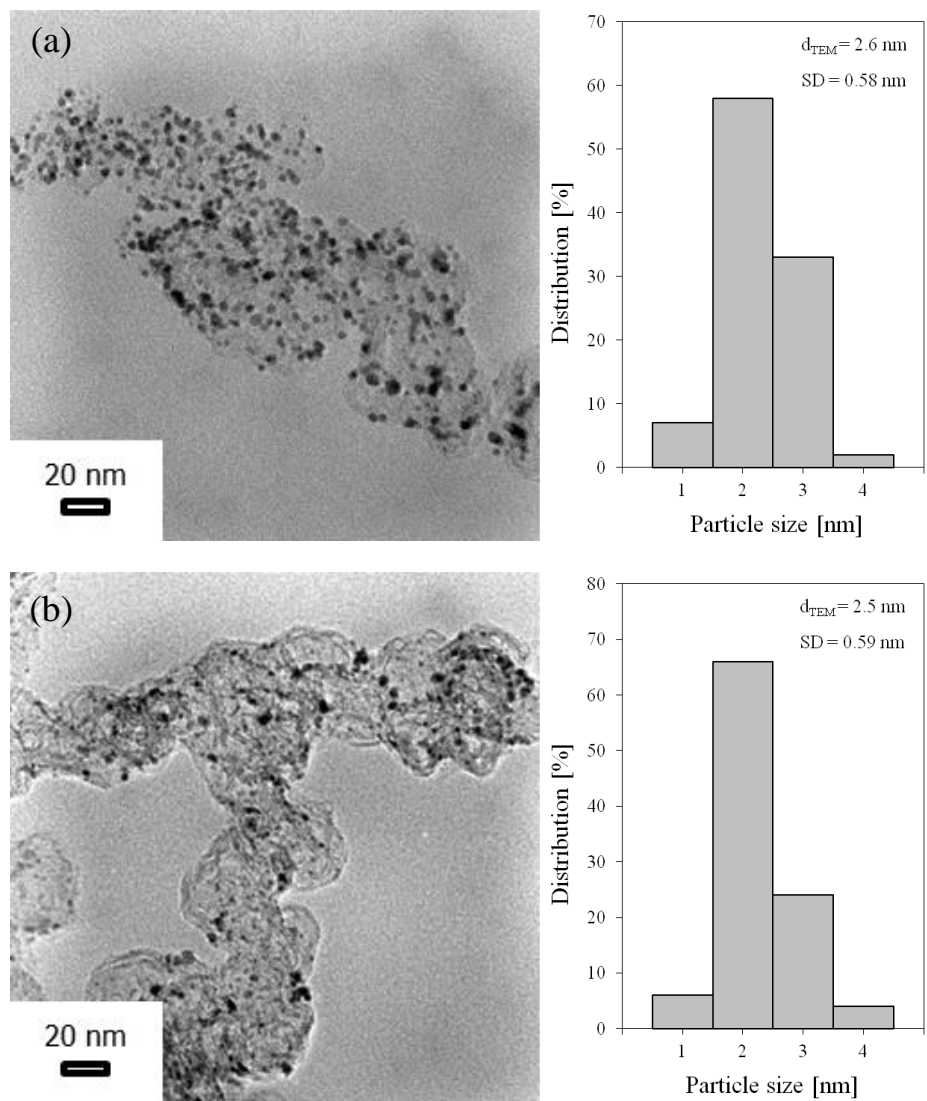


Figure 4.8 HR-TEM images of (a) Pt/KB and (b) Pt/KB-17 catalysts.

that effect of Pt catalyst particle size is well-controlled since carbon oxidation is accelerated in the presence of Pt [40].

4.3.3 ELECTROCHEMICAL PERFORMANCE AND DURABILITY OF Pt/KB AND Pt/KB-17

The LSVs of Pt/KB and Pt/KB-17 obtained at room temperature in oxygen-saturated 0.1 M HClO₄ electrolyte are shown in Figure 4.9 (a). The LSVs are recorded at a rotating rate of 1600 rpm and a scan rate of 5 mV s⁻¹ by sweeping the potential anodically (0.2 V and 1.05 V). The ORR is governed under kinetic dominated process at high potential region. The mixed kinetic-diffusion control is occurred at mid-potential regions, followed by a plateau of diffusion-limited current. The Pt/KB-17 exhibits better performance for the ORR than Pt/KB. The diffusion-limited current density of Pt/KB-17 is 5.02 mA cm⁻² while that of Pt/KB is 4.82 mA cm⁻². Furthermore, the half-wave potential of Pt/KB-17 is 0.85 V, while that of Pt/KB shows 0.841 V. For the on-set potential, the Pt/KB-17 exhibits more 20 mV more anodic potential than Pt/KB. The specific activities (A_s), which is calculated from ECSA and platinum loading, is shown in Figure 4.9 (a) inset in the region of 0.8 and 0.5 V. The result indicates higher catalytic activity for Pt/KB-17 when compared to Pt/KB towards ORR in the whole region of 0.8 and 0.5 V.

To compare the activity of these catalysts in the kinetic region, Tafel plots for the Pt/KB and Pt/KB-17 in Figure 4.9 (b) are obtained from LSV diagram using the following equation [165]:

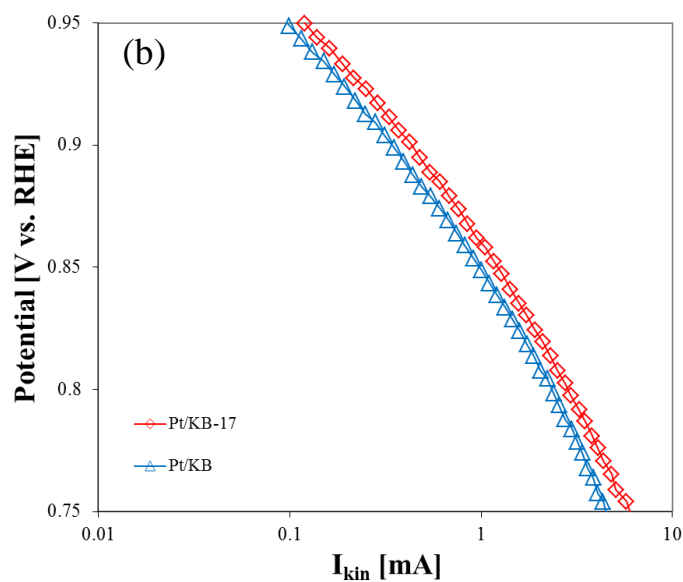
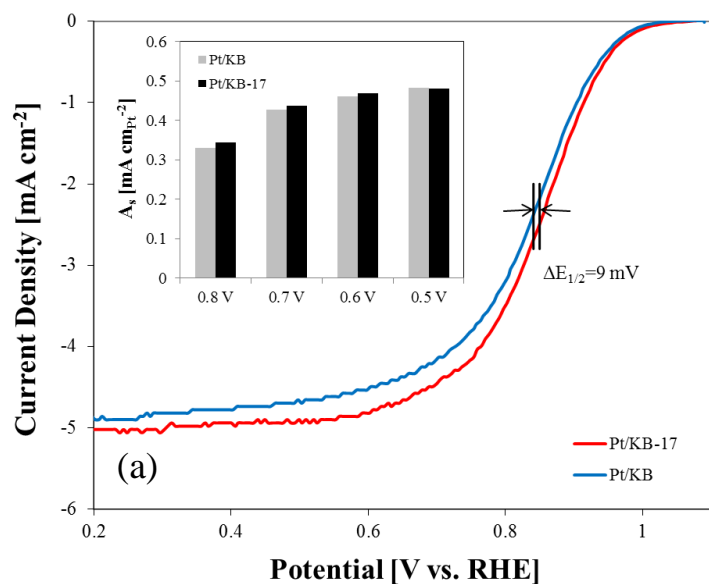


Figure 4.9 (a) LSV curves of Pt/KB and Pt/KB-17 catalysts in O_2 -saturated 0.1 M $HClO_4$ at room temperature and scan rate of 5 mV s^{-1} with 1600 rpm. The inset in (a) shows specific activities calculated from ECSA and platinum loading. (b) Tafel plots from LSV data of Pt/KB and Pt/KB-17 catalysts at 1600 rpm.

$$\frac{1}{i} = \frac{1}{i_k} + \frac{1}{i_{dl}} \quad [4.3]$$

$$i_k = \frac{i_{dl} \cdot i}{i_{dl} - i} \quad [4.4]$$

where i is the measured current in LSV experiment, i_k is the mass transport free kinetic current, and i_{dl} is the diffusion-limited current. The Pt/KB-17 catalyst shows higher kinetic current than Pt/KB. For example, i_k of the Pt/KB-17 is 1.28 mA, while that of Pt/KB is 0.91 mA. Consequently, for the kinetic, mixed, and diffusion-limited regions, the Pt/KB-17 represents superior performance for ORR than Pt/KB.

Figure 4.10 (a) and (b) show the polarization and power density curves of Pt/KB and Pt/KB-17 before and after potential cycling between 1.0 and 1.5 V, respectively. In Figure 4.10 (a), the polarization curves of Pt/KB are compared to those of Pt/KB-17. As shown in LSV results, the fuel cell tests also show higher performance for Pt/KB-17 higher than that for Pt/KB. At 0.6 V, the Pt/KB catalyst shows an initial current density of 610 mA cm⁻², while Pt/KB-17 exhibits 716 mA cm⁻². After 1000 cycles, for the Pt/KB, the current density at 0.6 V is 228 mA cm⁻², while Pt/KB-17 after 3000 cycles shows 788 mA cm⁻². Moreover, a potential gain of 8 mV at 1600 mA cm⁻² is observed for the Pt/KB-17. Figure 4.10 (b) exhibits the power density loss of Pt/KB and Pt/KB-17 catalysts after potential cycling experiment. The maximum power density of Pt/KB is 498 mW cm⁻², while that of Pt/KB-17 is 585 mW cm⁻², indicating 17% increase when compared with Pt/KB. After 1000 cycles, for the Pt/KB, 64% loss in the maximum power density is observed, while the Pt/KB-17 shows 3% gain after 3000 cycles. Since, the Pt nanoparticles on both supports practically show the same properties in the HR-TEM and XRD, the enhancement in initial performances are likely to have come from the

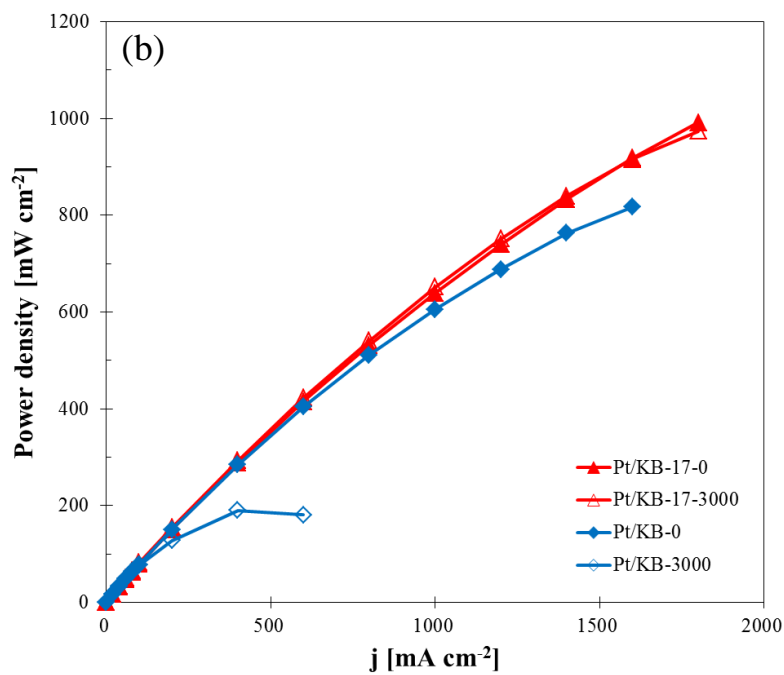
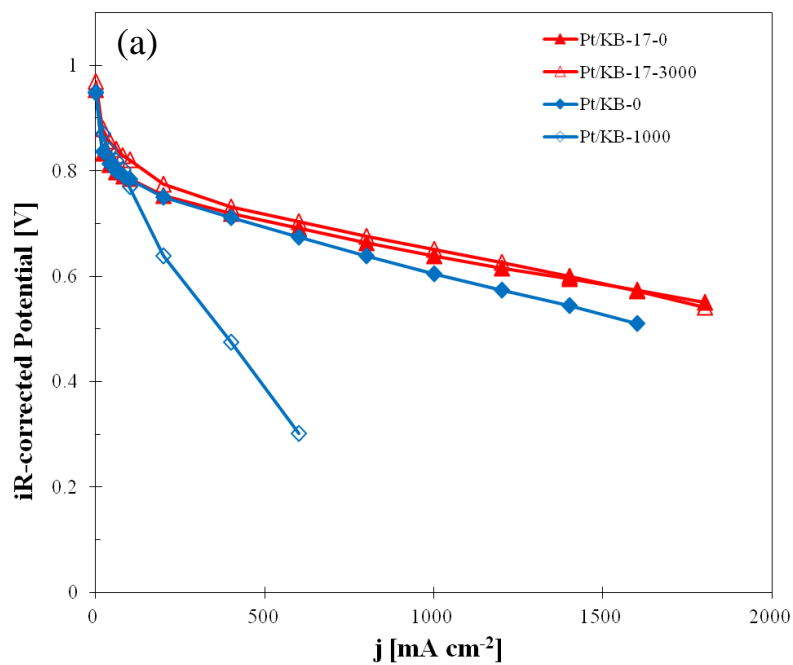


Figure 4.10 (a) H_2/air polarization and (b) the power density curves of Pt/KB and Pt/KB-17 catalysts before and after 3,000 potential cycles between 1.0 and 1.5 V.

difference in the nature of the supports used. First, in the case of Pt/KB, the Pt nanoparticles are filled in the micro-pores as discussed in Figure 4.6. It is well-known that the initial performance of amorphous carbon supported Pt in the RDE and MEA test is lower than that of graphitized carbon supported Pt, since micro pores can inhibit the reactant flow from contacting the Pt catalyst surface efficiently [163, 166, 167]. Additionally, the electrical conductivity is increased since the oxygenated functional groups are removed at the high temperature [98, 168, 169]. Liu et al. reported that the Pt/GCB exhibits enhanced electro-catalytic activity in terms of both efficiency and kinetics for the ORR [163]. Since the heat treatment process removes most of the surface defects on the CB, and the oxygen molecules can be adsorbed on the defect-free surface, improvements in ORR catalytic activity and kinetics are observed. Moreover, the graphitized carbon showed even lower mass transport resistance than as-received carbon due to the insufficient adsorption of oxygen molecules on the surface of the as-received carbon with a number of defect sites. It agrees well with the MEA tests in this study, since Pt/KB-17 outperforms Pt/KB in the mass transport dominant high current density region as shown in Figure 4.10.

To further evaluate the durability, the ECSA change is shown in Figure 4.11 as a function of number of potential cycles for Pt/KB and Pt/KB-17 catalysts. After 1000 cycles, the initial ECSA of Pt/KB remains only 39% of the initial value ($32 \text{ m}^2 \text{ g}_{\text{Pt}}^{-1}$), indicating severe carbon corrosion. However, the ECSA of Pt/KB-17 retains 84% after 1000 cycles, which indicates that the Pt/KB-17 is even more stable than the Pt/KB under high potentials. For the Pt/KB-17, 54% of initial ECSA ($60 \text{ m}^2 \text{ g}_{\text{Pt}}^{-1}$) is retained after 3000 cycles. As seen in this result, the trend of mass activity is in good agreement with that of

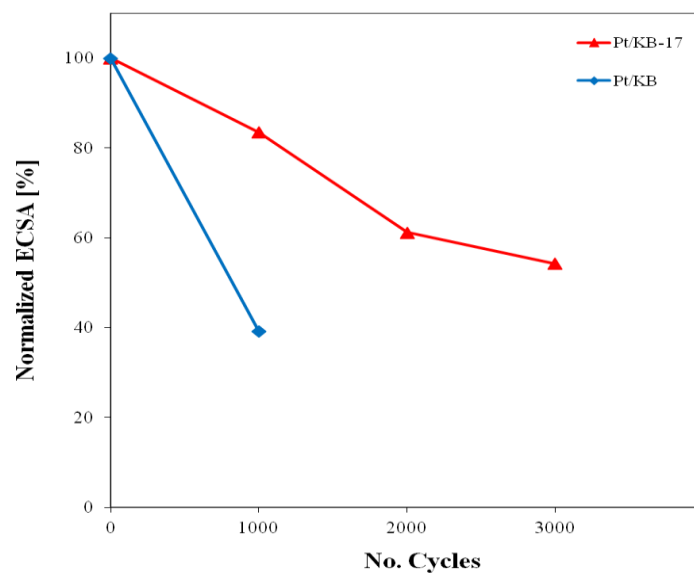
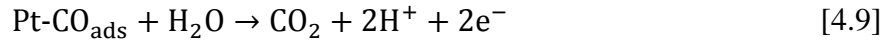
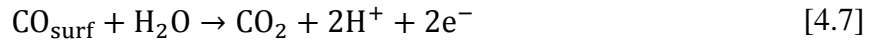
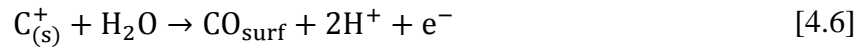


Figure 4.11 Normalized ECSA of Pt/KB and Pt/KB-17 as a function of cycle number. ECSAs were calculated from cyclic voltammograms obtained between 0.05 and 0.6 V (vs. RHE) at 80 °C. Fully humidified H₂ (200 sccm) and N₂ (75 sccm) were supplied to the anode and the cathode, respectively.

ECSA change. These results clearly indicate that the Pt/KB-17 catalyst is remarkably stable when compared to the Pt/KB. The high stability is attributed to the graphitic nature of KB-17 support

In H₂/air polarization studies, the Pt/KB exhibits a large voltage drop after 1000 cycles due to carbon corrosion and subsequent processes such as Ostwald ripening, detached Pt particles, Pt particle migration and agglomeration under star-up/shutdown condition [170]. The electrochemical corrosion of the carbon surface led to changes in the surface chemistry of the carbon and an increase in the hydrophilicity of the catalyst layer and the GDL, which affects the transport behavior of the reactant gas and product water [165]. The carbon corrosion mechanism in PEMFCs is suggested as follows [171]



According to the suggested mechanism, the electrochemical formation of C_(s)⁺ surface sites occurred initially followed by a rapid hydrolysis into carbon surface oxides (CO_{surf}). Then, the Pt nanoparticles accelerate the CO₂ evolution reaction through eq 4.4 and eq 4.5 instead of eq 4.3. The amorphous carbon or defective sites are oxidized at low potential (< 1.0 V). The nanostructural change of carbon can mitigate the carbon oxidation reaction as described above. As shown in Figure 4.4, as the heat treatment temperature is increased, the specific surface area of carbon is decreased and degree of graphitization is increased, which indicates that the Pt/KB-17 catalyst is more

hydrophobic and corrosion-resistant than Pt/KB. Furthermore, as the degree of graphitization increased, π -bonds in graphitized carbon support are also increased. Subsequently, the interaction between π -bonds and the Pt particles is relatively strong for the graphitized carbon, which results in the enhanced durability of the Pt catalysts [168, 169].

4.4 CONCLUSION

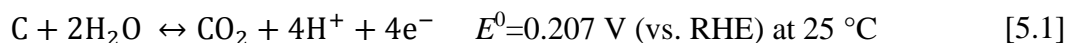
In this study, change in carbon nanostructure by means of high temperature treatment enhanced the support properties required for PEMFCs. The support stability in the presence of Pt was evaluated using a potential cycling protocol (1.0-1.5 V). In order to enhance the durability, it is necessary to understand the important factors such as ECSA, ORR, and morphology of the support. The study shows that the carbon nanostructure and degree of graphitization play a key role in enhancing the support stability during startup/shutdown condition. As expected, higher temperature treatment leads to increasing in both degree of graphitization and corrosion resistance. Since the both KB and KB-17 carbon supports were treated with an effective surface activation process, Pt nanoparticle size is similar in both the disordered amorphous (KB) and ordered graphitized carbon (KB-17), which indicates no particle size effect on the support stability during high potential cycling. In this study, we have found that the graphitization at 1700 °C exhibits remarkable enhancement in support stability at high potentials when compared with the pristine amorphous carbon (KB).

CHAPTER 5

ENHANCED DURABILITY OF CO-DOPED Pt/GCCC CATALYST UNDER POTENTIAL CYCLING FOR PEMFCs

5.1 INTRODUCTION

PEMFCs enable the direct production of electricity from chemicals with higher efficiency, noiseless operation, and without pollutant emissions as compared to conventional internal combustion engines. However, there are still some problems to solve in order to advance to commercialization like the cost and durability of catalysts. In general, the catalysts are comprised of Pt nanoparticles and high surface area carbon which has the ideal properties as a support such as high electric conductivity, high surface area, and porosity. Degradation mechanisms for catalysts involve dissolution of Pt [12, 85-89], migration of Pt [155, 156], and carbon corrosion [95-99]. In terms of carbon corrosion, the carbon support is electrochemically oxidized under PEMFC environment such as high temperature and humidity, since the standard electrode potential of carbon is very low as below.



Furthermore, according to a reverse-current decay mechanism, after the shut down or during start-up, the cathode can be degraded by a higher potential than the OCV. Such a high potential rapidly oxidizes the carbon support [31, 35]. As the carbon support is oxidized, the Pt nanoparticles aggregate to form larger particles and the catalyst layer

porosity is changed [157, 158]. These results bring about the reduction of ECSA and decreased performance.

To enhance the durability of carbon supports, a variety of research has been investigated to identify alternate carbon-based supports, for example, CNCs [172, 173], CNTs [41, 174, 175] and graphene [176-178]. Lim et al. [172] investigated CNC obtained from acetylene black heat treated at 2800 °C. The corrosion-resistance of a CNC in a PEMFC was investigated by on-line mass spectrometry to measure CO₂ generation at a constant potential of 1.4 V for 30 min. The CNC showed significant resistance to electrochemical corrosion, exhibiting low performance degradation of only about 2.3% after the corrosion test. Wang et al. [173] prepared N-doped graphitic hollow CNCs by spray pyrolysis and heat treatment with sulfur. When tested under fuel cell operating conditions, Pt/CNC exhibited almost no degradation for both HOR and ORR, compared with the apparent degradation observed for a commercial catalyst. Such a remarkable catalytic activity and durability were attributed to strong oxidation resistance and strong interaction with Pt particles due to their graphitization and concurrent N doping.

Zhang et al. [174] fabricated nanocomposites of poly(diallyldimethylammonium chloride) (PDDA) and graphitic carbon nanotubes (GCNTs) using electrostatic self-assembly technology. The potential step method (1.4–0.85 V) for 44 h was applied to test the durability in N₂-saturated 0.5 M H₂SO₄ solution. After the degradation test, Pt/PDDA-GCNTs exhibited even higher durability and activity than Pt/CNTs and Pt/XC-72 in terms of both ECSA and ORR. Lv et al. [179] heat-treated the carbon nanotubes under NH₃ atmosphere (H-CNTs-1000) to enhance the durability of the support. The electrochemical oxidation at 1.2 V for 48 h showed that the H-CNTs-1000 have a higher

resistance to electrochemical oxidation than the CNTs. They conducted potential cycling test between 0.6 and 1.2 V for 1000 cycles. After 1000 cycles, the ECSA of Pt/H-CNTs-1000 remained 40.5%, while that of the Pt/CNTs remained only 22.9%.

Tiwari et al. [180] reported that graphene oxide (GO) non-covalently interacted with genomic DNA significantly improved the durability of the support. The ECSA loss after 10,000 cycles between 0.6 and 1.2 V was only 6% while ~48% and ~60% of ECSA loss was observed for the Pt/GO and Pt/C catalysts, respectively. Jung et al. [176] prepared the GO from expandable graphite with Hummers method. The catalysts were examined between 0.4 and 1.2 V for 60 min. The ECSA of Pt/GO showed 17.81% loss while that of Pt/C showed 43.15% loss. For MEAs tests, the commercial Pt/C exhibited 45.4% loss while the mixture of Pt/C and Pt/GO (Pt/C: Pt/GO =8:2) showed 17.7% loss after 3 h holding at constant 1.4 V.

In our previous study, we reported a novel route of preparing Co-doped Pt catalysts on CCC as supports [85]. As described in Chapter 3, unlike the general impregnation method, in our novel synthesis, Co was initially doped into the carbon materials at high temperature using Co-catalyzed pyrolysis which later was used as the Co metal source for the formation of Co-doped Pt. The Co-doped carbon thus prepared was used as a support to deposit Pt nanoparticles. The Pt supported on Co-doped carbon was heat-treated under reducing atmosphere to obtain Co-doped Pt catalyst with controlled particles size. During the heat-treatment, Co which is doped within the carbon diffuses to the surface and forms Co-doped Pt catalyst with a core-shell structure. In the present study, the CB was heat-treated at high temperature to obtain highly graphitized carbon support. Since the pristine CB is amorphous, there is a limitation at high potentials

in order to use as a support in practical application. In this chapter, the kinetic activity and durability of Co-doped Pt catalysts prepared by the novel approach using the pristine and graphitized CB as catalyst supports.

5.2 EXPERIMENTAL

5.2.1 PREPARATION OF SUPPORT AND CATALYST

All the details for the preparation of CCC are described in Chapter 3. In brief, to obtain graphitized carbon composite catalyst (GCCC), as-received CB (Ketjen Black EC-300J) was heat-treated at 1700 °C for 1 h under N₂ atmosphere. Then, the material was oxidized in 9.8 M HNO₃ solution at 85 °C for 9 h under refluxing conditions. After filtering, the oxidized carbon was washed with DI water several times and dried under vacuum at 80 °C for 12 h. A desired amount of Co(NO₃)₂ and ethylene diamine, used as Co and N precursors, respectively, were mixed with the oxidized carbon in 200 ml IPA. The mol ratio of Co and N precursors was maintained at 1:9. The mixture was refluxed for 3 h at 85 °C under vigorous stirring, followed by drying under vacuum at 80 °C. The resultant powder was subjected to heat-treatment under inert atmosphere at 800 °C for 1 h followed by leaching in 0.5 M H₂SO₄ at 80 °C for 3 h to remove excess Co. The final product is denoted as GCCC. The supports were non-covalently activated by the PCA before the Pt deposition due to their high hydrophobicity deposition [121, 122] .

Pt deposition was accomplished by a polyol reduction method for the preparation of 30% Pt/GCCC catalyst. First, the GCCC support was dispersed in 25 ml of ethyleneglycol in a sonication bath (Branson ultrasonic cleaner). A desired amount of PtCl₄ was added and the pH was adjusted to 11 by the addition of 0.5 M NaOH solution.

The resulting solution was refluxed at 160 °C for 3 h and allowed to cool to room temperature. Then, the solution was filtered, washed with DI water, and dried at 160 °C for 1 h. Prior to heat-treatment, the Pt/GCCC was subjected to a protective coating procedure. Oxidative polymerization of aniline sulfate was carried out at room temperature using ammonium peroxydisulfate as the oxidizing agent [123, 124]. The polyaniline-coated Pt/GCCC was placed in an alumina crucible and heat-treated at 800 °C for 2 h in a tubular furnace under 5% H₂ (balance N₂) atmosphere. The catalyst thus prepared is denoted as Co-doped Pt/GCCC. Finally, the molar ratio of Pt to Co in both Co-doped Pt/CCC and Co-doped Pt/GCCC is 1:1. Similarly, Co-doped Pt/CCC was synthesized using CCC as the support. For comparison, Pt/C is prepared with the same polyol reduction method using Ketjen Black EC-300J.

5.2.2 PHYSICAL CHARACTERIZATION

The nitrogen adsorption/desorption isotherms were obtained at -196 °C using a Quantachrome NOVA 2000 BET analyzer. Specific surface area was determined by a multipoint BET analysis. PSD curves were calculated by the BJH method using the adsorption/desorption branch. XRD analysis was performed using a Rigaku D/Max 2500 V/ PC with a Cu K α radiation. A tube voltage of 30 kV and a current of 15 mA were used during the scanning. To estimate the particle size of samples, we employed the following Scherrer equation [66]:

$$D = \frac{k\lambda}{10B \cos \theta} \quad [5.2]$$

where D is the crystallite size in nm, k is a coefficient (0.9), λ is the wavelength of X-ray (1.5404 Å), B is the line broadening at half the maximum intensity in radians, and θ is the

angle at the position of the maximum peak known as Bragg angle. Raman spectroscopy was used to evaluate the degree of graphitization of the carbon supports using HORIBA "LABRAM 1B" (He-Ne 20mW laser, wave length 632.817 nm). ICP-AES (Perkin Elmer) analysis was used to determine the composition of the catalysts. HR-TEM was used to study the morphology and particles size distribution of the catalysts using Hitachi 9500 HR-TEM operated at 300 kV accelerating voltage. XRF (Fischer XDAL) was used to determine PtCo composition in the catalyst and Pt loading in the catalyst coated membrane.

5.2.3 MEA FABRICATION AND ELECTROCHEMICAL MEASUREMENT

For the MEA fabrication, the in-house synthesized catalysts were employed as the cathode catalyst while commercial 46% Pt/C was used as a catalyst for the anode. Catalyst inks were prepared by ultrasonically mixing the appropriate amount of catalysts, IPA (1.8 ml), Nafion[®] ionomer (5% solution, Alfa Aesar), and DI water (0.2 ml). The ionomer content was 30% and 20% in the anode and cathode inks, respectively. The catalyst inks were sprayed directly on the Nafion[®] 212 membrane covering an active area of 25 cm². The Pt loading on the anode and cathode electrodes is kept at 0.1 and 0.15 mg cm⁻², respectively. The catalyst coated membrane was then hot pressed at 140 °C using a pressure of 20 kg cm⁻² for 6 min. in between the gas diffusion layers (Sigracet GDL 10BC, SGL) and Teflon gaskets to prepare the MEA for the performance evaluation studies in fuel cell.

The initial mass activity at 0.9 V_{IR-free} was evaluated under H₂/O₂ (2/9.5 stoic.) at 80 °C, 100% RH, and 150 kPa_{abs.} back pressure. Polarization curves were obtained at

80 °C, and 170 kPa_{abs} back pressure supplying H₂ and air (2/2 stoic.) humidified at 50% RH. The ECSA was estimated using CV experiments carried out between 0.05 and 0.6 V (vs. RHE) at 80 °C under fully humidified H₂ and N₂ supply to the anode and the cathode, respectively. During AST, H₂ and N₂ were supplied to the anode and cathode, respectively and the potential was swept between 1 and 1.5 V (vs. RHE) at 500 mV s⁻¹ in a triangle profile for the durability evaluation, respectively [125]. The fuel cell polarization was conducted using a fully automated fuel cell test station (Scribner Associates Inc., model 850e) at 80 °C.

5.3 RESULTS AND DISCUSSION

5.3.1 CCC AND GCCC SUPPORT SYNTHESIS

Figure 5.1 (a) and (b) show the nitrogen adsorption-desorption isotherms and BJH PSD curves of CB, CCC and GCCC. The specific surface area of CB is 826.4 m² g⁻¹. The specific surface area of CCC is 397.7 m² g⁻¹, while the GCCC has 284.3 m² g⁻¹. The isotherms of CCC and GCCC show hysteresis loop with sharp adsorption and desorption branches over a relative pressure range of 0.4 – 0.8, while GCCC show larger hysteresis than CCC relatively, as shown in Figure 5.1 (a). In addition, nitrogen uptake for CCC and GCCC is observed at a relatively high pressure of 0.94–1.0, which is associated with the presence of mesopores [67]. The isotherms of CCC and GCCC exhibit characteristic Type IV by the IUPAC classification indicating that CCC and GCCC are the mesoporous support [67]. The total pore volumes of CCC and GCCC are 0.846 and 0.688 ml g⁻¹, respectively. In Figure 5.1 (b), CCC show larger pore volume than GCCC in pore diameter over 20 nm or less than 3 nm, while GCCC exhibits larger pore volume than

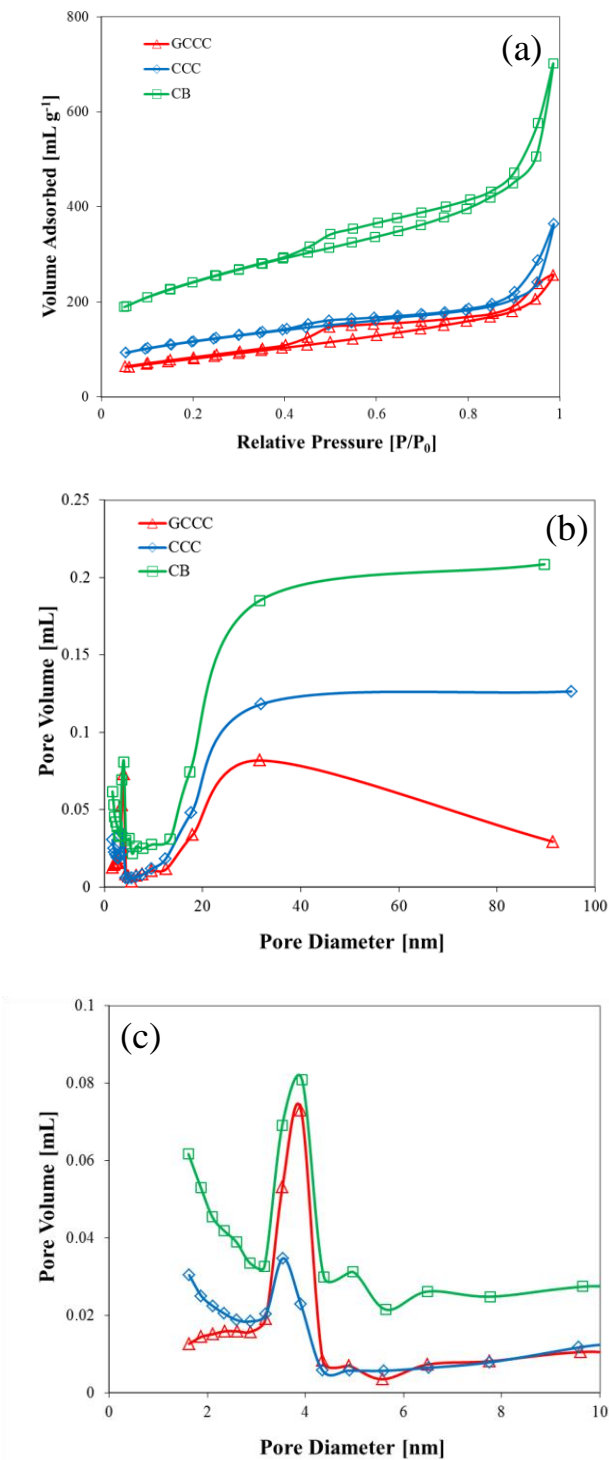


Figure 5.1 (a) N₂ adsorption/desorption isotherms and (b) BJH pore-size distribution curves obtained from the adsorption branch of GCCC, CCC and CB. (c) BJH pore-size distribution in the range 0-10 nm.

CCC in pore diameter between 3 and 4 nm, suitable sites for deposition of Pt nanoparticles. Like the CB, both CCC and GCCC show that the peak pore diameter under 10 nm stays at ca. 4 nm, as shown in Figure 5.1 (c).

The results of XPS analysis performed on the CB, CCC and GCCC supports are presented in Figure 5.2. Figure 5.2 (a) shows the survey scans for the CB, CCC and GCCC. The nitrogen atom is not observed in the survey scan of CB. XPS spectra of CCC and GCCC show a peak at ~398 eV which corresponds to the nitrogen atom on the surface of CCC and GCCC supports, as shown in Figure 5.2 (a). The nitrogen peaks shown in Figure 5.2 (b) and (c) for CCC and GCCC, respectively, can be deconvoluted into four major peaks corresponding to pyridinic, pyrrolic and/or pyridone, quaternary, and pyridinic-N⁺-O⁻ (oxidized nitrogen). The peak at ca. 398.4 eV accounts for the presence of pyridinic-N whereas the peak at ca. 400.3 eV corresponds to the pyrrolic-N and/or pyridine-N. The peaks at ca. 401.1 and ca. 403.4 eV are ascribed to the presence of quaternary-N and pyridinic-N⁺-O⁻, respectively. For CCC, relative percentages of pyridinic-N and pyrrolic-N and/or pyridine-N are 41.0 and 38.5% of total nitrogen, respectively. Quaternary-N accounts for 6.6% while pyridinic-N⁺-O⁻ occupies 13.9%. For GCCC, pyridinic-N and pyrrolic-N and/or pyridine-N contain 27.8 and 37.0%, respectively. Quaternary-N and pyridinic-N⁺-O⁻ comprise 19.3 and 15.9%, respectively. The percentages of pyrrolic-N and/or pyridine-N and pyridinic-N⁺-O⁻ show similar in CCC and GCCC. Pyridinic-N in GCCC exhibits less than that in CCC, while quaternary-N in GCCC shows more than that in CCC. It is well-known that quaternary-N plays an important role in stability of catalyst in ORR [55, 56, 61, 70], while pyridinic-N situated

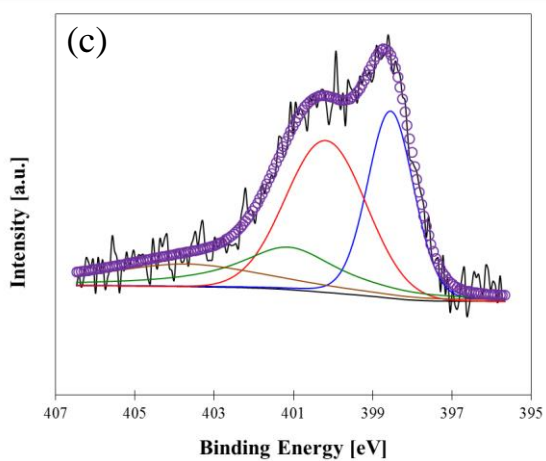
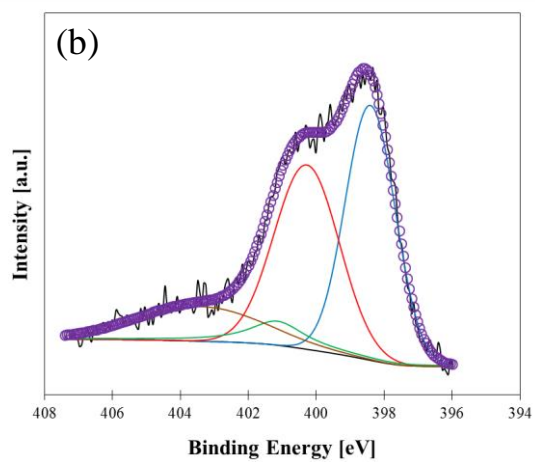
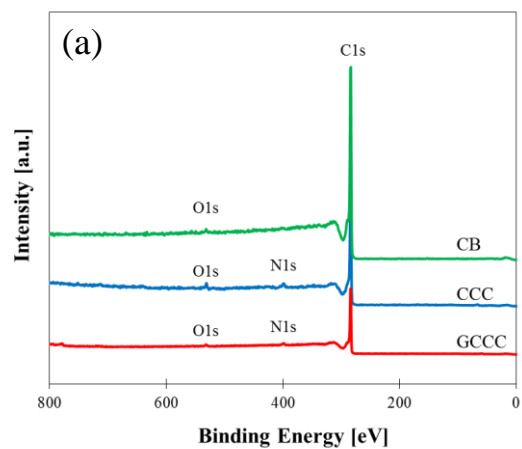


Figure 5.2 (a) XPS survey scans of GCCC, CCC and CB. Deconvoluted N1s XPS spectra of (b) CCC and (c) GCCC.

on the edge of the graphite planes promotes ORR by donating one p-electron to the aromatic π system [55, 68, 69].

XRD patterns of the CB, CCC, and GCCC are shown in Figure 5.3 (a). The Co metal is not observed in the XRD pattern of CB. The characteristic diffraction peaks of Co metal at ca. 44.2, 51.5, and 75.8° represent (111), (200), and (220) planes in both CCC and GCCC supports, respectively (PDF#97-007-6632). The XRD results confirm the presence of Co metal after acid-leaching at high temperature. Based on the carbon, the characteristic diffraction peaks of GCCC are sharper with increased intensity and shift to more positive angles. Therefore, the interlayer spacing of CCC based on (002) plane decreases to 0.3483 nm, while that of GCCC is 0.3463 nm. Figure 5.3 (b) and (c) exhibit the Raman spectra for CCC and GCCC. Both CCC and GCCC show the D band and G band at ca. 1350 and 1600 cm^{-1} , respectively. The D band originates from structural defects and disorder-induced features on carbon, while the G band corresponds to the stretching vibration mode of graphite crystals [70, 126]. Two broad peaks at ca. 1200 and 1510 cm^{-1} are associated with carbon atoms outside of a perfectly planar graphene network (such as aliphatic or amorphous structures) and integrated five-member rings or heteroatoms in graphene-sheet structures, respectively [160-162]. The integrated intensity ratio of D band to the G band (I_D/I_G) is widely used for indicating the degree of graphitization or the defect quantity in graphitic materials. I_D/I_G for CCC and GCCC is estimated to be 3.11 and 2.11, respectively, indicating that GCCC is more graphitized than CCC. These results combined with the Raman spectroscopy verify that the carbon surface of GCCC has been more graphitized than CCC which is already partially graphitized during metal-catalyzed pyrolysis as shown in chapter 3.

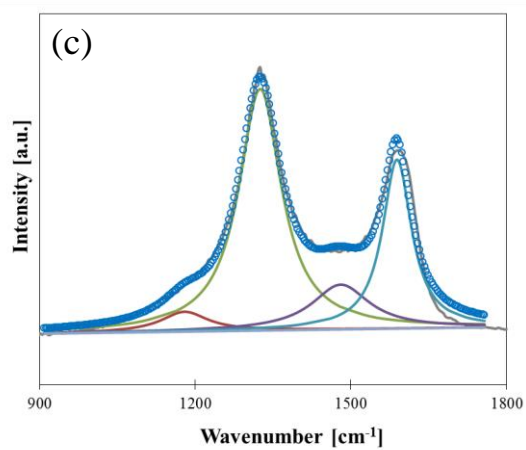
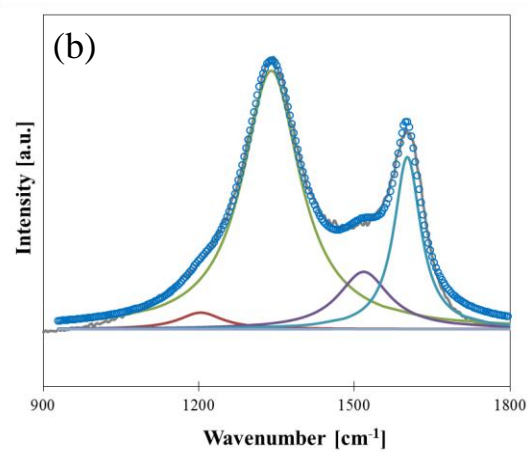
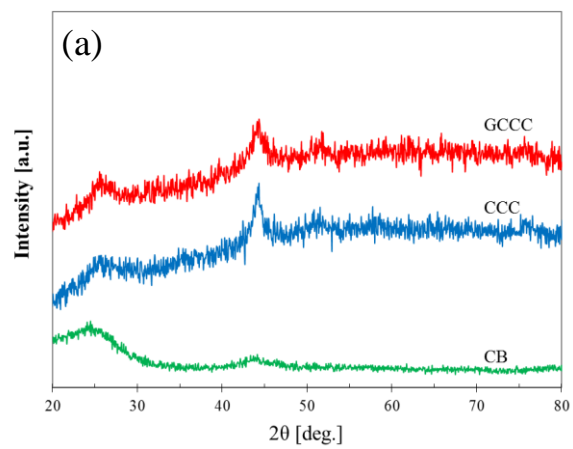


Figure 5.3 (a) Comparison of (a) XRD patterns of GCCC, CCC and CB. Raman spectra of (b) CCC and (c) GCCC.

The HR-TEM images of CB, CCC and GCCC are shown in Figure 5.4 (a), (b) and (c), respectively. The apparent difference between them is the presence of Co particles encapsulated by carbon shells in the CCC and GCCC supports since the Co particles present on the surface are removed during acid leaching. Nanostructured fibers or tubes of graphitic carbon are also formed as a result of pyrolysis in the presence of Co metal [55, 56], while CB showed amorphous morphology without Co particles as shown in Figure 5.4 (a). ICP-AES results of CCC and GCCC indicated a cobalt content of ca. 13 wt% in the supports synthesized at 800 °C.

5.3.2 CO-DOPED Pt/CCC AND CO-DOPED Pt/GCCC CATALYST SYNTHESIS

The elemental compositions in the bulk of Co-doped Pt/CCC and Co-doped Pt/GCCC catalysts were determined using ICP-AES and XRF. For both CCC and GCCC, the Co content is ca. 13 wt%. After Pt deposition, the initial Pt: Co atomic ratios are 1:1 and 0.9:1 for Pt/CCC and Pt/GCCC catalysts, respectively. After heat-treatment at 800 °C for 2 h under 5% H₂, the Pt: Co atomic ratios are 1.1:1 and 1.0:1 for Co-doped Pt/CCC and Co-doped Pt/GCCC catalysts, respectively. As described earlier, the novelty of the process is to use the Co particles embedded in the CCC support for the formation of Co-doped Pt catalyst when subjected to heat-treatment at 800 °C for 2 h under 5% H₂.

To confirm Co doping into Pt, XRD analysis was performed and the results of Pt/CCC, and Pt/GCCC Co-doped Pt/CCC, and Co-doped Pt/GCCC catalysts are shown in Figure 5.5. The characteristic diffraction peaks of Pt/CCC and Pt/GCCC at 39.8, 46.25, and 67.7° correspond to the (111), (200), and (220) planes of pure Pt, respectively, while those at 44.2, 51.5, and 75.8° are ascribed to (111), (200), and (220) planes of pure Co,

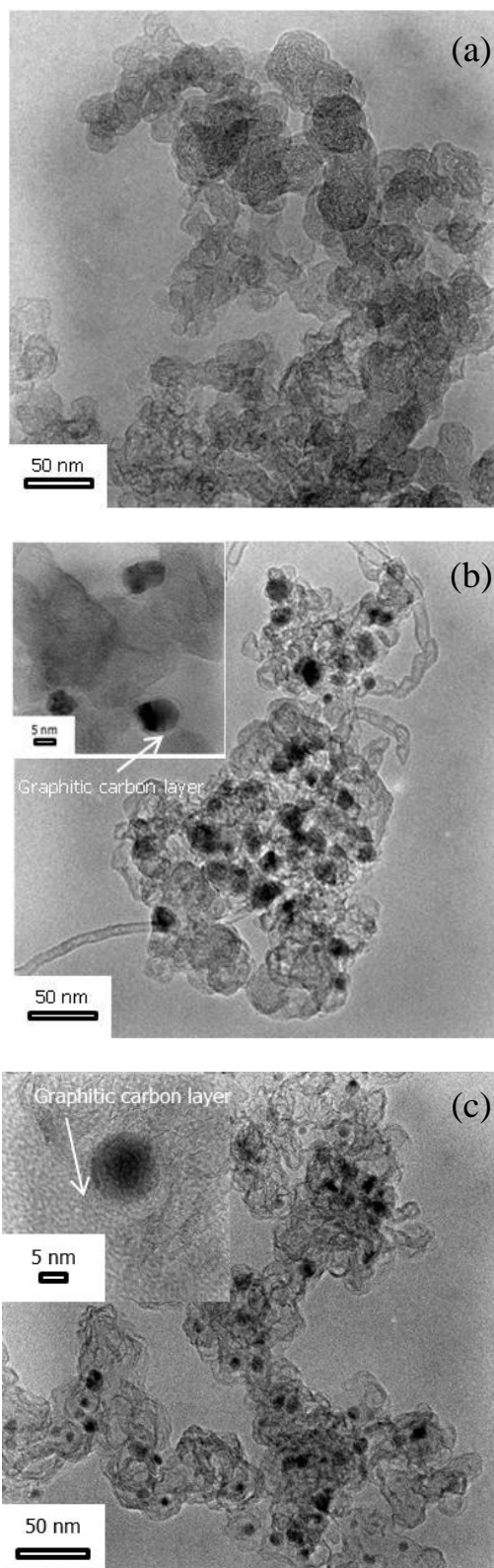


Figure 5.4 HR-TEM images of (a) CB, (b) CCC and (c) GCCC

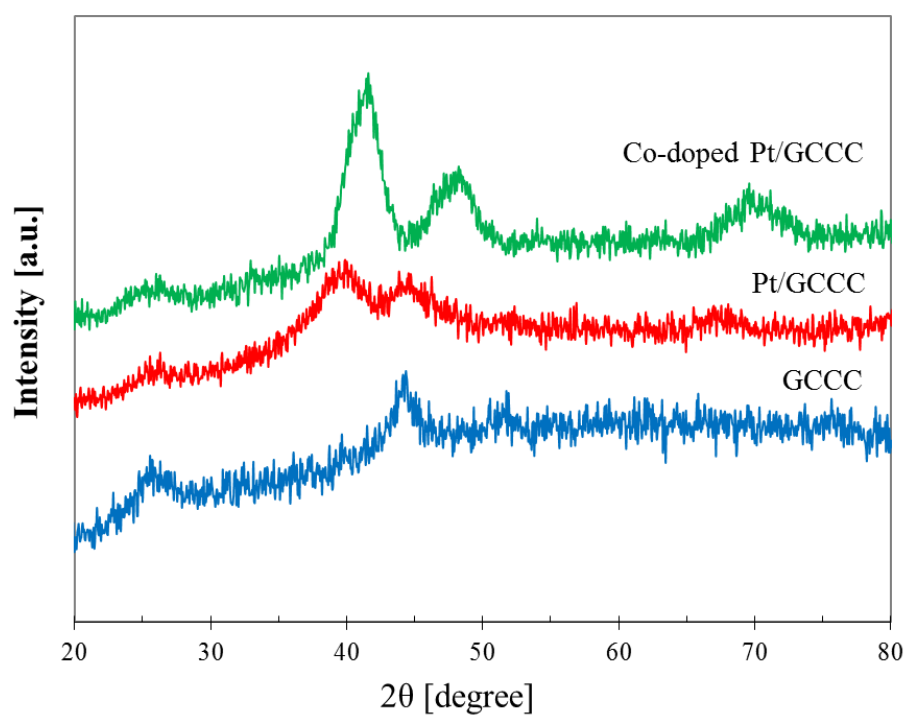


Figure 5.5 XRD patterns of GCCC, Pt/GCCC, and Co-doped Pt/GCCC.

respectively. Both Pt/CCC and Pt/GCCC exhibit the characteristics of the Pt with FCC structure. As shown in Figure 5.5, the characteristic peaks of pure Co are observed in Pt/CCC and Pt/GCCC, since the CCC and GCCC contain Co encapsulated with thin carbon layer. After the heat-treatment, the peaks of Co and Pt are shifted to lower and higher angles, respectively and Co doping into the Pt lattice is observed as indicated by the shift in Pt(111) peak to higher angles. As a result, both Co-doped Pt/CCC and Co-doped Pt/GCCC show chemically ordered FCT. The (001) and (100) superlattice planes at ca. 24 and 33°, respectively, confirm the formation of the FCT phase [127]. The XRD result indicates that the Co particles embedded in the CCC and GCCC supports successfully diffused to the surface during heat-treatment and formed Co-doped Pt catalyst particles regardless of the specific surface area.

Figure 5.6 (a), (b), (c), and (d) show the HR-TEM images of Pt/CCC, Pt/GCCC, Co-doped Pt/CCC, and Co-doped Pt/GCCC catalysts, respectively. Over 100 nanoparticles are used to measure the mean particle size and particle size distribution of the synthesized catalysts. As shown in the micrographs, Pt nanoparticles are uniformly deposited and well-distributed on the supports. The mean particle sizes of Pt/CCC, Pt/GCCC, Co-doped Pt/CCC and Co-doped Pt/GCCC are 2.5, 2.4, 5.4, and 4.8 nm, respectively. Pt nanoparticles in Pt/CCC and Pt/GCCC are dominantly deposited on both CCC and GCCC supports in the range of 2-3 nm. Majority of particles in Co-doped Pt/CCC and Co-doped Pt/GCCC are in the range of the 3-6 nm, while a few large particles are observed but well-distributed on the supports even after high temperature treatment. Parameters like particle size and surface area are summarized in Table 5.1.

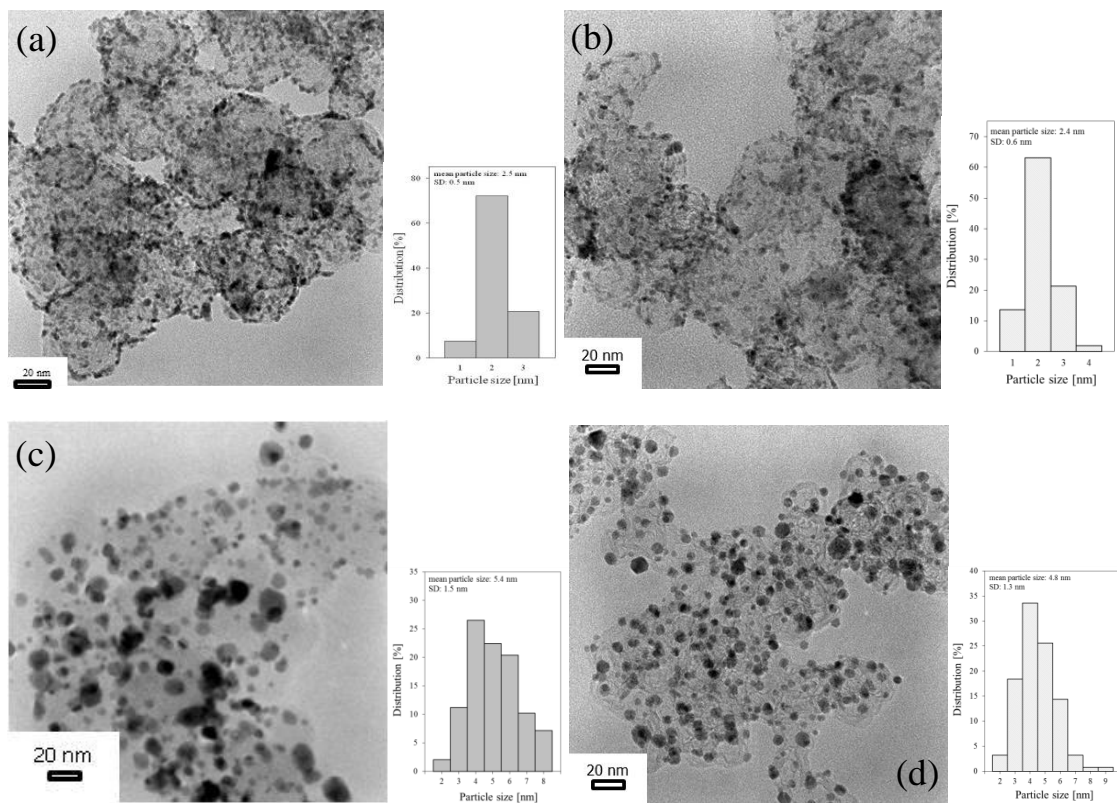


Figure 5.6 HR-TEM images of fresh (a) Pt/CCC, (b) Pt/GCCC, (c) Co-doped Pt/CCC, and (d) Co-doped Pt/GCCC catalysts.

Table 5.1 Characteristics of Co-doped Pt/CCC, Pt/GCCC and Co-doped Pt/GCCC

	$D_{\text{TEM}}^{\text{a}}$ [nm]	$D_{\text{XRD}}^{\text{b}}$ [nm]	$S_{\text{TEM}}^{\text{c}}$ [m ² /g]	ECSA ^d [m ² /gPt]
Co-doped Pt/CCC	5.4	4.1	52	70
Co-doped Pt/GCCC	4.8	3.1	58	57

^a Mean particle size calculated from Scherrer equation.

^b Mean particle size based on the HR-TEM

^c Specific surface area calculated from the diameter of HR-TEM

^d Initial values of ECSA calculated from the hydrogen desorption peak in each CV.

5.3.3 DURABILITY OF CO-DOPED Pt/CCC AND CO-DOPED Pt/GCCC

Figure 5.7 (a) and (b) represent the polarization and power density curves of Co-doped Pt/CCC and Co-doped Pt/GCCC before and after potential cycling between 1.0 and 1.5 V, respectively. In Figure 5.7 (a), the polarization curves of Co-doped Pt/CCC are compared to those of Co-doped Pt/GCCC. At $0.6 V_{iR-free}$, the initial current density of Co-doped Pt/CCC shows 1395 mA cm^{-2} , while the current density after 1000 cycles (between 1.0 and 1.5 V) exhibits 400 mA cm^{-2} . Moreover, at 1200 mA cm^{-2} , the initial potential is $0.638 V_{iR-free}$ and no activity is observed after 1000 cycles, which indicates that the Co-doped Pt/CCC catalyst layer is totally destroyed when subjected to high potentials. This result is very similar with the Pt/C. at $0.6 V_{iR-free}$, initially the Pt/C shows the 1230 mA cm^{-2} , while the current density after 1000 cycles exhibits 360 mA cm^{-2} . The Pt/C loses all the activity at 1200 mA cm^{-2} after 1000 cycles. In the case of Co-doped Pt/GCCC, the initial current density is 1154 mA cm^{-2} at $0.6 V_{iR-free}$, while the current density after 3,000 cycles shows 1140 mA cm^{-2} . Also, the potential loss at 1200 mA cm^{-2} is only $10 \text{ mV}_{iR-free}$ after 3,000 cycles. The durability of Co-doped Pt/GCCC is remarkably enhanced when compared to that of Co-doped Pt/CCC catalyst. As shown in Figure 5.7 (b), for the maximum power density which is calculated using the iR -free cell potential, both catalysts initially show similar values. The maximum power density of Co-doped Pt/GCCC is 897 mW cm^{-2} , while that of Co-doped Pt/CCC is 883 mW cm^{-2} . After 1000 cycles, the maximum power density of Co-doped Pt/CCC decreased to 239 mW cm^{-2} corresponding to 73% loss. However, that maximum power density of Co-doped Pt/GCCC decreased to 707 mW cm^{-2} which corresponds to only 21% loss after 1,000 cycles.

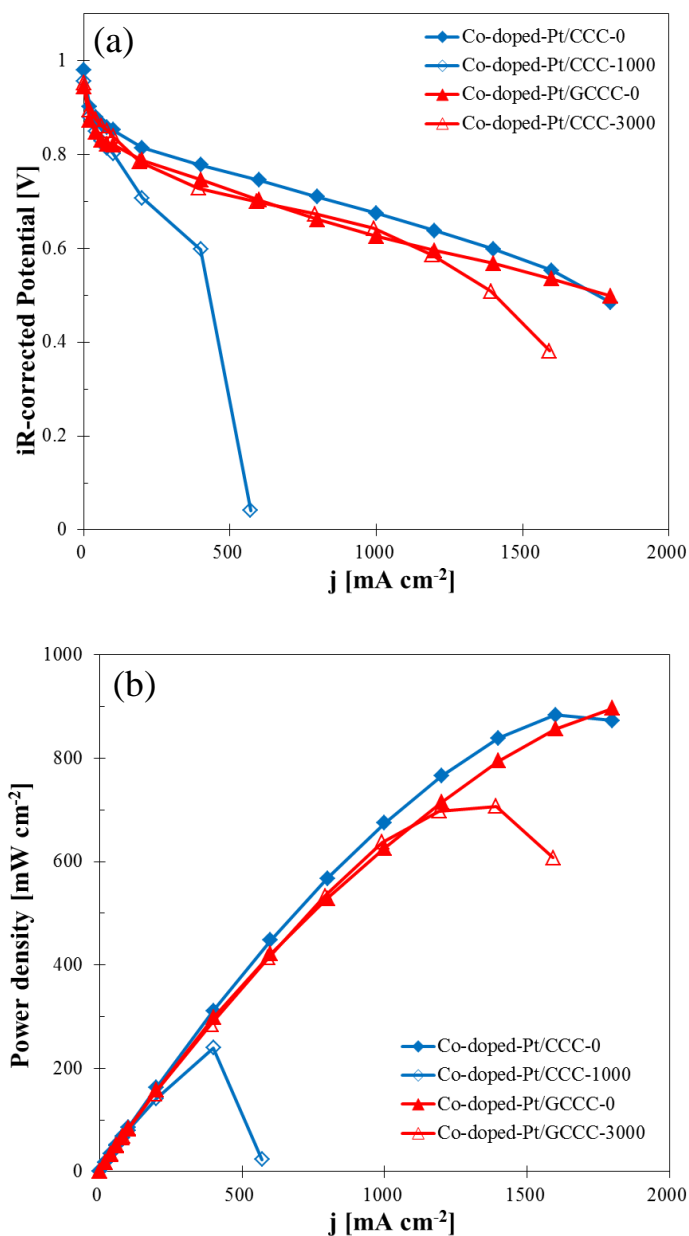


Figure 5.7 (a) H_2 /air polarization and (b) power density curves of Co-doped Pt/CCC and Co-doped Pt/GCCC before and after potential cycling (1,000 cycles for Co-doped Pt/CCC; 3,000 cycles for Co-doped Pt/GCCC) between 1.0 and 1.5 V, respectively.

To further analyze the durability of catalysts, the normalized ECSAs calculated for Co-doped Pt/CCC, Co-doped Pt/GCCC, and Pt/C catalysts as a function of cycle number are shown in Figure 5.8. Initial ECSA values of 70, 57, and 70.8 m² g_{Pt}⁻¹ are measured for Co-doped Pt/CCC, Co-doped Pt/GCCC, and Pt/C catalysts, respectively. After 1000 cycles, only 38 and 39% ECSA remains for the Co-doped Pt/CCC and Pt/C, respectively, while Co-doped Pt/GCCC catalyst retains 69% and 39% of its initial ECSA after 1,000 and 3,000 cycles, respectively. These results indicate that the Co-doped Pt/GCCC is remarkably durable when compared to the Co-doped Pt/CCC catalyst.

The composition of catalysts before and after AST was examined using XRF. The results indicated that the initial Pt:Co atomic ratio for the initial Co-doped Pt/CCC and Co-doped Pt/GCCC is almost constant after 1,000 and 3000 cycles, respectively. In the previous study (chapter 3), the potential cycling from 0.6 to 1.0 V led to Co leaching and the formation of Pt-enriched shell/PtCo core structure. However, the potential cycling from 1.0 and 1.5 V does not result in Co leaching despite the performance degradation. It may be suggested that the electrochemical leaching of Co is inhibited at the high potential due to the rapid formation of up to 2 MLs of Pt oxide on the surface [181, 182]. The compositional data is summarized in Table 5.2.

XRD patterns and their deconvolution before and after AST study are shown in Figure 5.9 and 5.10. The deconvolution is carried out in the range of 37 to 44°. First, the superlattice peaks like (100) plane, which is a feature for the FCT structure, are disappeared after 1000 cycles in Figure 5.9 (a). The (101) plane of Co-doped Pt after 1000 cycles is shifted to lower angle indicating the increment of lattice parameter. In Figure 5.9 (b), the initial Co-doped Pt/CCC catalyst clearly shows single peak, while the

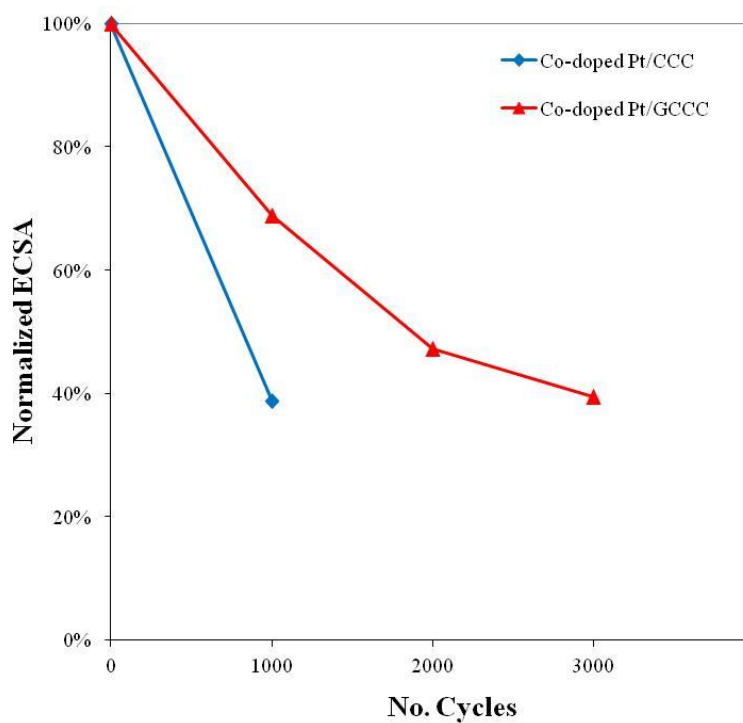


Figure 5.8 Normalized ECSA of Co-doped Pt/CCC and Co-doped Pt/GCCC catalysts as a function of cycle number. ECSAs were calculated from cyclic voltammograms obtained between 0.05 and 0.6 V (vs. RHE) at 80 °C. Fully humidified H₂ (200 sccm) and N₂ (75 sccm) were supplied to the anode and the cathode, respectively.

Table 5.2 Compositions of Pt/CCC, Co-doped Pt/CCC, Pt/GCCC and Co-doped Pt/GCCC measured by ICP-AES, XPS, and XRF

	ICP	XPS	XRF	
			Initial	After AST
Pt/CCC	1:1	-	-	-
Pt/GCCC	0.9:1	-	-	-
Co-doped Pt/CCC	1.1:1	1.2:1	1.1:1	1:1
Co-doped Pt/GCCC	1.0:1	1.5:1	1.0:1	0.9:1

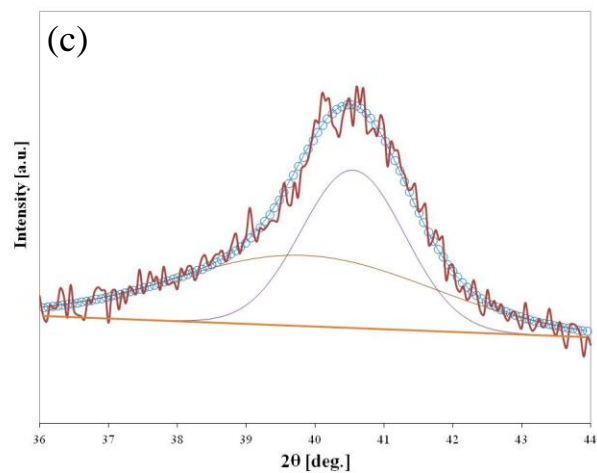
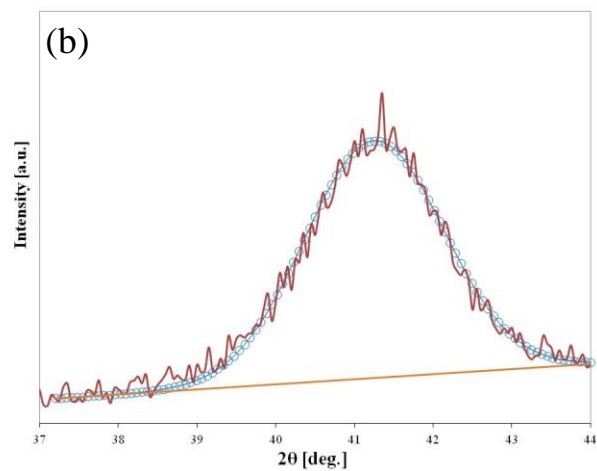
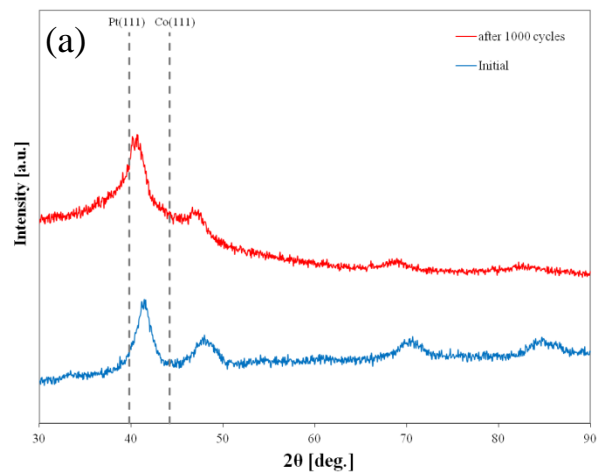


Figure 5.9 (a) Comparison of XRD patterns of Co-doped Pt/CCC before and after 1,000 cycles. Deconvoluted patterns of Co-doped Pt/CCC (b) before and (c) after 1,000 cycles.

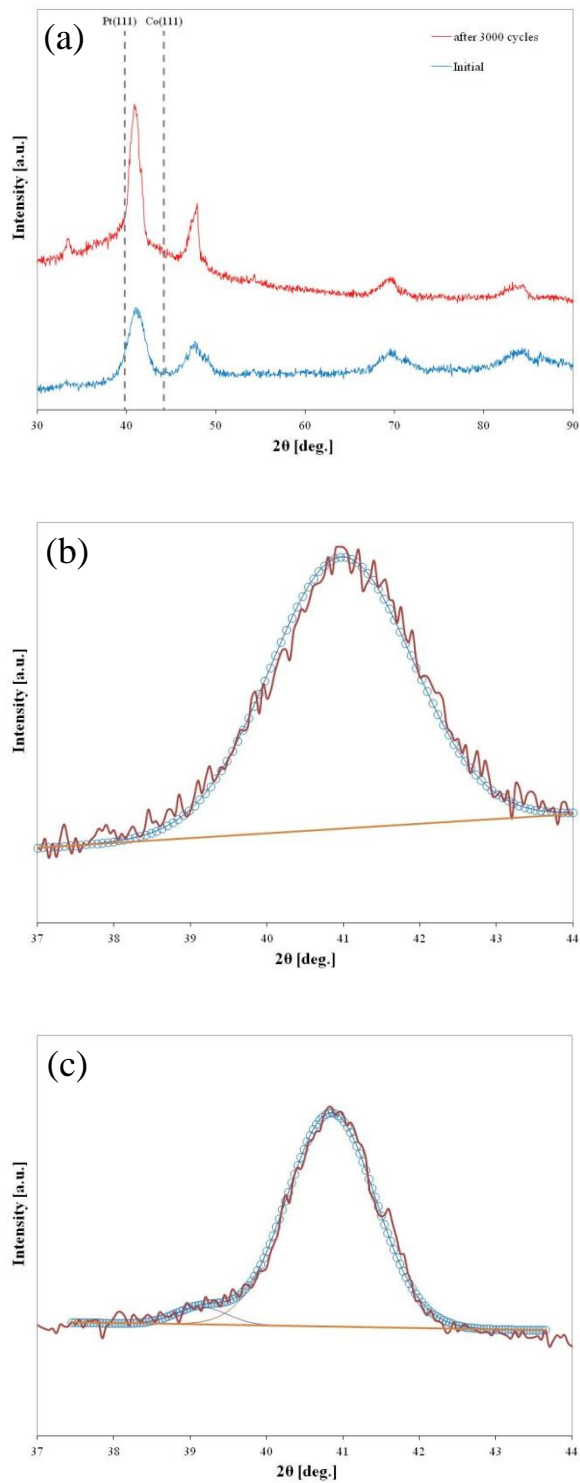


Figure 5.10 (a) Comparison of XRD patterns of Co-doped Pt/GCCC before and after 3,000 cycles. Deconvoluted patterns of Co-doped Pt/GCCC (b) before and (c) after 3,000 cycles.

Table 5.3 Characteristics of XRD peak for Co-doped Pt/CCC and Co-doped Pt/GCCC after AST

	Catalyst phase	Initial			After 3,000 cycles		
		2 θ	FWHM	Ratio [%]	2 θ	FWHM	Ratio [%]
Co-doped Pt/CCC	Pt	-	-	-	39.84	4.373	51.6
	PtCo	41.25	2.082	100	40.55	1.767	48.4
Co-doped Pt/GCCC	Pt	-	-	-	39.15	0.793	4.5
	PtCo	40.97	2.193	100	40.85	1.361	95.5

catalyst after 1000 cycles in Figure 5.9 (c) exhibits the 2 different peaks at 39.84 and 40.55° with the relative ratios of 51.6 and 48.4%, respectively. These changes indicate that the FCC crystalline structure (PDF#97-010-2621) formation for the Co-doped Pt/CCC catalyst after AST. Similarly, as shown in Figure 5.10 (a), the initial (101) plane of Co-doped Pt/CCC is moved to lower angle, which results in increased lattice parameters, while the XRD patterns of Co-doped Pt/GCCC show the super lattice peaks before and after 3000 cycles. The characteristic peaks of Co-doped Pt/GCCC after 3000 cycles correspond to the FCT structure (PDF#97-010-2622). In Figure 5.10 (b), the initial Co-doped Pt/GCCC catalyst also apparently represents a single peak in the range of 37 to 44°, while the catalyst after 3000 cycles in Figure 5.10 (c) shows two different peaks at 39.15 and 40.85° with relative ratios of 4.5 and 95.5%, respectively. Post-test XRD analyses indicated that the structure of Co-doped Pt/GCCC is more stable than that of Co-doped Pt/CCC after AST.

Fundamentally, the interactions of Pt and carbon are partially covalent and ionic since the electron delocalization between the π sites on carbon and d orbital of Pt, and the electron-transfer from Pt to carbon, respectively [30, 140, 168, 183-186]. Unlike the amorphous carbons, the highly graphitized carbon supports, such as CNTs and graphenes, have abundant π sites on the surface and relatively small number of edge plane sites, which is resistant for carbon oxidation [168, 183, 184]. Therefore, the interaction of graphitized carbon and Pt is stronger than that of amorphous carbon and Pt, which leads to the less degradation. On the other hand, the tetragonal to cubic shift is occurred by increasing the particle size [187-189]. The particle size effects are based on a core-shell model of nanoparticles where the core is tetragonal and the shell is cubic. As reported in

the literature [7-10], Pt has been dissolved and re-deposited on the catalyst surface under high potential cycling. As a result, the particle size increases and the homogeneous bimetallic catalyst transforms into a Pt-alloy core and Pt shell [150, 190]. These combined effects can help the structure of catalyst on the highly graphitized GCCC to be stable after the AST which resulted in the stable fuel cell performance as shown in Figure 5.7.

5.4 CONCLUSION

In this study, Co-Doped Pt/GCCC catalyst was prepared using a graphitized CB as a support and compared to Co-doped Pt/CCC catalyst. The change of specific surface area, interlayer spacing, and I_D/I_G value indicated that the GCCC was more graphitized than the CCC support. XPS results indicated the presence of four different types of nitrogen. The ratio of quaternary-N related to the durability is particularly increased as compared to that in the Co-doped Pt/CCC. HR-TEM studies indicated uniform particle sizes for Co-doped Pt/CCC and Co-doped Pt/GCCC catalysts with an average size of ca. 5 nm. Both Co-doped Pt/CCC and Co-doped Pt/GCCC catalysts showed similar initial power density. After 3,000 potential cycles between 1.0 and 1.5 V, the retained ECSA of Co-doped Pt/GCCC was 39%. Furthermore, a very stable H₂/air fuel cell performance was observed at 0.6 V_{iR-free} for the Co-doped Pt/GCCC catalyst. According to the post-test XRD results, FCT-structure of Co-doped Pt/GCCC was maintained until 3,000 potential cycles, while the intrinsic FCT peaks of Co-doped Pt/CCC disappeared after 1,000 potential cycles. Also, the 2θ of Co-doped Pt/GCCC was almost constant, while that of Co-doped Pt/CCC was apparently shifted to lower angle. Consequently, the

electrochemical and structural studies indicated that the degree of graphitization plays an important role in the stability of the catalyst structure under high potential cycling (1.0–1.5 V).

CHAPTER 6

SUMMARY

In this study, a novel non-precious metal CCC containing electrochemically active sites for ORR was prepared and a novel synthesis of the Co-doped Pt/CCC is developed with the CCC.

A novel CCC exhibits high activity and good selectivity for ORR since the presence of pyridinic and quaternary-nitrogen catalytic sites observed by XPS analysis. The synergistic effect of CCC and Pt resulted in 1.5 to 6-fold higher activity than conventional Pt/C in RDE and fuel cell testing. The XPS analysis confirmed that the enhancement originated from the CCC and increase of metallic Pt⁰.

A novel synthesis of the Co-doped Pt/CCC using an electrochemically active CCC is developed through platinum deposition and heat-treatment procedures. HR-TEM images indicated uniform Pt deposition for the Co-doped Pt/CCC with average particle size of 5.4 nm. Co-doped Pt/CCC showed high initial mass activity of 0.44 A mg_{Pt}⁻¹ and 0.25 A mg_{Pt}⁻¹ at 0.9 V_{iR-free} after 30,000 potential cycles between 0.6 and 1.0 V. It is highly stable as compared to the conventional catalysts (PtCo/C-Imp, PtCo/C, and Pt/C) showing 60-70% loss of activity. The enhanced catalytic activity and stability of activity for Co-doped Pt/CCC are attributed to the formation of compressive Pt lattice due to Co doping. The electrochemical characterization indicated that Co doping increased the

potential for Pt oxide formation to a more positive value and suppressed the detrimental Pt dissolution process.

To develop the stable support, the change in carbon nanostructure by means of high temperature treatment is investigated. The physical characterization such as BET, XRD, and Raman spectroscopy indicated that the degree of graphitization is increased as compared to the amorphous pristine carbon black. And the electrochemical tests exhibit the increased corrosion resistance as compared to the amorphous pristine carbon black. To apply for the novel synthesis of Co-doped Pt catalysts, GCCC was prepared using this graphitized CB as a support. As expected, the physical characterization indicated that GCCC exhibited higher degree of graphitization than CCC. HR-TEM studies showed uniform particle sizes for Co-doped Pt/GCCC while the XPS analysis exhibited the presence of higher ratio of quaternary-nitrogen in GCCC than CCC. Therefore, the stability of Co-doped Pt/GCCC based on fuel cell performance and ECSA is significantly increased as compared to the Co-doped Pt/CCC. According to the post-test XRD results, FCT-structure of Co-doped Pt/GCCC was maintained until 3,000 potential cycles, while the intrinsic FCT peaks of Co-doped Pt/CCC disappeared after 1,000 potential cycles.

REFERENCES

- [1] http://www.g-energy.com.my/fuel_cell_tech_PEMFC.html.
- [2] http://energy.gov/sites/prod/files/2014/03/f11/apu2011_10_papageorgopoulos.pdf.
- [3] http://www.hydrogen.energy.gov/pdfs/epact_report_sec811.pdf.
- [4] http://energy.gov/sites/prod/files/14012_fuel_cell_system_cost_2013.pdf.
- [5] M. Pourbaix, Atlas of Electrochemical Equilibrium in Aqueous Solutions, 1st ed ed., Pergamon Press, New York, 1966.
- [6] V.A.T. Dam, F.A. de Bruijn, The Stability of PEMFC Electrodes: Platinum Dissolution vs Potential and Temperature Investigated by Quartz Crystal Microbalance, Journal of The Electrochemical Society, 154 (2007) B494-B499.
- [7] D.C. Johnson, D.T. Napp, S. Bruckenstein, A ring-disk electrode study of the current/potential behaviour of platinum in 1.0 M sulphuric and 0.1 M perchloric acids, Electrochimica Acta, 15 (1970) 1493-1509.
- [8] K. Kinoshita, J.T. Lundquist, P. Stonehart, Potential cycling effects on platinum electrocatalyst surfaces, Journal of Electroanalytical Chemistry and Interfacial Electrochemistry, 48 (1973) 157-166.
- [9] D.A.J. Rand, R. Woods, A study of the dissolution of platinum, palladium, rhodium and gold electrodes in 1 m sulphuric acid by cyclic voltammetry, Journal of Electroanalytical Chemistry and Interfacial Electrochemistry, 35 (1972) 209-218.
- [10] X. Wang, R. Kumar, D.J. Myers, Effect of Voltage on Platinum Dissolution: Relevance to Polymer Electrolyte Fuel Cells, Electrochemical and Solid-State Letters, 9 (2006) A225-A227.
- [11] Y. Sugawara, T. Okayasu, A.P. Yadav, A. Nishikata, T. Tsuru, Dissolution Mechanism of Platinum in Sulfuric Acid Solution, Journal of The Electrochemical Society, 159 (2012) F779-F786.

- [12] A.A. Topalov, S. Cherevko, A.R. Zeradjanin, J.C. Meier, I. Katsounaros, K.J.J. Mayrhofer, Towards a comprehensive understanding of platinum dissolution in acidic media, *Chemical Science*, 5 (2014) 631-638.
- [13] S.R. Dhanushkodi, S. Kundu, M.W. Fowler, M.D. Pritzker, Study of the effect of temperature on Pt dissolution in polymer electrolyte membrane fuel cells via accelerated stress tests, *Journal of Power Sources*, 245 (2014) 1035-1045.
- [14] J. Xie, D.L. Wood, D.M. Wayne, T.A. Zawodzinski, P. Atanassov, R.L. Borup, Durability of PEMFCs at High Humidity Conditions, *Journal of The Electrochemical Society*, 152 (2005) A104-A113.
- [15] Y. Hoshi, T. Yoshida, A. Nishikata, T. Tsuru, Dissolution of Pt–M (M: Cu, Co, Ni, Fe) binary alloys in sulfuric acid solution, *Electrochimica Acta*, 56 (2011) 5302-5309.
- [16] Y. Hoshi, E. Tada, A. Nishikata, T. Tsuru, Effect of potential cycling on dissolution of equimolar Pt–M (M: Co, Ni, Fe) alloys in sulfuric acid solution, *Electrochimica Acta*, 85 (2012) 268-272.
- [17] P. Yu, M. Pemberton, P. Plasse, PtCo/C cathode catalyst for improved durability in PEMFCs, *Journal of Power Sources*, 144 (2005) 11-20.
- [18] P.J. Ferreira, G.J. la O', Y. Shao-Horn, D. Morgan, R. Makharia, S. Kocha, H.A. Gasteiger, Instability of Pt/C Electrocatalysts in Proton Exchange Membrane Fuel Cells: A Mechanistic Investigation, *Journal of The Electrochemical Society*, 152 (2005) A2256-A2271.
- [19] A. Bonakdarpour, J. Wenzel, D.A. Stevens, S. Sheng, T.L. Monchesky, R. Löbel, R.T. Atanasoski, A.K. Schmoedel, G.D. Vernstrom, M.K. Debe, J.R. Dahn, Studies of Transition Metal Dissolution from Combinatorially Sputtered, Nanostructured Pt_{1-x}M_x (M = Fe, Ni; 0 < x < 1) Electrocatalysts for PEM Fuel Cells, *Journal of The Electrochemical Society*, 152 (2005) A61-A72.
- [20] A. Haug, L. Protsailo, Alternative Catalysts for PEM FCs: Performance and Durability at Normal and High Temperature Operations, Meeting Abstracts, MA2005-02 (2006) 1023.
- [21] D. Thompsett, in: W. Vielstich, H. Gasteiger, A. Lamm (Eds.), *Handbook of Fuel Cells—Fundamentals, Technology and Applications*, vol. 3, Wiley, Chichester, UK, 2003, pp. 467 (chap. 37).
- [22] T.R. Ralph, J.E. Keating, N.J. Collis, T.I. Hyde, ETSU Contract Report F/02/00038, 1997.

- [23] F.A. de Bruijn, V.A.T. Dam, G.J.M. Janssen, Review: Durability and Degradation Issues of PEM Fuel Cell Components, *Fuel Cells*, 8 (2008) 3-22.
- [24] P.T. Yu, W. Gu, R. Makharia, F.T. Wagner, H.A. Gasteiger, The Impact of Carbon Stability on PEM Fuel Cell Startup and Shutdown Voltage Degradation, *ECS Transactions*, 3 (2006) 797-809.
- [25] K. Kinoshita, *Carbon: Electrochemical and Physicochemical Properties*, Wiley, New York, 1988.
- [26] D.A. Stevens, J.R. Dahn, Thermal degradation of the support in carbon-supported platinum electrocatalysts for PEM fuel cells, *Carbon*, 43 (2005) 179-188.
- [27] L.M. Roen, C.H. Paik, T.D. Jarvi, Electrocatalytic Corrosion of Carbon Support in PEMFC Cathodes, *Electrochemical and Solid-State Letters*, 7 (2004) A19-A22.
- [28] D.A. Stevens, M.T. Hicks, G.M. Haugen, J.R. Dahn, Ex Situ and In Situ Stability Studies of PEMFC Catalysts: Effect of Carbon Type and Humidification on Degradation of the Carbon, *Journal of The Electrochemical Society*, 152 (2005) A2309-A2315.
- [29] M. Cai, M.S. Ruthkosky, B. Merzougui, S. Swathirajan, M.P. Balogh, S.H. Oh, Investigation of thermal and electrochemical degradation of fuel cell catalysts, *Journal of Power Sources*, 160 (2006) 977-986.
- [30] M.F. Mathias, R. Makharia, H.A. Gasteiger, J.J. Conley, T.J. Fuller, C.J. Gittleman, S.S. Kocha, D.P. Miller, C.K. Mittelsteadt, T. Xie, S.G. Yan, P.T. Yu, Two Fuel Cell Cars in Every Garage?, *The Electrochemical Society Interface*, 14 (2005) 24.
- [31] C.A. Reiser, L. Bregoli, T.W. Patterson, J.S. Yi, J.D. Yang, M.L. Perry, T.D. Jarvi, A Reverse-Current Decay Mechanism for Fuel Cells, *Electrochemical and Solid-State Letters*, 8 (2005) A273-A276.
- [32] M. Oszcipok, M. Zedda, D. Riemann, D. Geckeler, Low temperature operation and influence parameters on the cold start ability of portable PEMFCs, *Journal of Power Sources*, 154 (2006) 404-411.
- [33] T.F. Fuller, J. Newman, Water and Thermal Management in Solid-Polymer-Electrolyte Fuel Cells, *Journal of The Electrochemical Society*, 140 (1993) 1218-1225.
- [34] T.W. Patterson, R.M. Darling, Damage to the Cathode Catalyst of a PEM Fuel Cell Caused by Localized Fuel Starvation, *Electrochemical and Solid-State Letters*, 9 (2006) A183-A185.

- [35] H. Tang, Z. Qi, M. Ramani, J.F. Elter, PEM fuel cell cathode carbon corrosion due to the formation of air/fuel boundary at the anode, *Journal of Power Sources*, 158 (2006) 1306-1312.
- [36] J. Willsau, J. Heitbaum, The influence of Pt-activation on the corrosion of carbon in gas diffusion electrodes—A dems study, *Journal of Electroanalytical Chemistry and Interfacial Electrochemistry*, 161 (1984) 93-101.
- [37] K.H. Kangasniemi, D.A. Condit, T.D. Jarvi, Characterization of Vulcan Electrochemically Oxidized under Simulated PEM Fuel Cell Conditions, *Journal of The Electrochemical Society*, 151 (2004) E125-E132.
- [38] Z. Siroma, K. Ishii, K. Yasuda, Y. Miyazaki, M. Inaba, A. Tasaka, Imaging of highly oriented pyrolytic graphite corrosion accelerated by Pt particles, *Electrochemistry Communications*, 7 (2005) 1153-1156.
- [39] T. Kinumoto, K. Takai, Y. Iriyama, T. Abe, M. Inaba, Z. Ogumi, Stability of Pt-Catalyzed Highly Oriented Pyrolytic Graphite Against Hydrogen Peroxide in Acid Solution, *Journal of The Electrochemical Society*, 153 (2006) A58-A63.
- [40] A.M. Chaparro, N. Mueller, C. Atienza, L. Daza, Study of electrochemical instabilities of PEMFC electrodes in aqueous solution by means of membrane inlet mass spectrometry, *Journal of Electroanalytical Chemistry*, 591 (2006) 69-73.
- [41] X. Wang, W. Li, Z. Chen, M. Waje, Y. Yan, Durability investigation of carbon nanotube as catalyst support for proton exchange membrane fuel cell, *Journal of Power Sources*, 158 (2006) 154-159.
- [42] C.-C. Hung, P.-Y. Lim, J.-R. Chen, H.C. Shih, Corrosion of carbon support for PEM fuel cells by electrochemical quartz crystal microbalance, *Journal of Power Sources*, 196 (2011) 140-146.
- [43] B. Avasarala, R. Moore, P. Haldar, Surface oxidation of carbon supports due to potential cycling under PEM fuel cell conditions, *Electrochimica Acta*, 55 (2010) 4765-4771.
- [44] S. Maass, F. Finsterwalder, G. Frank, R. Hartmann, C. Merten, Carbon support oxidation in PEM fuel cell cathodes, *Journal of Power Sources*, 176 (2008) 444-451.
- [45] R. Jasinski, A New Fuel Cell Cathode Catalyst, *Nature*, 201 (1964) 1212-1213.
- [46] S. Gupta, D. Tryk, I. Bae, W. Aldred, E. Yeager, Heat-treated polyacrylonitrile-based catalysts for oxygen electroreduction, *J Appl Electrochem*, 19 (1989) 19-27.

- [47] M. Lefèvre, E. Proietti, F. Jaouen, J.-P. Dodelet, Iron-Based Catalysts with Improved Oxygen Reduction Activity in Polymer Electrolyte Fuel Cells, *Science*, 324 (2009) 71-74.
- [48] M. Lefèvre, J.-P. Dodelet, Fe-based catalysts for the reduction of oxygen in polymer electrolyte membrane fuel cell conditions: determination of the amount of peroxide released during electroreduction and its influence on the stability of the catalysts, *Electrochimica Acta*, 48 (2003) 2749-2760.
- [49] J. Maruyama, I. Abe, Formation of Platinum-Free Fuel Cell Cathode Catalyst with Highly Developed Nanospace by Carbonizing Catalase, *Chemistry of Materials*, 17 (2005) 4660-4667.
- [50] H. Schulenburg, S. Stankov, V. Schünemann, J. Radnik, I. Dorbandt, S. Fiechter, P. Bogdanoff, H. Tributsch, Catalysts for the Oxygen Reduction from Heat-Treated Iron(III) Tetramethoxyphenylporphyrin Chloride: Structure and Stability of Active Sites, *The Journal of Physical Chemistry B*, 107 (2003) 9034-9041.
- [51] N.P. Subramanian, S.P. Kumaraguru, H. Colon-Mercado, H. Kim, B.N. Popov, T. Black, D.A. Chen, Studies on Co-based catalysts supported on modified carbon substrates for PEMFC cathodes, *Journal of Power Sources*, 157 (2006) 56-63.
- [52] V. Nallathambi, J.-W. Lee, S.P. Kumaraguru, G. Wu, B.N. Popov, Development of high performance carbon composite catalyst for oxygen reduction reaction in PEM Proton Exchange Membrane fuel cells, *Journal of Power Sources*, 183 (2008) 34-42.
- [53] N.P. Subramanian, X. Li, V. Nallathambi, S.P. Kumaraguru, H. Colon-Mercado, G. Wu, J.-W. Lee, B.N. Popov, Nitrogen-modified carbon-based catalysts for oxygen reduction reaction in polymer electrolyte membrane fuel cells, *Journal of Power Sources*, 188 (2009) 38-44.
- [54] K. Wiesener, N4-chelates as electrocatalyst for cathodic oxygen reduction, *Electrochimica Acta*, 31 (1986) 1073-1078.
- [55] P.H. Matter, L. Zhang, U.S. Ozkan, The role of nanostructure in nitrogen-containing carbon catalysts for the oxygen reduction reaction, *Journal of Catalysis*, 239 (2006) 83-96.
- [56] S. Maldonado, K.J. Stevenson, Influence of Nitrogen Doping on Oxygen Reduction Electrocatalysis at Carbon Nanofiber Electrodes, *The Journal of Physical Chemistry B*, 109 (2005) 4707-4716.
- [57] K.A. Kurak, A.B. Anderson, Nitrogen-Treated Graphite and Oxygen Electroreduction on Pyridinic Edge Sites, *The Journal of Physical Chemistry C*, 113 (2009) 6730-6734.

- [58] S. Kundu, T.C. Nagaiah, W. Xia, Y. Wang, S.V. Dommele, J.H. Bitter, M. Santa, G. Grundmeier, M. Bron, W. Schuhmann, M. Muhler, Electrocatalytic Activity and Stability of Nitrogen-Containing Carbon Nanotubes in the Oxygen Reduction Reaction, *The Journal of Physical Chemistry C*, 113 (2009) 14302-14310.
- [59] V. Nallathambi, G. Wu, N. Subramanian, S. Kumaraguru, J.-W. Lee, B. Popov, Highly Active Carbon Composite Electrocatalysts for PEM Fuel Cells, *ECS Transactions*, 11 (2007) 241-247.
- [60] G. Liu, X. Li, P. Ganesan, B.N. Popov, Development of non-precious metal oxygen-reduction catalysts for PEM fuel cells based on N-doped ordered porous carbon, *Applied Catalysis B: Environmental*, 93 (2009) 156-165.
- [61] G. Liu, X. Li, P. Ganesan, B.N. Popov, Studies of oxygen reduction reaction active sites and stability of nitrogen-modified carbon composite catalysts for PEM fuel cells, *Electrochimica Acta*, 55 (2010) 2853-2858.
- [62] G. Lalande, R. Côté, G. Tamizhmani, D. Guay, J.P. Dodelet, L. Dignard-Bailey, L.T. Weng, P. Bertrand, Physical, chemical and electrochemical characterization of heat-treated tetracarboxylic cobalt phthalocyanine adsorbed on carbon black as electrocatalyst for oxygen reduction in polymer electrolyte fuel cells, *Electrochimica Acta*, 40 (1995) 2635-2646.
- [63] B.N. Popov, X. Li, G. Liu, J.-W. Lee, Power source research at USC: Development of advanced electrocatalysts for polymer electrolyte membrane fuel cells, *International Journal of Hydrogen Energy*, 36 (2011) 1794-1802.
- [64] S.L. Gojković, S. Gupta, R.F. Savinell, Heat-treated iron(III) tetramethoxyphenyl porphyrin chloride supported on high-area carbon as an electrocatalyst for oxygen reduction:: Part III. Detection of hydrogen-peroxide during oxygen reduction, *Electrochimica Acta*, 45 (1999) 889-897.
- [65] X. Li, G. Liu, B.N. Popov, Activity and stability of non-precious metal catalysts for oxygen reduction in acid and alkaline electrolytes, *Journal of Power Sources*, 195 (2010) 6373-6378.
- [66] A.L. Patterson, The Scherrer Formula for X-Ray Particle Size Determination, *Physical Review*, 56 (1939) 978-982.
- [67] K.S.W. Sing, D.H. Everett, R.A.W. Haul, L. Moscou, R.A. Pierotti, J. Rouquerol, T. Siemieniewska, Reporting Physisorption Data for Gas/Solid Systems, *Handbook of Heterogeneous Catalysis*, vol. Wiley-VCH Verlag GmbH & Co. KGaA2008, (chap.

- [68] Y. Shao, J. Sui, G. Yin, Y. Gao, Nitrogen-doped carbon nanostructures and their composites as catalytic materials for proton exchange membrane fuel cell, *Applied Catalysis B: Environmental*, 79 (2008) 89-99.
- [69] W.Y. Wong, W.R.W. Daud, A.B. Mohamad, A.A.H. Kadhum, E.H. Majlan, K.S. Loh, Nitrogen-containing carbon nanotubes as cathodic catalysts for proton exchange membrane fuel cells, *Diamond and Related Materials*, 22 (2012) 12-22.
- [70] J. Tang, J. Yang, X. Zhou, Acetylene black derived hollow carbon nanostructure and its application in lithium-sulfur batteries, *RSC Advances*, 3 (2013) 16936-16939.
- [71] S. Maass, F. Finsterwalder, G. Frank, R. Hartmann, C. Merten, Carbon support oxidation in PEM fuel cell cathodes, *Journal of Power Sources*, 176 (2008) 444-451.
- [72] S.L. Gojković, S. Gupta, R.F. Savinell, Heat-treated iron(III) tetramethoxyphenyl porphyrin chloride supported on high-area carbon as an electrocatalyst for oxygen reduction: Part II. Kinetics of oxygen reduction, *Journal of Electroanalytical Chemistry*, 462 (1999) 63-72.
- [73] Z. Liu, X. Lin, J.Y. Lee, W. Zhang, M. Han, L.M. Gan, Preparation and Characterization of Platinum-Based Electrocatalysts on Multiwalled Carbon Nanotubes for Proton Exchange Membrane Fuel Cells, *Langmuir*, 18 (2002) 4054-4060.
- [74] F. Su, Z. Tian, C.K. Poh, Z. Wang, S.H. Lim, Z. Liu, J. Lin, Pt Nanoparticles Supported on Nitrogen-Doped Porous Carbon Nanospheres as an Electrocatalyst for Fuel Cells, *Chemistry of Materials*, 22 (2010) 832-839.
- [75] Z. Liu, J.Y. Lee, W. Chen, M. Han, L.M. Gan, Physical and Electrochemical Characterizations of Microwave-Assisted Polyol Preparation of Carbon-Supported PtRu Nanoparticles, *Langmuir*, 20 (2004) 181-187.
- [76] Y. Liang, H. Zhang, H. Zhong, X. Zhu, Z. Tian, D. Xu, B. Yi, Preparation and characterization of carbon-supported PtRuIr catalyst with excellent CO-tolerant performance for proton-exchange membrane fuel cells, *Journal of Catalysis*, 238 (2006) 468-476.
- [77] D.-W. Wang, F. Li, L.-C. Yin, X. Lu, Z.-G. Chen, I.R. Gentle, G.Q. Lu, H.-M. Cheng, Nitrogen-Doped Carbon Monolith for Alkaline Supercapacitors and Understanding Nitrogen-Induced Redox Transitions, *Chemistry – A European Journal*, 18 (2012) 5345-5351.
- [78] A. Pozio, M. De Francesco, A. Cemmi, F. Cardellini, L. Giorgi, Comparison of high surface Pt/C catalysts by cyclic voltammetry, *Journal of Power Sources*, 105 (2002) 13-19.

- [79] J. Amadou, K. Chizari, M. Houllé, I. Janowska, O. Ersen, D. Bégin, C. Pham-Huu, N-doped carbon nanotubes for liquid-phase CC bond hydrogenation, *Catalysis Today*, 138 (2008) 62-68.
- [80] K. Ghosh, M. Kumar, T. Maruyama, Y. Ando, Tailoring the field emission property of nitrogen-doped carbon nanotubes by controlling the graphitic/pyridinic substitution, *Carbon*, 48 (2010) 191-200.
- [81] P.M. Ajayan, Nanotubes from Carbon, *Chemical Reviews*, 99 (1999) 1787-1800.
- [82] P.H. Matter, E. Wang, U.S. Ozkan, Preparation of nanostructured nitrogen-containing carbon catalysts for the oxygen reduction reaction from SiO₂- and MgO-supported metal particles, *Journal of Catalysis*, 243 (2006) 395-403.
- [83] H.A. Gasteiger, S.S. Kocha, B. Sompalli, F.T. Wagner, Activity benchmarks and requirements for Pt, Pt-alloy, and non-Pt oxygen reduction catalysts for PEMFCs, *Applied Catalysis B: Environmental*, 56 (2005) 9-35.
- [84] R. Makharia, S. Kocha, P. Yu, M.A. Sweikart, W. Gu, F. Wagner, H.A. Gasteiger, Durable PEM Fuel Cell Electrode Materials: Requirements and Benchmarking Methodologies, *ECS Transactions*, 1 (2006) 3-18.
- [85] X. Li, H.R. Colón-Mercado, G. Wu, J.-W. Lee, B.N. Popov, Development of Method for Synthesis of Pt – Co Cathode Catalysts for PEM Fuel Cells, *Electrochemical and Solid-State Letters*, 10 (2007) B201-B205.
- [86] J. Wu, X.Z. Yuan, J.J. Martin, H. Wang, J. Zhang, J. Shen, S. Wu, W. Merida, A review of PEM fuel cell durability: Degradation mechanisms and mitigation strategies, *Journal of Power Sources*, 184 (2008) 104-119.
- [87] K. Juodkazis, G. Stalnionis, B. SŠebeka, V. SŠukiené, I. Savickaja, EQCM Study of Rhodium Anodic Dissolution in Sulfuric Acid, *Russian Journal of Electrochemistry*, 38 (2002) 1157-1162.
- [88] S. Mitsushima, S. Kawahara, K.-i. Ota, N. Kamiya, Consumption Rate of Pt under Potential Cycling, *Journal of The Electrochemical Society*, 154 (2007) B153-B158.
- [89] F. Koder, Y. Kuwahara, A. Nakazawa, M. Umeda, Electrochemical corrosion of platinum electrode in concentrated sulfuric acid, *Journal of Power Sources*, 172 (2007) 698-703.
- [90] S. Mitsushima, S. Kawahara, K.-i. Ota, N. Kamiya, Consumption Rate of Pt under Potential Cycling, *Journal of The Electrochemical Society*, 154 (2007) B153-B158.

- [91] R. Borup, J. Davey, F. Garzon, D. Wood, P. Welch, K. More, PEM Fuel Cell Durability With Transportation Transient Operation, *ECS Transactions*, 3 (2006) 879-886.
- [92] V.A. Sethuraman, J.W. Weidner, A.T. Haug, L.V. Protsailo, Durability of Perfluorosulfonic Acid and Hydrocarbon Membranes: Effect of Humidity and Temperature, *Journal of The Electrochemical Society*, 155 (2008) B119-B124.
- [93] M. Crum, W. Liu, Effective Testing Matrix for Studying Membrane Durability in PEM Fuel Cells: Part 2. Mechanical Durability and Combined Mechanical and Chemical Durability, *ECS Transactions*, 3 (2006) 541-550.
- [94] A. Laconti, H. Liu, C. Mittelsteadt, R. McDonald, Polymer Electrolyte Membrane Degradation Mechanisms in Fuel Cells - Findings Over the Past 30 Years and Comparison with Electrolyzers, *ECS Transactions*, 1 (2006) 199-219.
- [95] S.-Y. Huang, P. Ganesan, S. Park, B.N. Popov, Development of a Titanium Dioxide-Supported Platinum Catalyst with Ultrahigh Stability for Polymer Electrolyte Membrane Fuel Cell Applications, *Journal of the American Chemical Society*, 131 (2009) 13898-13899.
- [96] S.D. Knights, K.M. Colbow, J. St-Pierre, D.P. Wilkinson, Aging mechanisms and lifetime of PEFC and DMFC, *Journal of Power Sources*, 127 (2004) 127-134.
- [97] L.M. Roen, C.H. Paik, T.D. Jarvi, Electrocatalytic Corrosion of Carbon Support in PEMFC Cathodes, *Electrochemical and Solid-State Letters*, 7 (2004) A19-A22.
- [98] Y. Shao, G. Yin, J. Zhang, Y. Gao, Comparative investigation of the resistance to electrochemical oxidation of carbon black and carbon nanotubes in aqueous sulfuric acid solution, *Electrochimica Acta*, 51 (2006) 5853-5857.
- [99] B. Avasarala, R. Moore, P. Haldar, Surface oxidation of carbon supports due to potential cycling under PEM fuel cell conditions, *Electrochimica Acta*, 55 (2010) 4765-4771.
- [100] M.-k. Min, J. Cho, K. Cho, H. Kim, Particle size and alloying effects of Pt-based alloy catalysts for fuel cell applications, *Electrochimica Acta*, 45 (2000) 4211-4217.
- [101] U.A. Paulus, A. Wokaun, G.G. Scherer, T.J. Schmidt, V. Stamenkovic, V. Radmilovic, N.M. Markovic, P.N. Ross, Oxygen Reduction on Carbon-Supported Pt-Ni and Pt-Co Alloy Catalysts, *The Journal of Physical Chemistry B*, 106 (2002) 4181-4191.
- [102] V.R. Stamenkovic, B.S. Mun, M. Arenz, K.J.J. Mayrhofer, C.A. Lucas, G. Wang, P.N. Ross, N.M. Markovic, Trends in electrocatalysis on extended and nanoscale Pt-bimetallic alloy surfaces, *Nat Mater*, 6 (2007) 241-247.

- [103] V. Stamenkovic, B.S. Mun, K.J.J. Mayrhofer, P.N. Ross, N.M. Markovic, J. Rossmeisl, J. Greeley, J.K. Nørskov, Changing the Activity of Electrocatalysts for Oxygen Reduction by Tuning the Surface Electronic Structure, *Angewandte Chemie International Edition*, 45 (2006) 2897-2901.
- [104] K. Jayasayee, J.A.R.V. Veen, T.G. Manivasagam, S. Celebi, E.J.M. Hensen, F.A. de Bruijn, Oxygen reduction reaction (ORR) activity and durability of carbon supported PtM (Co, Ni, Cu) alloys: Influence of particle size and non-noble metals, *Applied Catalysis B: Environmental*, 111–112 (2012) 515-526.
- [105] E. Antolini, J.R.C. Salgado, E.R. Gonzalez, The stability of Pt–M (M = first row transition metal) alloy catalysts and its effect on the activity in low temperature fuel cells: A literature review and tests on a Pt–Co catalyst, *Journal of Power Sources*, 160 (2006) 957-968.
- [106] P. Mani, R. Srivastava, P. Strasser, Dealloyed binary PtM₃ (M = Cu, Co, Ni) and ternary PtNi₃M (M = Cu, Co, Fe, Cr) electrocatalysts for the oxygen reduction reaction: Performance in polymer electrolyte membrane fuel cells, *Journal of Power Sources*, 196 (2011) 666-673.
- [107] A.S. Aricò, A.K. Shukla, H. Kim, S. Park, M. Min, V. Antonucci, An XPS study on oxidation states of Pt and its alloys with Co and Cr and its relevance to electroreduction of oxygen, *Applied Surface Science*, 172 (2001) 33-40.
- [108] A.K. Shukla, M. Neergat, P. Bera, V. Jayaram, M.S. Hegde, An XPS study on binary and ternary alloys of transition metals with platinumized carbon and its bearing upon oxygen electroreduction in direct methanol fuel cells, *Journal of Electroanalytical Chemistry*, 504 (2001) 111-119.
- [109] T. Toda, H. Igarashi, H. Uchida, M. Watanabe, Enhancement of the Electroreduction of Oxygen on Pt Alloys with Fe, Ni, and Co, *Journal of The Electrochemical Society*, 146 (1999) 3750-3756.
- [110] T. Toda, H. Igarashi, M. Watanabe, Role of Electronic Property of Pt and Pt Alloys on Electrocatalytic Reduction of Oxygen, *Journal of The Electrochemical Society*, 145 (1998) 4185-4188.
- [111] V. Stamenković, T.J. Schmidt, P.N. Ross, N.M. Marković, Surface Composition Effects in Electrocatalysis: Kinetics of Oxygen Reduction on Well-Defined Pt₃Ni and Pt₃Co Alloy Surfaces, *The Journal of Physical Chemistry B*, 106 (2002) 11970-11979.
- [112] V.R. Stamenkovic, B. Fowler, B.S. Mun, G. Wang, P.N. Ross, C.A. Lucas, N.M. Marković, Improved Oxygen Reduction Activity on Pt₃Ni(111) via Increased Surface Site Availability, *Science*, 315 (2007) 493-497.

- [113] Q. Huang, H. Yang, Y. Tang, T. Lu, D.L. Akins, Carbon-supported Pt–Co alloy nanoparticles for oxygen reduction reaction, *Electrochemistry Communications*, 8 (2006) 1220-1224.
- [114] A. Salvatore Aricò, A. Stassi, I. Gatto, G. Monforte, E. Passalacqua, V. Antonucci, Surface Properties of Pt and PtCo Electrocatalysts and Their Influence on the Performance and Degradation of High-Temperature Polymer Electrolyte Fuel Cells, *The Journal of Physical Chemistry C*, 114 (2010) 15823-15836.
- [115] A. Stassi, I. Gatto, G. Monforte, V. Baglio, E. Passalacqua, V. Antonucci, A.S. Aricò, The effect of thermal treatment on structure and surface composition of PtCo electro-catalysts for application in PEMFCs operating under automotive conditions, *Journal of Power Sources*, 208 (2012) 35-45.
- [116] Z. Yu, J. Zhang, Z. Liu, J.M. Ziegelbauer, H. Xin, I. Dutta, D.A. Muller, F.T. Wagner, Comparison between Dealloyed PtCo₃ and PtCu₃ Cathode Catalysts for Proton Exchange Membrane Fuel Cells, *The Journal of Physical Chemistry C*, 116 (2012) 19877-19885.
- [117] B. Han, C.E. Carlton, A. Kongkanand, R.S. Kukreja, B.R. Theobald, L. Gan, R. O'Malley, P. Strasser, F.T. Wagner, Y. Shao-Horn, Record activity and stability of dealloyed bimetallic catalysts for proton exchange membrane fuel cells, *Energy & Environmental Science*, 8 (2015) 258-266.
- [118] T. Xie, W. Jung, T. Kim, P. Ganesan, B.N. Popov, Development of Highly Active and Durable Hybrid Cathode Catalysts for Polymer Electrolyte Membrane Fuel Cells, *Journal of The Electrochemical Society*, 161 (2014) F1489-F1501.
- [119] B. Arumugam, B.A. Kakade, T. Tamaki, M. Arao, H. Imai, T. Yamaguchi, Enhanced activity and durability for the electroreduction of oxygen at a chemically ordered intermetallic PtFeCo catalyst, *RSC Advances*, 4 (2014) 27510-27517.
- [120] S. Du, Y. Lu, S.K. Malladi, Q. Xu, R. Steinberger-Wilckens, A simple approach for PtNi-MWCNT hybrid nanostructures as high performance electrocatalysts for the oxygen reduction reaction, *Journal of Materials Chemistry A*, 2 (2014) 692-698.
- [121] X. An, T. Simmons, R. Shah, C. Wolfe, K.M. Lewis, M. Washington, S.K. Nayak, S. Talapatra, S. Kar, Stable Aqueous Dispersions of Noncovalently Functionalized Graphene from Graphite and their Multifunctional High-Performance Applications, *Nano Letters*, 10 (2010) 4295-4301.
- [122] H.-S. Oh, H. Kim, Efficient Synthesis of Pt Nanoparticles Supported on Hydrophobic Graphitized Carbon Nanofibers for Electrocatalysts Using Noncovalent Functionalization, *Advanced Functional Materials*, 21 (2011) 3954-3960.

- [123] S. Ghatak, G. Chakraborty, A.K. Meikap, T. Woods, R. Babu, W.J. Blau, Synthesis and characterization of polyaniline/carbon nanotube composites, *Journal of Applied Polymer Science*, 119 (2011) 1016-1025.
- [124] J. Stejskal, R.G. Gilbert, Preparation of a conducting polymer, *Pure and Appl.Chem.*, 74 (2002) 857-867.
- [125] U.S. DRIVE Fuel Cell Tech Team (January 14 2014)
<http://www.uscar.org/guest/teams/17/Fuel-Cell-Tech-Team>.
- [126] C. Kim, S.-H. Park, J.-I. Cho, D.-Y. Lee, T.-J. Park, W.-J. Lee, K.-S. Yang, Raman spectroscopic evaluation of polyacrylonitrile-based carbon nanofibers prepared by electrospinning, *Journal of Raman Spectroscopy*, 35 (2004) 928-933.
- [127] S. Koh, J. Leisch, M.F. Toney, P. Strasser, Structure-Activity-Stability Relationships of Pt-Co Alloy Electrocatalysts in Gas-Diffusion Electrode Layers, *The Journal of Physical Chemistry C*, 111 (2007) 3744-3752.
- [128] S. Zhang, X. Zhang, G. Jiang, H. Zhu, S. Guo, D. Su, G. Lu, S. Sun, Tuning Nanoparticle Structure and Surface Strain for Catalysis Optimization, *Journal of the American Chemical Society*, 136 (2014) 7734-7739.
- [129] W. Trongchuanvij, K. Pruksathorn, M. Hunsom, Preparation of a high performance Pt-Co/C electrocatalyst for oxygen reduction in PEM fuel cell via a combined process of impregnation and seeding, *Applied Energy*, 88 (2011) 974-980.
- [130] Y.-w. Ma, Z.-r. Liu, B.-l. Wang, L. Zhu, J.-p. Yang, X.-a. Li, Preparation of graphene-supported Pt-Co nanoparticles and their use in oxygen reduction reactions, *New Carbon Materials*, 27 (2012) 250-257.
- [131] Y. Sugawara, A.P. Yadav, A. Nishikata, T. Tsuru, EQCM Study on Anodic Dissolution of Platinum in Acid Solutions, *Electrochemistry*, 75 (2007) 359
- [132] E. Antolini, J.R.C. Salgado, M.J. Giz, E.R. Gonzalez, Effects of geometric and electronic factors on ORR activity of carbon supported Pt-Co electrocatalysts in PEM fuel cells, *International Journal of Hydrogen Energy*, 30 (2005) 1213-1220.
- [133] V.R. Stamenkovic, B.S. Mun, K.J.J. Mayrhofer, P.N. Ross, N.M. Markovic, Effect of Surface Composition on Electronic Structure, Stability, and Electrocatalytic Properties of Pt-Transition Metal Alloys: Pt-Skin versus Pt-Skeleton Surfaces, *Journal of the American Chemical Society*, 128 (2006) 8813-8819.
- [134] A. Groß, Reactivity of Bimetallic Systems Studied from First Principles, *Top Catal*, 37 (2006) 29-39.

- [135] J.R. Kitchin, J.K. Nørskov, M.A. Barteau, J.G. Chen, Role of Strain and Ligand Effects in the Modification of the Electronic and Chemical Properties of Bimetallic Surfaces, *Physical Review Letters*, 93 (2004) 156801.
- [136] A. Schlapka, M. Lischka, A. Groß, U. Käsberger, P. Jakob, Surface Strain versus Substrate Interaction in Heteroepitaxial Metal Layers: Pt on Ru(0001), *Physical Review Letters*, 91 (2003) 016101.
- [137] Y. Gauthier, M. Schmid, S. Padovani, E. Lundgren, V. Buš, G. Kresse, J. Redinger, P. Varga, Adsorption Sites and Ligand Effect for CO on an Alloy Surface: A Direct View, *Physical Review Letters*, 87 (2001) 036103.
- [138] R. Burch, Importance of electronic ligand effects in metal alloy catalysts, *Accounts of Chemical Research*, 15 (1982) 24-31.
- [139] C. Wang, M. Chi, D. Li, D. Strmcnik, D. van der Vliet, G. Wang, V. Komanicky, K.-C. Chang, A.P. Paulikas, D. Tripkovic, J. Pearson, K.L. More, N.M. Markovic, V.R. Stamenkovic, Design and Synthesis of Bimetallic Electrocatalyst with Multilayered Pt-Skin Surfaces, *Journal of the American Chemical Society*, 133 (2011) 14396-14403.
- [140] Y. Shao, G. Yin, Y. Gao, Understanding and approaches for the durability issues of Pt-based catalysts for PEM fuel cell, *Journal of Power Sources*, 171 (2007) 558-566.
- [141] Z. Chen, M. Waje, W. Li, Y. Yan, Supportless Pt and PtPd Nanotubes as Electrocatalysts for Oxygen-Reduction Reactions, *Angewandte Chemie International Edition*, 46 (2007) 4060-4063.
- [142] H.R. Colón-Mercado, B.N. Popov, Stability of platinum based alloy cathode catalysts in PEM fuel cells, *Journal of Power Sources*, 155 (2006) 253-263.
- [143] J. Speder, A. Zana, I. Spanos, J.J.K. Kirkensgaard, K. Mortensen, M. Hanzlik, M. Arenz, Comparative degradation study of carbon supported proton exchange membrane fuel cell electrocatalysts – The influence of the platinum to carbon ratio on the degradation rate, *Journal of Power Sources*, 261 (2014) 14-22.
- [144] H. Zhang, H. Haas, J. Hu, S. Kundu, M. Davis, C. Chuy, The Impact of Potential Cycling on PEMFC Durability, *Journal of The Electrochemical Society*, 160 (2013) F840-F847.
- [145] L. Dubau, J. Durst, F. Maillard, L. Guétaz, M. Chatenet, J. André, E. Rossinot, Further insights into the durability of Pt₃Co/C electrocatalysts: Formation of “hollow” Pt nanoparticles induced by the Kirkendall effect, *Electrochimica Acta*, 56 (2011) 10658-10667.

- [146] L. Dubau, F. Maillard, M. Chatenet, L. Guetaz, J. André, E. Rossinot, Durability of Pt₃Co / C Cathodes in a 16 Cell PEMFC Stack: Macro/Microstructural Changes and Degradation Mechanisms, *Journal of The Electrochemical Society*, 157 (2010) B1887-B1895.
- [147] Y. Yu, H.L. Xin, R. Hovden, D. Wang, E.D. Rus, J.A. Mundy, D.A. Muller, H.D. Abruña, Three-Dimensional Tracking and Visualization of Hundreds of Pt–Co Fuel Cell Nanocatalysts During Electrochemical Aging, *Nano Letters*, 12 (2012) 4417-4423.
- [148] H.L. Xin, J.A. Mundy, Z. Liu, R. Cabezas, R. Hovden, L.F. Kourkoutis, J. Zhang, N.P. Subramanian, R. Makharia, F.T. Wagner, D.A. Muller, Atomic-Resolution Spectroscopic Imaging of Ensembles of Nanocatalyst Particles Across the Life of a Fuel Cell, *Nano Letters*, 12 (2012) 490-497.
- [149] S. Hidai, M. Kobayashi, H. Niwa, Y. Harada, M. Oshima, Y. Nakamori, T. Aoki, Changes in electronic states of platinum–cobalt alloy catalyst for polymer electrolyte fuel cells by potential cycling, *Journal of Power Sources*, 196 (2011) 8340-8345.
- [150] L. Dubau, M. Lopez-Haro, L. Castanheira, J. Durst, M. Chatenet, P. Bayle-Guillemaud, L. Guétaz, N. Caqué, E. Rossinot, F. Maillard, Probing the structure, the composition and the ORR activity of Pt₃Co/C nanocrystallites during a 3422 h PEMFC ageing test, *Applied Catalysis B: Environmental*, 142–143 (2013) 801-808.
- [151] S. Ohyagi, T. Sasaki, Durability of a PEMFC Pt–Co cathode catalyst layer during voltage cycling tests under supersaturated humidity conditions, *Electrochimica Acta*, 102 (2013) 336-341.
- [152] S. Koh, M.F. Toney, P. Strasser, Activity–stability relationships of ordered and disordered alloy phases of Pt₃Co electrocatalysts for the oxygen reduction reaction (ORR), *Electrochimica Acta*, 52 (2007) 2765-2774.
- [153] M. Teliska, V.S. Murthi, S. Mukerjee, D.E. Ramaker, Correlation of Water Activation, Surface Properties, and Oxygen Reduction Reactivity of Supported Pt–M/C Bimetallic Electrocatalysts Using XAS, *Journal of The Electrochemical Society*, 152 (2005) A2159-A2169.
- [154] A. Parthasarathy, S. Srinivasan, A.J. Appleby, C.R. Martin, Temperature Dependence of the Electrode Kinetics of Oxygen Reduction at the Platinum/Nafion® Interface—A Microelectrode Investigation, *Journal of The Electrochemical Society*, 139 (1992) 2530-2537.
- [155] F. Ettingshausen, J. Kleemann, A. Marcu, G. Toth, H. Fuess, C. Roth, Dissolution and Migration of Platinum in PEMFCs Investigated for Start/Stop Cycling and High Potential Degradation, *Fuel Cells*, 11 (2011) 238-245.

- [156] L. Kim, C.G. Chung, Y.W. Sung, J.S. Chung, Investigation of Migrated Platinum Distributions in PEMFC Under Excess H₂/O₂, ECS Transactions, 16 (2008) 945-953.
- [157] S. Vinod Selvaganesh, G. Selvarani, P. Sridhar, S. Pitchumani, A.K. Shukla, Graphitic Carbon as Durable Cathode-Catalyst Support for PEFCs, Fuel Cells, 11 (2011) 372-384.
- [158] Z.Y. Liu, B.K. Brady, R.N. Carter, B. Litteer, M. Budinski, J.K. Hyun, D.A. Muller, Characterization of Carbon Corrosion-Induced Structural Damage of PEM Fuel Cell Cathode Electrodes Caused by Local Fuel Starvation, Journal of The Electrochemical Society, 155 (2008) B979-B984.
- [159] M. Hara, M. Lee, C.-H. Liu, B.-H. Chen, Y. Yamashita, M. Uchida, H. Uchida, M. Watanabe, Electrochemical and Raman spectroscopic evaluation of Pt/graphitized carbon black catalyst durability for the start/stop operating condition of polymer electrolyte fuel cells, Electrochimica Acta, 70 (2012) 171-181.
- [160] F. Tuinstra, J.L. Koenig, Raman Spectrum of Graphite, The Journal of Chemical Physics, 53 (1970) 1126-1130.
- [161] I. Herrmann, U.I. Kramm, J. Radnik, S. Fiechter, P. Bogdanoff, Influence of Sulfur on the Pyrolysis of CoTMPP as Electrocatalyst for the Oxygen Reduction Reaction, Journal of The Electrochemical Society, 156 (2009) B1283-B1292.
- [162] G. Wu, C.M. Johnston, N.H. Mack, K. Artyushkova, M. Ferrandon, M. Nelson, J.S. Lezama-Pacheco, S.D. Conradson, K.L. More, D.J. Myers, P. Zelenay, Synthesis-structure-performance correlation for polyaniline-Me-C non-precious metal cathode catalysts for oxygen reduction in fuel cells, Journal of Materials Chemistry, 21 (2011) 11392-11405.
- [163] H. Liu, J. Li, X. Xu, F. Wang, J. Liu, Z. Li, J. Ji, Highly graphitic carbon black-supported platinum nanoparticle catalyst and its enhanced electrocatalytic activity for the oxygen reduction reaction in acidic medium, Electrochimica Acta, 93 (2013) 25-31.
- [164] X. Pan, Y.-J. Xu, Defect-Mediated Growth of Noble-Metal (Ag, Pt, and Pd) Nanoparticles on TiO₂ with Oxygen Vacancies for Photocatalytic Redox Reactions under Visible Light, The Journal of Physical Chemistry C, 117 (2013) 17996-18005.
- [165] S.-Y. Huang, P. Ganesan, B.N. Popov, Titania supported platinum catalyst with high electrocatalytic activity and stability for polymer electrolyte membrane fuel cell, Applied Catalysis B: Environmental, 102 (2011) 71-77.

- [166] J. Wang, G. Yin, Y. Shao, S. Zhang, Z. Wang, Y. Gao, Effect of carbon black support corrosion on the durability of Pt/C catalyst, *Journal of Power Sources*, 171 (2007) 331-339.
- [167] A.A. Franco, *Polymer Electrolyte Fuel Cells: Science, Applications, and Challenges*, Pan Stanford Publishing, Singapore, 2013
- [168] F. Coloma, A. Sepulvedaescribano, F. Rodriguezreinoso, Heat-Treated Carbon-Blacks as Supports for Platinum Catalysts, *Journal of Catalysis*, 154 (1995) 299-305.
- [169] Y. Shao, G. Yin, Y. Gao, P. Shi, Durability Study of Pt/C and Pt/CNTs Catalysts under Simulated PEM Fuel Cell Conditions, *Journal of The Electrochemical Society*, 153 (2006) A1093-A1097.
- [170] J.C. Meier, C. Galeano, I. Katsounaros, A.A. Topalov, A. Kostka, F. Schüth, K.J.J. Mayrhofer, Degradation Mechanisms of Pt/C Fuel Cell Catalysts under Simulated Start–Stop Conditions, *ACS Catalysis*, 2 (2012) 832-843.
- [171] L. Castanheira, L. Dubau, M. Mermoux, G. Berthomé, N. Caqué, E. Rossinot, M. Chatenet, F. Maillard, Carbon Corrosion in Proton-Exchange Membrane Fuel Cells: From Model Experiments to Real-Life Operation in Membrane Electrode Assemblies, *ACS Catalysis*, 4 (2014) 2258-2267.
- [172] K.H. Lim, H.-S. Oh, H. Kim, Use of a carbon nanocage as a catalyst support in polymer electrolyte membrane fuel cells, *Electrochemistry Communications*, 11 (2009) 1131-1134.
- [173] X.X. Wang, Z.H. Tan, M. Zeng, J.N. Wang, Carbon nanocages: A new support material for Pt catalyst with remarkably high durability, *Scientific Reports*, 4 (2014) 4437.
- [174] S. Zhang, Y. Shao, G. Yin, Y. Lin, Self-assembly of Pt nanoparticles on highly graphitized carbon nanotubes as an excellent oxygen-reduction catalyst, *Applied Catalysis B: Environmental*, 102 (2011) 372-377.
- [175] L. Li, Y. Xing, Electrochemical durability of carbon nanotubes at 80 °C, *Journal of Power Sources*, 178 (2008) 75-79.
- [176] J.H. Jung, H.J. Park, J. Kim, S.H. Hur, Highly durable Pt/graphene oxide and Pt/C hybrid catalyst for polymer electrolyte membrane fuel cell, *Journal of Power Sources*, 248 (2014) 1156-1162.
- [177] E. Antolini, Graphene as a new carbon support for low-temperature fuel cell catalysts, *Applied Catalysis B: Environmental*, 123–124 (2012) 52-68.

- [178] Y. Li, Y. Li, E. Zhu, T. McLouth, C.-Y. Chiu, X. Huang, Y. Huang, Stabilization of High-Performance Oxygen Reduction Reaction Pt Electrocatalyst Supported on Reduced Graphene Oxide/Carbon Black Composite, *Journal of the American Chemical Society*, 134 (2012) 12326-12329.
- [179] H. Lv, N. Cheng, S. Mu, M. Pan, Heat-treated multi-walled carbon nanotubes as durable supports for PEM fuel cell catalysts, *Electrochimica Acta*, 58 (2011) 736-742.
- [180] J.N. Tiwari, K. Nath, S. Kumar, R.N. Tiwari, K.C. Kemp, N.H. Le, D.H. Youn, J.S. Lee, K.S. Kim, Stable platinum nanoclusters on genomic DNA–graphene oxide with a high oxygen reduction reaction activity, *Nat Commun*, 4 (2013).
- [181] V.I. Birss, M. Chang, J. Segal, Platinum oxide film formation—reduction: an in-situ mass measurement study, *Journal of Electroanalytical Chemistry*, 355 (1993) 181-191.
- [182] Y. Furuya, T. Mashio, A. Ohma, N. Dale, K. Oshihara, G. Jerkiewicz, Surface oxide growth on platinum electrode in aqueous trifluoromethanesulfonic acid, *The Journal of Chemical Physics*, 141 (2014) 164705.
- [183] X. Yu, S. Ye, Recent advances in activity and durability enhancement of Pt/C catalytic cathode in PEMFC: Part II: Degradation mechanism and durability enhancement of carbon supported platinum catalyst, *Journal of Power Sources*, 172 (2007) 145-154.
- [184] E. Antolini, Formation, microstructural characteristics and stability of carbon supported platinum catalysts for low temperature fuel cells, *Journal of Materials Science*, 38 (2003) 2995-3005.
- [185] N.T. Cuong, D.H. Chi, Y.-T. Kim, T. Mitani, Structural and electronic properties of Pt_n (n = 3, 7, 13) clusters on metallic single wall carbon nanotube, *physica status solidi (b)*, 243 (2006) 3472-3475.
- [186] G. Gupta, D.A. Slanac, P. Kumar, J.D. Wiggins-Camacho, J. Kim, R. Ryoo, K.J. Stevenson, K.P. Johnston, Highly Stable Pt/Ordered Graphitic Mesoporous Carbon Electrocatalysts for Oxygen Reduction, *The Journal of Physical Chemistry C*, 114 (2010) 10796-10805.
- [187] R. Böttcher, C. Klimm, H.C. Semmelhack, G. Völkel, H.J. Gläsel, E. Hartmann, Size Effect in Mn²⁺ Doped Barium Titanate Nanopowders Observed by Means of Electron Paramagnetic Resonance (EPR), *physica status solidi (b)*, 215 (1999) R3-R4.
- [188] E. Emre, S. Hans-Christoph, B. Rolf, R. Holger, B. Juras, M. Anke, G. Hans-Jürgen, H. Dietmar, H. Eberhard, Study of the tetragonal-to-cubic phase transition in PbTiO₃ nanopowders, *Journal of Physics: Condensed Matter*, 18 (2006) 3861.

[189] M. Tanaka, Y. Makino, Finite size effects in submicron barium titanate particles, *Ferroelectrics Letters Section*, 24 (1998) 13-23.

[190] M. Lopez-Haro, L. Dubau, L. Guétaz, P. Bayle-Guillemaud, M. Chatenet, J. André, N. Caqué, E. Rossinot, F. Maillard, Atomic-scale structure and composition of Pt₃Co/C nanocrystallites during real PEMFC operation: A STEM–EELS study, *Applied Catalysis B: Environmental*, 152–153 (2014) 300-308.